Summer 2020

Neutrino Induced Coherent-Pion: Precision Measurement in NOMAD and Uses in Oscillation Experiments

Bing Guo

Neutrino induced Coherent-Pion: Precision Measurement in NOMAD and Uses in Oscillation Experiments

by

Bing Guo

Bachelor of Science
East China Normal University 2012

Submitted in Partial Fulfillment of the Requirements

for the Degree of Doctor of Philosophy in

Physics

College of Arts and Sciences

University of South Carolina

2020

Accepted by:

Sanjib R. Mishra, Major Professor

Roberto Petti, Committee Member

Pawel O. Mazur, Committee Member

Jianming Bian, Committee Member

Cheryl Addy, Vice Provost and Dean of the Graduate School

Dedication

This dissertation is dedicated to my family for their unyielding love and support, and to my advisor Sanjib Mishra for his meticulous guidance in the ocean of physics.

Acknowledgments

I would like to express my heartiest gratitude and sincere thanks to my advisor Sanjib Mishra, he brought me into neutrino physics area six years ago, consistently gave me valuable guidance and suggestions throughout my Ph.D research. I also want to thank Professor Roberto Petti for providing precious ideas and assistance in my research.

I am also thankful to my committee members, Professor Pawel Mazur and professor Jianming Bian, for their valuble guidance in my physics classes and my neutrino research.

My thanks also go to my collegues at University of South Carolina: Hongyue Duyang, Xinchun Tian, Libo Jiang, Chris Kullenberg, Kevin Wilson. They gave me so much help in past six years and I enjoyed the time working with them.

I also want to thank all the people from NOvA collaboration for their zealous help for last a few years.

Abstract

In the era of high precision oscillation measurements, lead by DUNE and Hyper-K, the Near Detector (ND) faces unprecedented challenges and opportunities. Among the various neutrino events in ND, Coherent meson production plays a special role. It is a non-negligible background to the oscillation signal. However the cross-section models for neutrino induced Coherent meson currently being used are old and imprecise. On the other hand, Coherent meson has a simple experimental signature with minimal nuclear effect making it unique among neutrino-nucleon interactions. Furthermore, the cross section for Coherent meson is the same in neutrino and antineutrino modes. It, thus, potentially could offer the most precise constraints on NuMuBar/NuMu flux ratio. Coherent pion production has been studied in NOMAD experiment, It has resulted in the most precise determination of the process to date. Two different model has been used and compared with an attempt to test PCAC hypothesis. Inspired by NOMAD detector, a straw tube technology based tracking device is proposed for the Near Detector complex of DUNE, it's performance and advantages are shown, Coherent meson production is also developed in it with validation of it's application to flux ratio determination.

Table of Contents

List of Tables

List of Figures

Chapter 1

Introduction

1.1 The Discovery of Neutrino

The idea of neutrino is introduced in 1930s to solve the problem found in nuclear beta decay.[38] At that time, what people noticed is some radioactive nucleus transformed to a lighter nucleus with emission of a electron, some examples are potassium goes to calcium, tritium goes to helium. But the common sense of two-body decay that the outgoing particles' energies are fixed is not supported by electron's large energy variation showed in experiments. Niels Bohr tried to explain it by giving up the law of conservation of energy, when Pauli proposed another neutral, light and undiscovered particle exists to share the missing energy. Later on Fermi coined the name "neutrino" and it becomes what has been used till today.

The direct experimental confirmation of the existence of neutrino didn't come until mid-1950s at Savannah River nuclear reactor in South Carolina, where Cowan and Reines used a large tank of water to capture anti-neutrino by "inverse" beta decay reaction:

$$\bar{\nu} + p^{+} - > n + e^{+} \tag{1.1}$$

The reactor had a anti-neutrino flux of 5×10^{13} neutrinos per second per square centimeter, which gave them two to three events per hour. In the end, they measured the cross-section to be $6.3 \times 10^{-44} cm^2$.

1.2 Neutrino oscillation model: PMNS matrix

Before we dive into the history how neutrino oscillation are discovered, and how each parameter are measured and constrained by different generations of neutrino detectors, let's get familiar with the theoretical model first.

In Standard model, there are three known flavors of neutrinos, electron neutrino (ν_e), muon neutrino (ν_μ) and tau neutrino(ν_τ), corresponding to their charged counterparts: electron, muon and tau. All three types of neutrinos can only be generated by weak interaction and only interact through weak channel, which make them three weak eigenstates or flavor eigenstates. It had been a long while that physicists believe neutrinos are massless. But from a few decades ago, this last brick of standard model grand building get broken.

Contrary to standard model, neutrinos actually possess mass. There are three mass eigenstates of neutrinos, ν_1, ν_2 and ν_3, and they are different from the three flavor eigenstates. Their relationship can be expressed by PMNS matrix:

$$\begin{pmatrix} \nu_e \\ \nu_\mu \\ \nu_\tau \end{pmatrix} = \begin{pmatrix} U_{e1} & U_{e2} & U_{e3} \\ U_{\mu 1} & U_{\mu 2} & U_{\mu 3} \\ U_{\tau 1} & U_{\tau 2} & U_{\tau 3} \end{pmatrix} \begin{pmatrix} \nu_1 \\ \nu_2 \\ \nu_3 \end{pmatrix} \tag{1.2}$$

The matrix is unitary, and it follows:

$$\begin{pmatrix} \nu_1 \\ \nu_2 \\ \nu_3 \end{pmatrix} = \begin{pmatrix} U^*_{e1} & U^*_{\mu 1} & U^*_{\tau 1} \\ U^*_{e2} & U^*_{\mu 2} & U^*_{\tau 2} \\ U^*_{e3} & U^*_{\mu 3} & U^*_{\tau 3} \end{pmatrix} \begin{pmatrix} \nu_e \\ \nu_\mu \\ \nu_\tau \end{pmatrix} \tag{1.3}$$

The unitarity give a few useful relations:

$$\begin{aligned}
U_{e1}U_{e1}^* + U_{\mu 1}U_{\mu 1}^* + U_{\tau 1}U_{\tau 1}^* &= 1 \\
U_{e2}U_{e2}^* + U_{\mu 2}U_{\mu 2}^* + U_{\tau 2}U_{\tau 2}^* &= 1 \\
U_{e3}U_{e3}^* + U_{\mu 3}U_{\mu 3}^* + U_{\tau 3}U_{\tau 3}^* &= 1 \\
U_{e1}U_{\mu 1}^* + U_{e2}U_{\mu 2}^* + U_{e3}U_{\mu 3}^* &= 1 \\
U_{e1}U_{\tau 1}^* + U_{e2}U_{\tau 2}^* + U_{e3}U_{\tau 3}^* &= 1 \\
U_{\mu 1}U_{\tau 1}^* + U_{\mu 2}U_{\tau 2}^* + U_{\mu 3}U_{\tau 3}^* &= 1
\end{aligned} \tag{1.4}$$

Assume at time 0, the neutrino is in it's flavor eigenstate $|\nu_\alpha\rangle$

$$|\phi(t=0)\rangle = U_{\alpha 1}|\nu_1\rangle + U_{\alpha 2}|\nu_2\rangle + U_{\alpha 3}|\nu_3\rangle \tag{1.5}$$

so the wavefunction at x(t) will be:

$$|\phi(t)\rangle = U_{\alpha 1}|\nu_1\rangle e^{-ip_1 x} + U_{\alpha 2}|\nu_2\rangle e^{-ip_2 x} + U_{\alpha 3}|\nu_3\rangle e^{-ip_3 x} \tag{1.6}$$

where $p_i x = E_i t - \mathbf{p_i x}$. After distance L, the wavefunction becomes

$$|\phi(t)\rangle = U_{\alpha 1}|\nu_1\rangle e^{-i\phi_1} + U_{\alpha 2}|\nu_2\rangle e^{-i\phi_2} + U_{\alpha 3}|\nu_3\rangle e^{-i\phi_3} \tag{1.7}$$

where $\phi_i = p_i x = E_i t - |p_i|L \approx (E_i - |p_i|)L$. Since $E_i \approx p_i + \dfrac{m_i^2}{2E_i}$, so

$$\phi_i = (E_i - |p_i|)L \approx \frac{m_i^2 L}{2E_i} \tag{1.8}$$

Expressing each mass eigenstate with flavor eigenstates in (1.8) and after rearrangement gives:

$$\begin{aligned}
|\phi(t)\rangle =& (U_{\alpha 1}U_{e1}^* e^{-i\phi_1} + U_{\alpha 2}U_{e2}^* e^{-i\phi_2} + U_{\alpha 3}U_{e3}^* e^{-i\phi_3})|\nu_e\rangle \\
&+ (U_{\alpha 1}U_{\mu 1}^* e^{-i\phi_1} + U_{\alpha 2}U_{\mu 2}^* e^{-i\phi_2} + U_{\alpha 3}U_{\mu 3}^* e^{-i\phi_3})|\nu_\mu\rangle \\
&+ (U_{\alpha 1}U_{\tau 1}^* e^{-i\phi_1} + U_{\alpha 2}U_{\tau 2}^* e^{-i\phi_2} + U_{\alpha 3}U_{\tau 3}^* e^{-i\phi_3})|\nu_\tau\rangle
\end{aligned} \tag{1.9}$$

The oscillation probability P($\nu_\alpha \to \nu_\beta$ can be obtained :

$$\begin{aligned}
&P(\nu_\alpha \to \nu_\beta) = |\langle \nu_\beta | \nu_\alpha \rangle|^2 \\
&= (U_{\alpha 1} U^*_{\beta 1} e^{-i\phi_1} + U_{\alpha 2} U^*_{\beta 2} e^{-i\phi_2} + U_{\alpha 3} U^*_{\beta 3} e^{-i\phi_3})^2 \\
&= |U_{\alpha 1} U^*_{\beta 1}|^2 + |U_{\alpha 2} U^*_{\beta 2}|^2 + |U_{\alpha 3} U^*_{\beta 3}|^2 + 2R(U_{\alpha 1} U^*_{\beta 1} U^*_{\alpha 2} U_{\beta 2} e^{-i(\phi_1 - \phi_2)} \\
&\quad + U_{\alpha 1} U^*_{\beta 1} U^*_{\alpha 3} U_{\beta 3} e^{-i(\phi_1 - \phi_3)} + U_{\alpha 2} U^*_{\beta 2} U^*_{\alpha 3} U_{\beta 3} e^{-i(\phi_2 - \phi_3)}) \\
&= (U_{\alpha 1} U^*_{\beta 1} + U_{\alpha 2} U^*_{\beta 2} + U_{\alpha 3} U^*_{\beta 3})^2 + 2R[U_{\alpha 1} U^*_{\beta 1} U^*_{\alpha 2} U_{\beta 2} (e^{-i(\phi_1 - \phi_2)} - 1)] \\
&+ 2R[U_{\alpha 1} U^*_{\beta 1} U^*_{\alpha 3} U_{\beta 3} (e^{-i(\phi_1 - \phi_3)} - 1)] + 2R[U_{\alpha 2} U^*_{\beta 2} U^*_{\alpha 3} U_{\beta 3} (e^{-i(\phi_2 - \phi_3)} - 1)]
\end{aligned} \tag{1.10}$$

since:

$$\begin{aligned}
e^{-i(\phi_1 - \phi_2)} - 1 =& e^{-i\frac{L}{2E}(m_1^2 - m_2^2)} - 1 \\
=& (\cos\left(\frac{\Delta m^2_{12} L}{2E}\right) - 1) + i \sin\left(\frac{\Delta m^2_{12} L}{2E}\right) \\
=& -2\sin^2(\frac{\Delta m^2_{12} L}{4E}) + i \sin\left(\frac{\Delta m^2_{12} L}{2E}\right)
\end{aligned} \tag{1.11}$$

where $\Delta m^2_{ij} \equiv m^2_i - m^2_j$ with $i, j = 1, 2, 3$ we have:

$$\begin{aligned}
P(\nu_\alpha \to \nu_\beta) =& \delta_{\alpha\beta} - 4 \sum_{i<j} Re(U_{\alpha i} U^*_{\beta i} U_{\alpha j} U^*_{\beta j}) sin^2(\frac{\Delta m^2_{ij} L}{4E}) \\
&+ 2 \sum_{i<j} Im(U_{\alpha i} U^*_{\beta i} U_{\alpha j} U^*_{\beta j}) sin^2(\frac{\Delta m^2_{ij} L}{2E})
\end{aligned} \tag{1.12}$$

if the CP-violation angle δ_{cp} is zero, then the imaginary term vanishes and we are left with:

$$P(\nu_\alpha \to \nu_\beta) = \delta_{\alpha\beta} - 4 \sum_{i<j} Re(U_{\alpha i} U^*_{\beta i} U_{\alpha j} U^*_{\beta j}) sin^2(\frac{\Delta m^2_{ij} L}{4E}) \tag{1.13}$$

and if we use km as the unit of L, GeV as the unit of E, then:

$$\frac{\Delta m^2_{ij} L}{4E} = 1.27 \Delta m^2_{ij}[\mathrm{eV}^2] \ \frac{L[\mathrm{Km}]}{E[\mathrm{GeV}]} \tag{1.14}$$

The PMNS matrix can be expressed by three rotation matrices and three complex phases:

$$U = \begin{pmatrix} 1 & 0 & 0 \\ 0 & \cos\theta_{23} & \sin\theta_{23} \\ 0 & -\sin\theta_{23} & \cos\theta_{23} \end{pmatrix} \begin{pmatrix} \cos\theta_{13} & 0 & \sin\theta_{13}e^{-i\delta_{cp}} \\ 0 & 1 & 0 \\ -\sin\theta_{13}e^{-i\delta_{cp}} & 0 & \cos\theta_{13} \end{pmatrix} \times \begin{pmatrix} \cos\theta_{12} & \sin\theta_{12} & 0 \\ -\sin\theta_{12} & \cos\theta_{12} & 0 \\ 0 & 0 & 1 \end{pmatrix} \begin{pmatrix} 1 & 0 & 0 \\ 0 & e^{i\alpha_2/2} & 0 \\ 0 & 0 & e^{i\alpha_3/2} \end{pmatrix} \tag{1.15}$$

The phase factors α_2 and α_3 are non-zero only if neutrinos are Majorana particles, and do not enter into oscillation phenomena regardless. The phase factor δ is no-zero only if neutrino oscillation violates the CP symmetry. If experiment shows this 3×3 matrix to be not unitary, a sterile neutrino or some other new physics is required.

Now Let's assume neutrinos are neither Majorana particles nor sterile, the last matrix becomes identity matrix, put all matrices together, we have:

$$U = \begin{pmatrix} c_{12}c_{13} & s_{12}c_{13} & s_{13}e^{-i\delta} \\ -s_{12}c_{23} - c_{12}s_{23}s_{13}e^{i\delta} & c_{12}c_{23} - s_{12}s_{23}s_{13}e^{i\delta} & s_{23}c_{13} \\ s_{12}s_{23} - c_{12}c_{23}s_{13}e^{i\delta} & -c_{12}s_{23} - s_{12}c_{23}s_{13}e^{i\delta} & c_{23}c_{13} \end{pmatrix} \tag{1.16}$$

In order to have oscillation, the probability has to be non-zero, it requires three neutrino mass eigenstates have different masses and the angles are not zero. So when neutrino oscillations are being/already confirmed, we are left with a bunch of parameters to measure: three angles($\theta_{12}, \theta_{13}, \theta_{23}$), and two mass differences (Δm^2_{12} and Δm^2_{23}, this will be discussed later) and 1 phase angle (δ_{CP}). Unluckily there's no single experiment so far can be sensitive to all of them, and it already took a couple of generations and types of neutrino detectors to measure and constrain them.

In order to be sensitive to the oscillation parameters, the term in $sin()$ can not be too small or too large which means we have to set up experiment to make $E/L \cong \Delta m^2_{ij}$. If $E/L \gg \Delta m^2_{ij}$ the neutrino doesn't travel long enough to oscillate to another flavor because $\sin^2 x_{ij} \ll 1$. For $E/L \ll \Delta m^2_{ij}$, the oscillating phase goes

Table 1.1: Characteristic values of L and E for various neutrino sources and experiments.[10]

Experiment	**L** [m]	**E** [MeV]
Solar	10^{10}	1
Atmospheric	$10^4 - 10^7$	$10^2 - 10^5$
Reactor	$10^2 - 10^5$	1
Accelerator	10^2	$10^3 - 10^4$
Long Baseline Accelerator	$10^5 - 10^6$	$10^3 - 10^4$

through many cycles before detection and, since in general neutrino beams are neither monochromatic nor from a point source, the phase is averaged to $< sin^2\theta_{ij} >= 1/2$ and it becomes insensitive too.

1.3 THE DISCOVERY OF NEUTRINO OSCILLATION AND EARLY NEUTRINO OSCILLATION EXPERIMENTS

1.3.1 THE SOLAR NEUTRINO PROBLEM

The Standard Solar Model predicts that most of the flux comes from the pp neutrinos with energies below 0.4 MeV. Only the Gallium experiments are sensitive to this component. The Chlorine experiments can just observe part of the $7Be$ line, and can see the other components. The big water experiments (Super-Kamiokande, SNO) can only view the 8B neutrinos as they have too high a threshold to see below about 5 MeV.

Homestake

Ray Davis' Homestake experiment [33] was the first neutrino experiment designed to look for solar neutrinos. It was built in the period 1965 to 1967 to measure the solar neutrinos above 0.814 MeV. It was in Homestake mine, 4850 feet underground, to shield from cosmic rays, with a100,000-gallon tank full of perchloroethylene, or dry cleaning fluid. A radiochemical technique is used, based on the inverse beta reaction:

$$\nu_e + {}^{37}\mathrm{Cl} \rightarrow {}^{37}\mathrm{Ar} + e^- \tag{1.17}$$

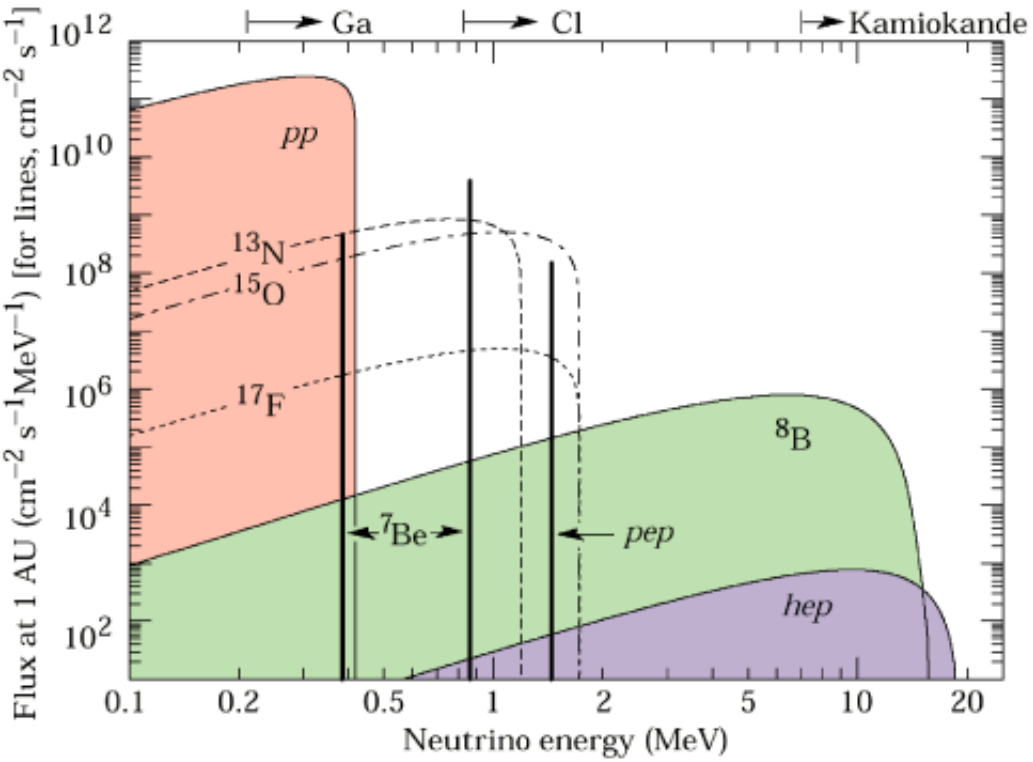

Figure 1.1: The Standard Solar Model's prediction of neutrino flux. Threshold for each solar experiment is shown at the top.

and after several years of running produced a result for the average capture rate of solar neutrinos of 2.56±0.25 SNU (remember that 1 SNU = 10^{-36}neutrino interactions per target atom per second). The big surprise was that the Standard Solar Models of the time predicted that Homestake should have seen about 8.1±1.2 SNU, over three times larger than the measured rate. This discrepancy became known as the Solar Neutrino Problem.

Kamiokande and Super-Kamiokande

The Kamiokande detector was built originally to detect proton decay which is one of the fundamental questions of elementary particle physics, later on at 1985 it was upgraded to allow it to observe solar neutrinos. As a result, it became sensitive enough to detect Supernova neutrinos , which indeed happened in 1987 in Large Magellanic Cloud. Super-Kamiokande was proposed, and it was built to be a 50

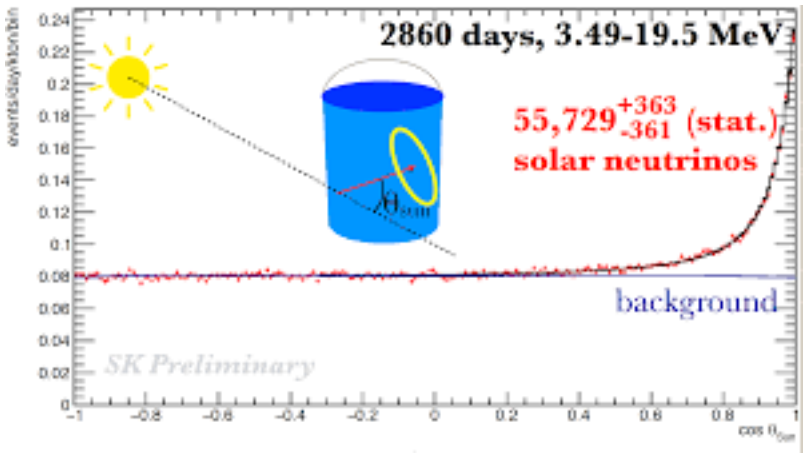

Figure 1.2: The angle between measured electron direction in Super-Kamiokande solar-neutrino data with respect to the direction to the Sun, a peak can be seen around 1. The broad spectrum is due to the kinematic smearing and multiple smearing of the electron.

kiloton detector which was 20 times of the size of Kamiokande, also got funding from US, who in addition contributed many PMTs from it's IMB experiment.

Different than Homestake, Super-K was able to directly detect outgoing electrons from its sensitive interaction channel elastic scattering which has a threshold of 5MeV:

$$\nu_a + e \rightarrow \nu_a + e \tag{1.18}$$

This threshold comes from the design of the detector - neutrinos with energies less than 5 MeV which elastically scatter in the water will not generate an electron with enough momentum to be seen in the detector. Super-Kamiokande observed a capture rate of about 0.45± 0.02 SNU, with a model prediction of 1.0 ± 0.2 SNU, almost a factor of two larger than observation. In addition, since Super-Kamiokande was able to reconstruct the direction of the incoming electron (with some large resolution due to both scattering kinematics - Super-Kamiokande sees the final state electron which isn't quite collinear with the incoming neutrino direction - and to multiple scattering of the final state electron - which smears the directional resolution out even more), it was able to show that the electron neutrinos do indeed come from the sun.

The Homestake experiment was simply a counting experiment and it couldn't detect electrons , neither prove the neutrino flux come from the Sun. But Super-K, this water Cerenkov experiment capable to directly prove them. However, it was basically measuring the disappearance of original ν_e flux from the sun, but not measure the new neutrino flavor which ν_e oscillated to. The solar neutrino energies are less than about 30 MeV, this is enough to allow both Neutral Current(NC) and Charged Current (CC) of electron neutrino interactions happen, but only NC of ν_μ and ν_τ to happen since the charged lepton μ need at least 105MeV to be generated, let alone the heavy τ. In later era, this problem would be solved by accelerator neutrino detectors. But here we'll introduce another experiment which was able to prove the existence of ν_μ and ν_τ and also their combined flux ratio to ν_e.

SNO experiment

The SNO experiment used a tank of 1000 tons of heavy water as its target. Similar to Super-K, SNO is also a water Cherenkov detector. The high speed electron moving in the water created the Cherenkov light, which was then detected by an array of 9600 photomultiplier tubes mounted on a geodesic support structure surrounding the heavy water vessel. Heavy water consists of D_2O with the deuteron containing a proton and a neutron, rather than just a proton (as in Hydrogen). The important point is that the deuteron is a very fragile nucleus. It only takes about 2 MeV to break it apart into a proton and a neutron. Solar neutrinos have energies up to 30 MeV and so any of the neutrino ν_e ν_μ ν_τ can break apart a deuteron in a neutral current interaction. SNO was able to detect the final state neutron and so all those neutrinos that weren't visible to the radiochemical or water Cerenkov experiments are visible to SNO.

In fact, SNO was able to detect neutrino via three different, and redundant, interactions:

- The Elastic Scattering (ES) channel :

$$\nu + e \rightarrow \nu + e \tag{1.19}$$

This is same channel used by super-K, both CC and NC of ν_e interaction would take place, and only NC of ν_μ and ν_τ was possible to happen. And due to the smaller cross section of ν_μ and ν_τ, the total interaction rate of ν_e is about six times of ν_μ and ν_τ:

$$\phi(\nu_e) + 0.15(\phi(\nu_\mu) + \phi(\nu_\tau)) \tag{1.20}$$

- The Charged Current (CC) channel :

$$\nu_e + d \rightarrow p + p + e^- \tag{1.21}$$

ν_e is the only flavor interact in this channel, therefore this channel can only measure $\phi(\nu_e)$.

- The Neutral Current (NC) channel :

$$\nu + d \rightarrow n + p + \nu \tag{1.22}$$

all three flavors of neutrino will have this interaction, it measures the total flux : $\phi(\nu_e) + \phi(\nu_\mu) + \phi(\nu_\tau)$

By measuring three independent channel, SNO was able to disentangle each individual fluxes of neutrinos. The measurement results, in units of 10^{-8} cm^{-2} s^{-1},

$$\phi_{ES} = \phi(\nu_e) + 0.15(\phi(\nu_\mu) + \phi(\nu_\tau)) = 2.39 \pm 0.26 \tag{1.23}$$

$$\phi_{CC} = \phi(\nu_e) = 1.76 \pm 0.01 \tag{1.24}$$

$$\phi_{NC} = \phi(\nu_e) + \phi(\nu_\mu) + \phi(\nu_\tau) = 5.09 \pm 0.63 \tag{1.25}$$

The total flux of muon neutrino and tau neutrino can be derived: $(3.33 \pm 0.63) \times 10^{-}8$ cm^{-2} s^{-1}, that's about twice of measured electron neutrino flux. This result is

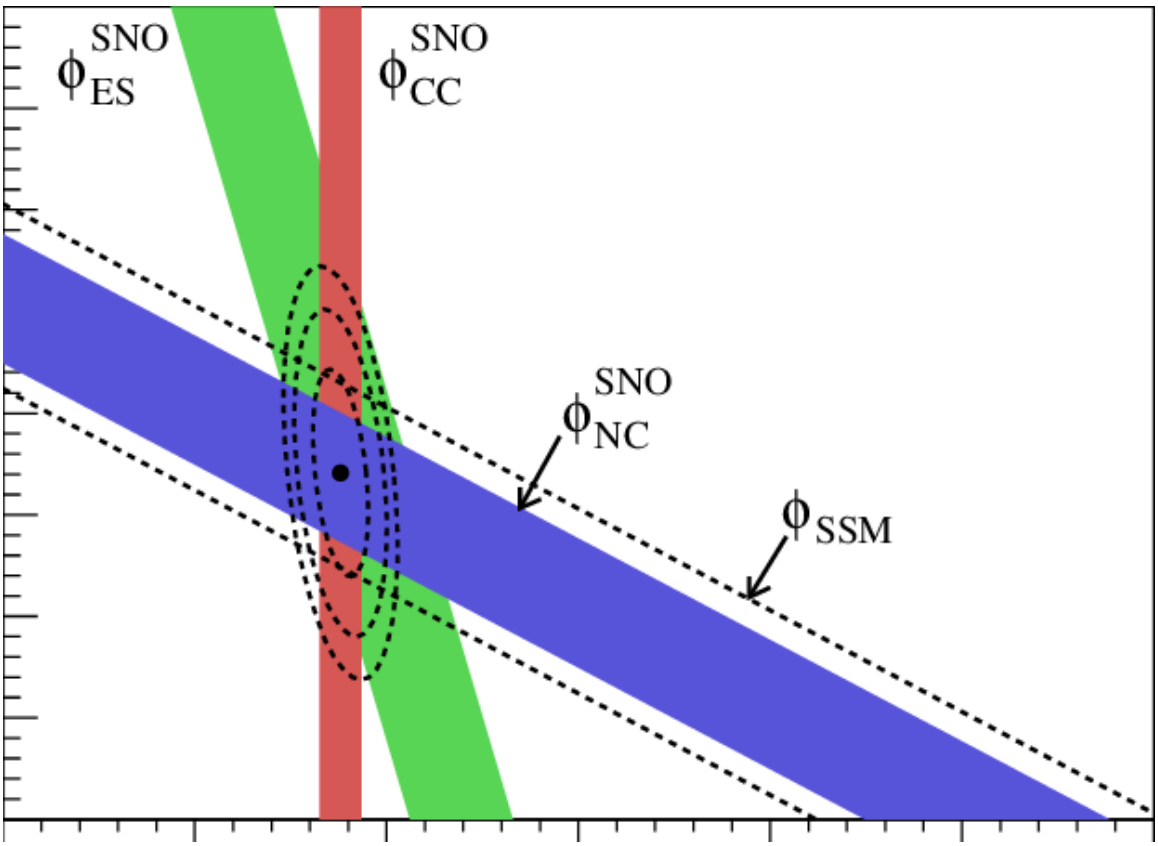

Figure 1.3: The three different channels that SNO is sensitive to

consistent with Homestake's experiment in which $\frac{2}{3}$ of electron neutrino disappeared according to SSM. So SNO experiment not only prove electron(solar) neutrino change flavor during its travel to Earth, but also directly measure the flavor it changed to.

With oscillation being proved, we can try to use PMNS matrix to see how the probability is calculated and measure the parameters the experiments are sensitive to. For solar neutrino experiments we just talked about, they are basically ν_e disappearance experiment which the experiment can measure how much electron neutrino disappear, but not how much other two flavors appear separately. From equation (1.15),

$$\begin{aligned} P(\nu_e \to \nu_e) = 1 - 4 \Big[& U_{e1}^2 U_{e2}^2 sin^2(1.27\Delta m_{12}^2 \frac{L}{E}) \Big] \\ & + U_{e1}^2 U_{e3}^2 sin^2(1.27\Delta m_{12}^2 \frac{L}{E}) \\ & + U_{e2}^2 U_{e3}^2 sin^2(1.27\Delta m_{12}^2 \frac{L}{E}) \end{aligned} \tag{1.26}$$

Before we proceed further, let's abbreviate $\Delta_{ij} = \Delta m^2_{ij} \frac{L}{E}$.

$$\begin{aligned} P(\nu_e \to \nu_e) &= 1 - 4\left[U^2_{e1}U^2_{e2}sin^2\Delta_{12} + U^2_{e2}U^2_{e3}sin^2\Delta_{23} + U^2_{e1}U^2_{e3}sin^2\Delta_{13}\right] \\ &= 1 - 4\left[c^2_{12}c^2_{13}s^2_{12}c^2_{13}sin^2\Delta_{12} + U^2_{e3}(U^2_{e2}sin^2\Delta_{23} + U^2_{e1}sin^2\Delta_{13})\right] \\ &= 1 - 4c^2_{12}s^2_{12}c^4_{13}sin^2\Delta_{12} - 4s^2_{13}(s^2_{12}c^2_{13}sin^2\Delta_{23} + c^2_{12}c^2_{13}sin^2\Delta_{13}) \\ &= 1 - \cos^4\theta_{13}sin^2(2\theta_{12})sin^2\Delta_{12} - 4s^2_{13}c^2_{13}(s^2_{12}sin^2\Delta_{23} + c^2_{12}sin^2\Delta_{13} \\ &= 1 - \cos^4\theta_{13}sin^2(2\theta_{12})sin^2\Delta_{12} - sin^2(2\theta_{13})(\sin\theta^2_{12}sin^2\Delta_{23} + \cos\theta^2_{12}sin^2\Delta_{13}) \end{aligned} \tag{1.27}$$

since $\Delta m^2_{13} \approx \Delta m^2_{23}$, we have:

$$P(\nu_e \to \nu_e) = 1 - \cos^4\theta_{13}sin^2(2\theta_{12})sin^2\Delta_{12} - sin^2(2\theta_{13})sin^2\Delta_{13} \tag{1.28}$$

From posterior experiments, we know θ_{13} is very small, in the precision level of old solar experiments, the third term could be neglected. And the equation becomes:

$$P(\nu_e \to \nu_e) = 1 - sin^2(2\theta_{12})sin^2(1.27\Delta m^2_{12}\frac{L}{E}) \tag{1.29}$$

measure $\Delta^2 m_{12}$ with reactors

The solar experiments don't do well on measuring $\Delta^2 m_{12}$. In order to check the solar oscillation analysis we need to make an experiment which is sensitive to $\Delta^2 m_{12} \approx 10^{-5} eV^2$. This can be done using reactors. The reactors produce electron anti-neutrinos with energies around 5 MeV. Using these as a source, one only requires a baseline of about 100 km.

The Kamioka Liquid-scintillator Anti-Neutrino Detector (KamLAND) experiment is situated in the old Kamiokande cavity in a horizontal mine drift in the Japanese Alps. The site is surrounded by 53 Japanese commercial power reactors, at a flux weighted average distance of ~180 km from the reactors.

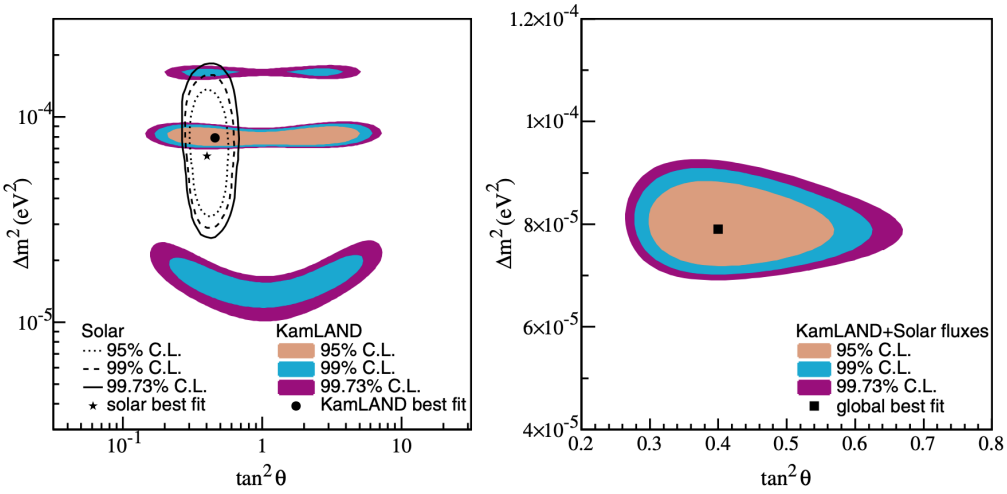

Figure 1.4: Left: Combined fitting to θ_{12} and $\Delta^2 m_{12}$ from solar neutrino experiment and Kamland. Right: Result of a combined two-neutrino oscillation analysis of KamLAND and observed solar-neutrino fluxes under the assumption of CPT invariance. The fit gives $\Delta^2_m = 7.9^{+0.6}_{-0.5} \times 10^{-5} eV^2$ and $\tan^2\theta = 0.40^{+0.10}_{-0.07}$. [28]

Electron anti-neutrinos are detected via the inverse β-decay reaction,

$$\bar{\nu_e} + p \rightarrow e^+ n \tag{1.30}$$

The prompt scintillation light from the e^+ gives an estimate of the incident anti-neutrino energy, $E_\nu = E_{prompt} + < E_n > +0.8 MeV$, where E_{prompt} is the prompt event energy including the positron kinetic energy and the e+e−annihilation energy. The quantity <En> is the average neutron recoil energy, which is only a few tens of keV. The neutron captures on hydrogen $\sim 200\mu s$ later, emitting a characteristic 2.2 MeV γ ray. This delayed coincidence signature is a very powerful tool for distinguishing anti-neutrinos from backgrounds produced by other particles.

The Kamland experiment's sensitivity to $\Delta^2 m_{12}$ can be shown by figure 1.4. A combined fitting using Kamland's data and solar experiments' data, the $\Delta^2 m_{12}$ and θ_{12} can be measured precisely.

1.3.2 Reactor antineutrino oscillation experiment with θ_{13}

Since θ_{13} is notoriously small. They are not measured until recent years. To measure θ_{13}, we need to take a deep look at equation:

$$P(\bar{\nu_e} \to \bar{\nu_e}) \approx P(\nu_e \to \nu_e) = 1 - \cos^4\theta_{13} sin^2(2\theta_{12}) sin^2\Delta_{12} - sin^2(2\theta_{13}) sin^2\Delta_{ee} \quad (1.31)$$

where $sin^2\Delta_{ee} = \sin\theta_{12}^2 sin^2\Delta_{23} + \cos\theta_{12}^2 sin^2\Delta_{13}$.

For Kamland or any solar neutrino experiments, the second term is large and the third term is relatively close to 0. If our precision to θ_{12} and $\Delta^2 m_{12}$ is not good enough, any attempt to measure θ_{13} will be very hard to succeed. The best way to independently measure θ_{13} without other parameters' interference is to make the second term as small as possible which make the third term becomes the dominant one. If this method is conducted in reactor experiment, then the detector has to be built very close to the neutrino source, around 1km. The three main currently going on experiments are Double Chooz in France, RENO in South Korea and Daya bay in China.

The Daya Bay experiment is most sensitive to θ_{13} among all the current reactor experiment[13]. Its nuclear-power complex contains six reactors which are grouped into three pairs with each pair referred to as a nuclear power plant(NPP). All six cores are viewed by 8 antineutrino detectors located in three different places. Each detector consists of 20 tons of liquid scintillator (linear alkylbenzene doped with gadolinium) surrounded by photomultiplier tubes and shielding. The location of the cores and the detectors are showed in figure 1.5. Daya bay started to take data at December 2011, and after 1958 days' data accumulation, it clearly showed the deficiency due to θ_{13} term which is small but not zero. The result [6] is:

$$\sin^2 2\theta_{13} = 0.0856 \pm 0.0029 \quad (1.32)$$

This shows the $\theta_{13} \approx 8.5°$.

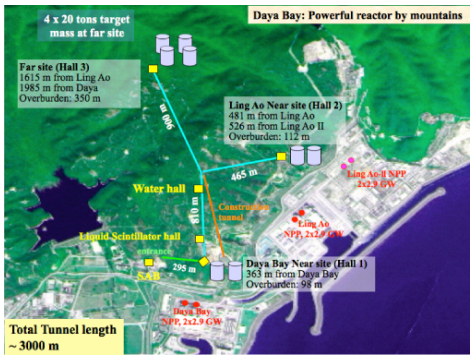

Figure 1.5: Location of Dayabay reactor 6 cores and 8 detectors

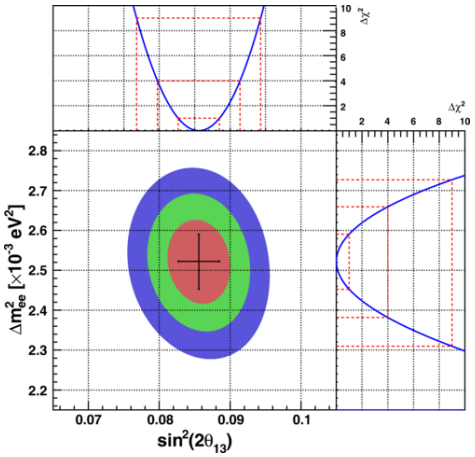

Figure 1.6: The fitting of θ_{13} and $\Delta^2 m_{ee}$ with Dayabay 1958 days' data [6]

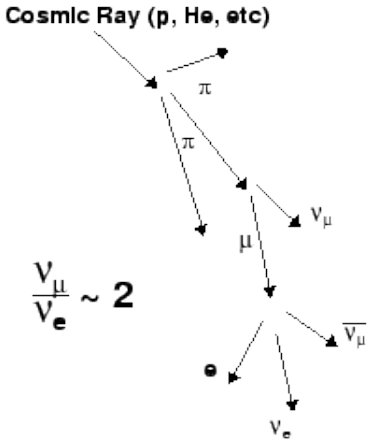

Figure 1.7: The cascade of cosmic rays

1.4 ATMOSPHERE NEUTRINO EXPERIMENT

The Earth atmosphere is constantly bombarded by cosmic rays. These are composed of protons (95%), alpha particles (5%) and heavier nuclei and electrons (< 1%). The primary cosmic rays interact with nuclei in the atmosphere , they shower and forms a cascade of hadrons. These hadrons decay during flight and neutrinos are generated. The dominant part of the decay chain is

Table 1.2: Measurements of the double ratio for various atmospheric neutrino experiments

Experiment	Type of experiment	R
Super-Kamiokande	Water Cerenkov	0.675±0.085
Soudan2	Iron Tracking Calorimeter	0.69±0.13
IMB	Water Cerenkov	0.54±0.12
Kamiokande	Water Cerenkov	0.60±0.07
Frejus	Iron Tracking Calorimeter	1.0±0.15

$$\begin{aligned} \pi^+ &\to \mu^+\nu_\mu \qquad \mu^+ \to e^+\nu_e\bar{\nu}_\mu \\ \pi^- &\to \mu^-\bar{\nu}_\mu \qquad \mu^- \to e^-\bar{\nu}_e\nu_\mu \end{aligned} \tag{1.33}$$

At higher energies, one starts to see kaon decay with emission of neutrinos as well. In general, the ratio:

$$R = \frac{\nu_\mu + \bar{\nu}_\mu}{\nu_e + \bar{\nu}_e} \tag{1.34}$$

should be equal to 2.

Since the Earth is surrounded by atmosphere, and neutrinos can easily cross the whole Earth without any interaction. Any detectors are supposed to see neutrinos coming from every direction. If the detector is sitting on the Earth's surface, the distance from where the neutrino generated to the detector range from shortest distance 15km (come from the top) to longest distance 13,000 km 9(come from down below on the other side of the planet).

Atmosphere neutrino detectors measure the ν_μ flux and ν_e flux separately and calculate the ratio. To help interpret the results and to cancel systematic uncertainties, the experiment normally use a double ratio:

$$R = \frac{(N_\mu/N_e)_{data}}{(N_\mu/N_e)_{sim}} \tag{1.35}$$

A compilation of R values from a number of different experiments is shown in Table 1.2.

With the exception of Frejus, all measurements of R are significantly less than 1, indicating that either there was less ν_μ in the data than in the prediction, or there was more ν_e , or both. This became known as the Atmospheric Neutrino Anomaly.

Super-Kamiokande was not only able to measure R, but also able to measure R as a function of angle, since it was able to measure the direction of the incoming neutrino by a not so bad of reconstruction of outgoing electron with its cherenkov radiation. In principle, we expect the neutrino flux to be isotropic. The zenith angle distributions from Super-Kamiokande are shown in figure : The left panel shows ν_e like events, right panel shows ν_μ like events. The red lines are the expectation from standard cosmic ray models, the black points are SuperK's measurements. The top and middle rows show sub GeV neutrino events, the bottom row shows multi-GeV neutrino events. For ν_e like events on the left, the superK data is more or less consistent with model prediction. However, the ν_μ like events from measurement are obviously less than the prediction, and when energy is high enough, the deficiency has a dependency on zenith angle. For neutrinos coming from the top($\cos\theta = 1$) , it's still consistent with prediction, but when zenith angle increase, the deficiency keep increasing.

Same as before, we can try to use PMNS matrix to explain then see what parameters the experiment is sensitive to.

$$\begin{aligned} P(\nu_\mu \to \nu_\mu) &= 1 - 4\left[U_{\mu 1}^2 U_{\mu 2}^2 sin^2\Delta_{12} + U_{\mu 2}^2 U_{\mu 3}^2 sin^2\Delta_{23} + U_{\mu 1}^2 U_{\mu 3}^2 sin^2\Delta_{13}\right] \\ &= 1 - 4U_{\mu 3}^2(U_{\mu 1}^2 + U_{\mu 2}^2) sin^2\Delta_{23} \\ &= 1 - 4U_{\mu 3}^2(1 - U_{\mu 3}^2) sin^2\Delta_{23} \\ &= 1 - 4c_{13}^2 s_{23}^2(1 - c_{13}^2 s_{23}^2) sin^2\Delta_{23} \\ &= 1 - 4s_{23}^2 c_{23}^2 sin^2\Delta_{23} \\ &= 1 - \sin^2(2\theta_{23}) sin^2\Delta_{23} \end{aligned} \tag{1.36}$$

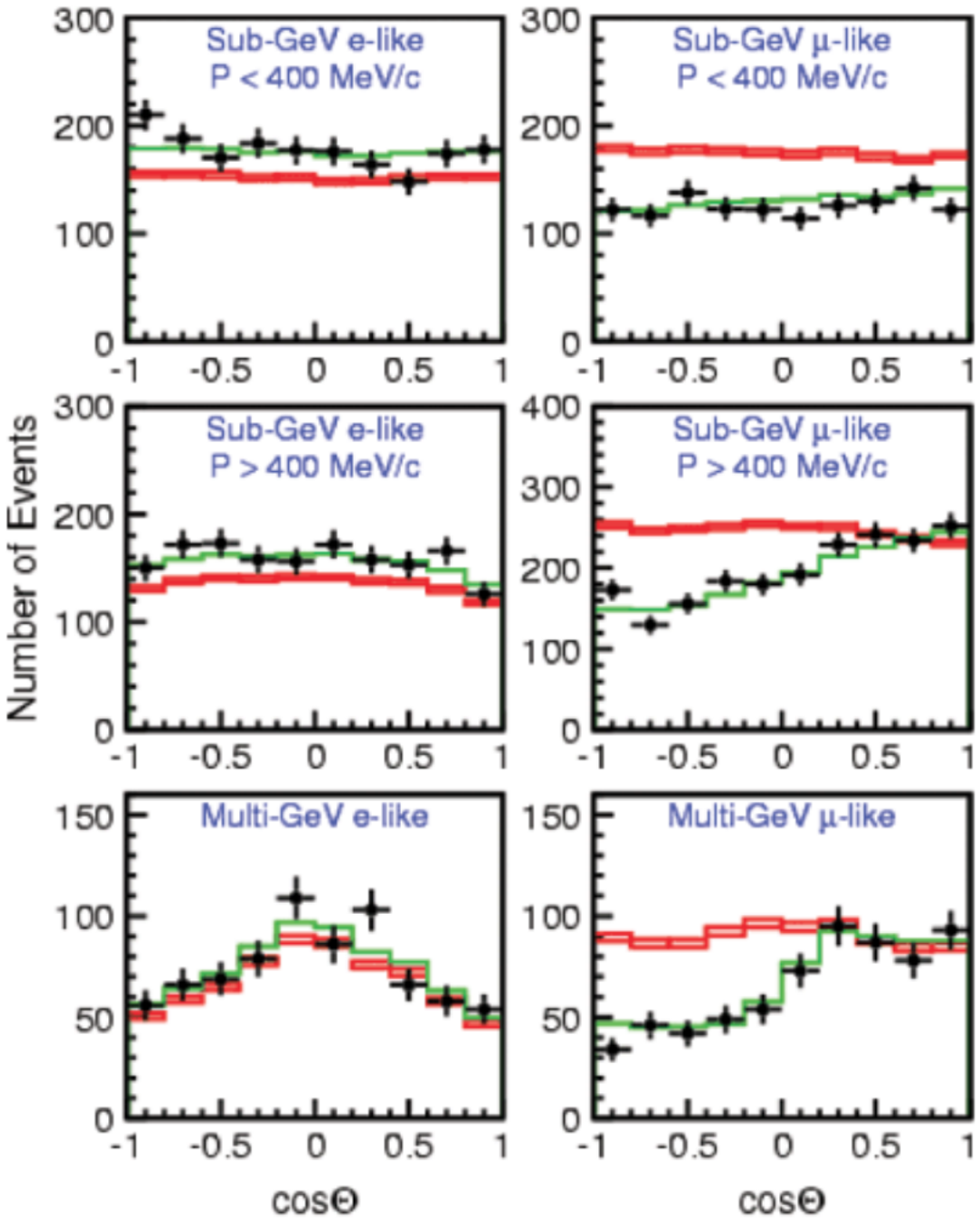

Figure 1.8: Zenith angle distribution of atmosphere neutrino events detected by Super-Kamiokande. The left panel shows ν_e like events, right panel shows ν_μ like events. The red lines are the expectation from standard cosmic ray models, the black points are SuperK's measurements. From top to bottom, neutrino energy increases.

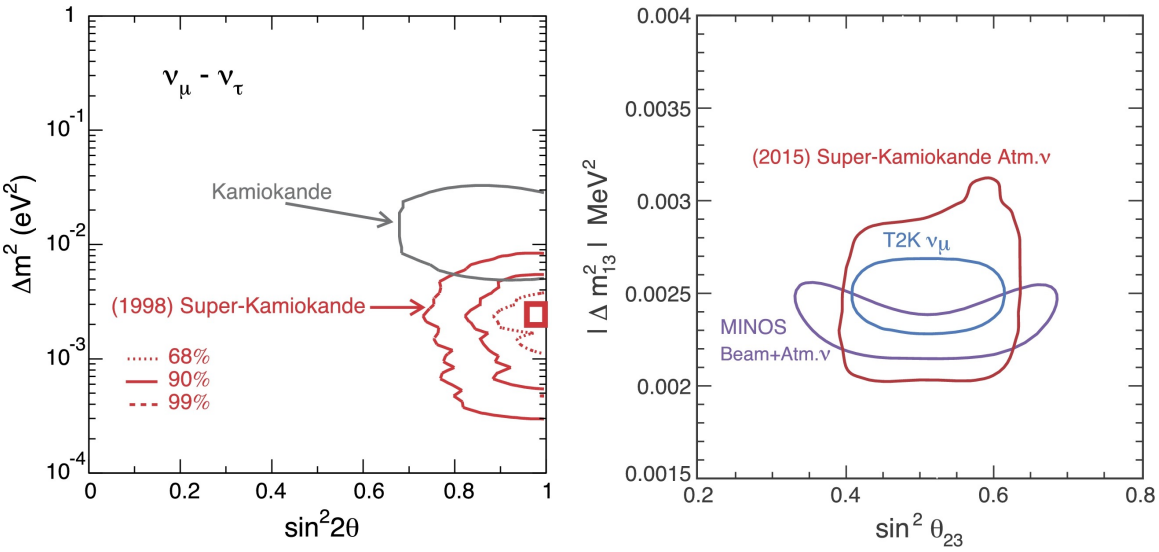

Figure 1.9: The left plot is based on the 1998 analysis of 33.0 kt-yr of Super-K data. The right plot contains the 90% confidence interval from a 2015 (preliminary) SK atmospheric oscillation analysis. This interval assumes normal hierarchy, and is compared to final results from MINOS and recent results from T2K. The bold inset square region on the left plot approximates the interval from the right plot for SK atmospheric neutrinos.[14]

The $sin^2\Delta_{12}$ is neglected due to the small distance (max is 13,000 km) and GeV-level energy. The $sin^2\Delta_{23}$ and $sin^2\Delta_{13}$ are combined due to their closeness. θ_{13} is approximated to zero since it's very small. Based on this equation and the super-K data, we are able to do a fitting and find the confidence interval of θ_{23} and Δm_{13}. Figure 1.9 shows the fitting result of super-K.

Chapter 2

Challenges Faced by Precision Oscillation Measurements

2.1 DUNE Sensitivities

There are two specific goals DUNE experiment intend to achieve regarding to neutrino oscillation measurements:

- Mass hierarchy determined with a significance of at least of 5σ for all δ_{cp} values using beam neutrinos.
- CP violation determined with high significance (for example: 5σ for 50% of δ_{cp} values or 3σ for 75% of δ_{cp} values).

where the sensitivities are defined as:

$$\begin{aligned}
\Delta\chi^2_{MH} &= \chi^2_{IH} - \chi^2_{NH}(\text{true normal hierarchy}),\\
\Delta\chi^2_{MH} &= \chi^2_{NH} - \chi^2_{IH}(\text{true normal hierarchy}),\\
\Delta\chi^2_{CPV} &= Min[\Delta\chi^2_{CP}(\delta^{test}_{CP}=0), \Delta\chi^2_{CP}(\delta^{test}_{CP}=\pi)], \text{where}\\
\Delta\chi^2_{CP} &= \chi^2_{\delta^{test}_{CP}} - \chi^2_{\delta^{true}_{CP}}.
\end{aligned} \tag{2.1}$$

Sensitivities to the mass hierarchy and the degree of CP violation are obtained by simultaneously fitting the $\nu_\mu \to \nu_\mu, \bar{\nu}_\mu \to \bar{\nu}_\mu, \nu_\mu \to \nu_e$ and $\bar{\nu}_\mu \to \bar{\nu}_e$ oscillated spectra. It is assumed that neutrino beam mode and antineutrino beam mode are 50%/50%, which has been shown to produce a nearly optimal sensitivity. The neutrino oscillation parameters are all allowed to vary, constrained by a Gaussian prior with 1σ width.The effect of systematic uncertainties are also included in the sensitivity search.

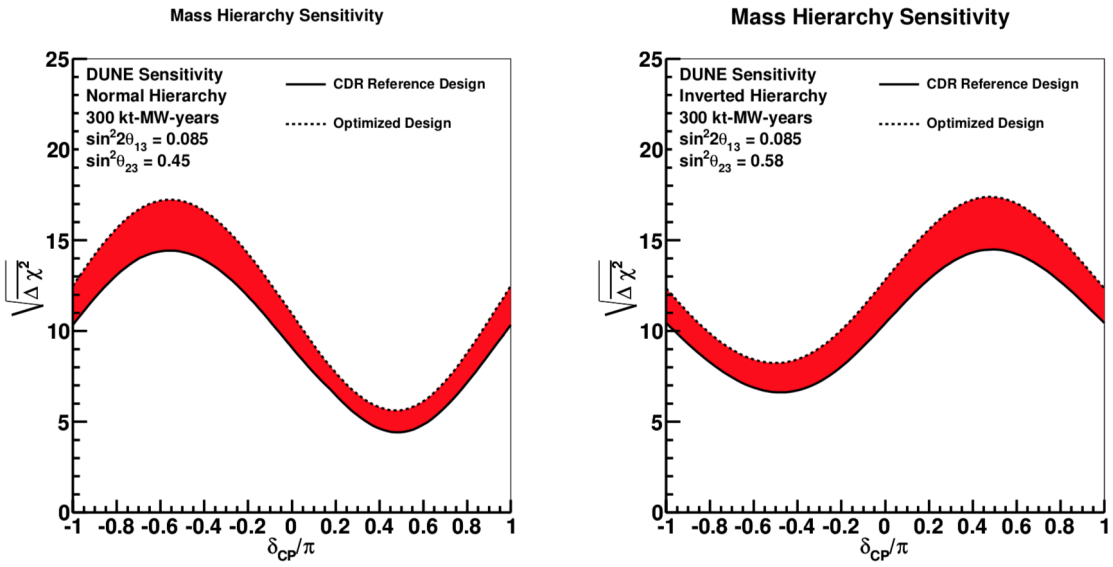

Figure 2.1: The significance of mass hierarchy as a function of the δ_{CP} value for an exposure of 300kt·MW·year assuming normal MH (left) or inverted MH(right). The shaded region represents the variation of sensitivity due to variations of beam design.

Assuming an exposure of 300kt·MV·year, which corresponds to a seven years of data taking(3.5 years in neutrino mode plus 3.5 years in antineutrino mode) with a 40-kt detector and a 1.07-MW 80-GeV beam, the significance of mass hierarchy as a function of δ_{CP} is shown in Figure 2.1 [18]. For same assumption, the significance of CP violation is shown in Figure 2.2[18].

There are many factors affecting the sensitivity of both mass hierarchy and CP violation besides fiducial mass, beam intensity and the number of years of data taking, one is the true values of every involved oscillation parameter, another is systematic uncertainties. For any experiment, the main systematic uncertainties are determined by the analysis strategy employed and the performance of the detector[20]. The typical analysis strategy for extracting oscillation parameters in long-baseline neutrino oscillation experiments is shown in Figure. Near detector is used to measure the un-oscillated ν_μ and ν_e flux, and then extrapolated to the far detector and are used to predict the oscillated flux and compare with data. The ν_μ disappearance and ν_e

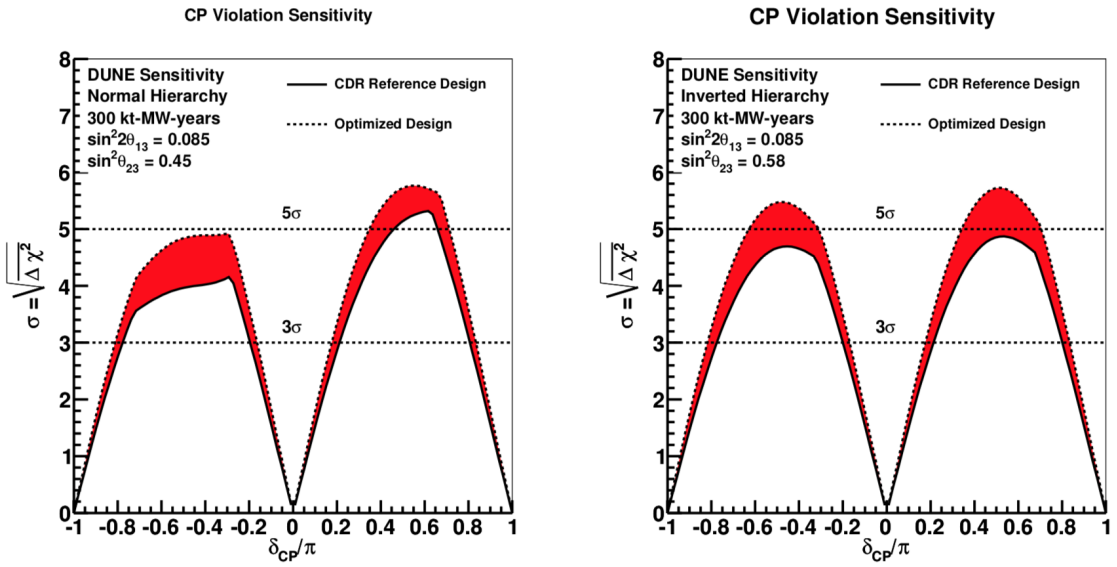

Figure 2.2: The significance of CP violation as a function of the δ_{CP} value for an exposure of 300kt·MW·year assuming normal MH (left) or inverted MH(right). The shaded region represents the variation of sensitivity due to variations of beam design.

appearance can be conducted separately and then combined to fit on the oscillation parameters.

In near detector, the measured spectrum of neutrino events is a product of 1, beam flux 2, detector efficiency and smearing, 3, neutrino interaction dynamics. In order to extrapolate the spectra in near detector to far detector, three corrections have to be made:

- Differences in the beam flux in the near and far detectors, Φ_{FD}/Φ_{ND}: The far detector sees the beam as a point source but near detector sees it as an extended source since it's much closer to the beamline. The beam never really gives off neutrino rays pointing to same direction, instead, it's diverged, as a result, near detector sees a greater divergence of the beam and far detector sees a less divergence of the beam.

- Differences in near and far detector smearing and efficiencies, $\epsilon_{FD}/\epsilon_{ND}$: The largest uncertainties are from the difference event selection efficiencies in the

near and far detectors, in particular, the energy scale. For ν_μ disappearance, most of these uncertainties can be cancelled, however, for ν_e appearance, the ν_e signal is extrapolated from $N_{ND}^{data}(\nu_\mu)$, and there are irreducible residual uncertainties from different selection of ν_μ and ν_e events and different detector response.

- Differences in the neutrino interactions of near and far detector. σ_{FD}/σ_{ND}: Most uncertainties can be cancelled in ν_μ disappearance, but uncertainties remain for ν_e appearance, i.e $\sigma_{FD}(\nu_e)/\sigma_{ND}(\nu_\mu)$.

The systematic uncertainties play a significant role in DUNE sensitivity to the CP violation or mass hierarchy. By varying one of the systematic uncertainty: signal normalization uncertainty from 5%⊕3% to 5%⊕1%, the differences can be found in Figure 2.3 [18].

2.2 The potential application of Coherent meson interaction for oscillation experiment

Coherent meson interactions are very special neutrino interaction channels where all nucleons in the same nucleus participate the interaction, as a result, the nucleus stays unbroken and in its ground state with little momentum gained. The interaction can be neutral charged where same neutrino comes in and comes out, at same time, a neutral meson is produced (π^0 or ρ^0), or charged current where a charged lepton and charged meson($\pi^{+/-}/\rho^{+/-}$) with opposite sign come out. Their Feynman diagrams are shown in Figure 2.4.

The first reason we want to study coherent meson interactions in an oscillation experiment is that the neutral charged coherent meson interaction could mimic ν_e signal and becomes one of the backgrounds. For neutral current coherent pion interaction, the meson π^0 exclusively decays to two gammas, if the two gammas are

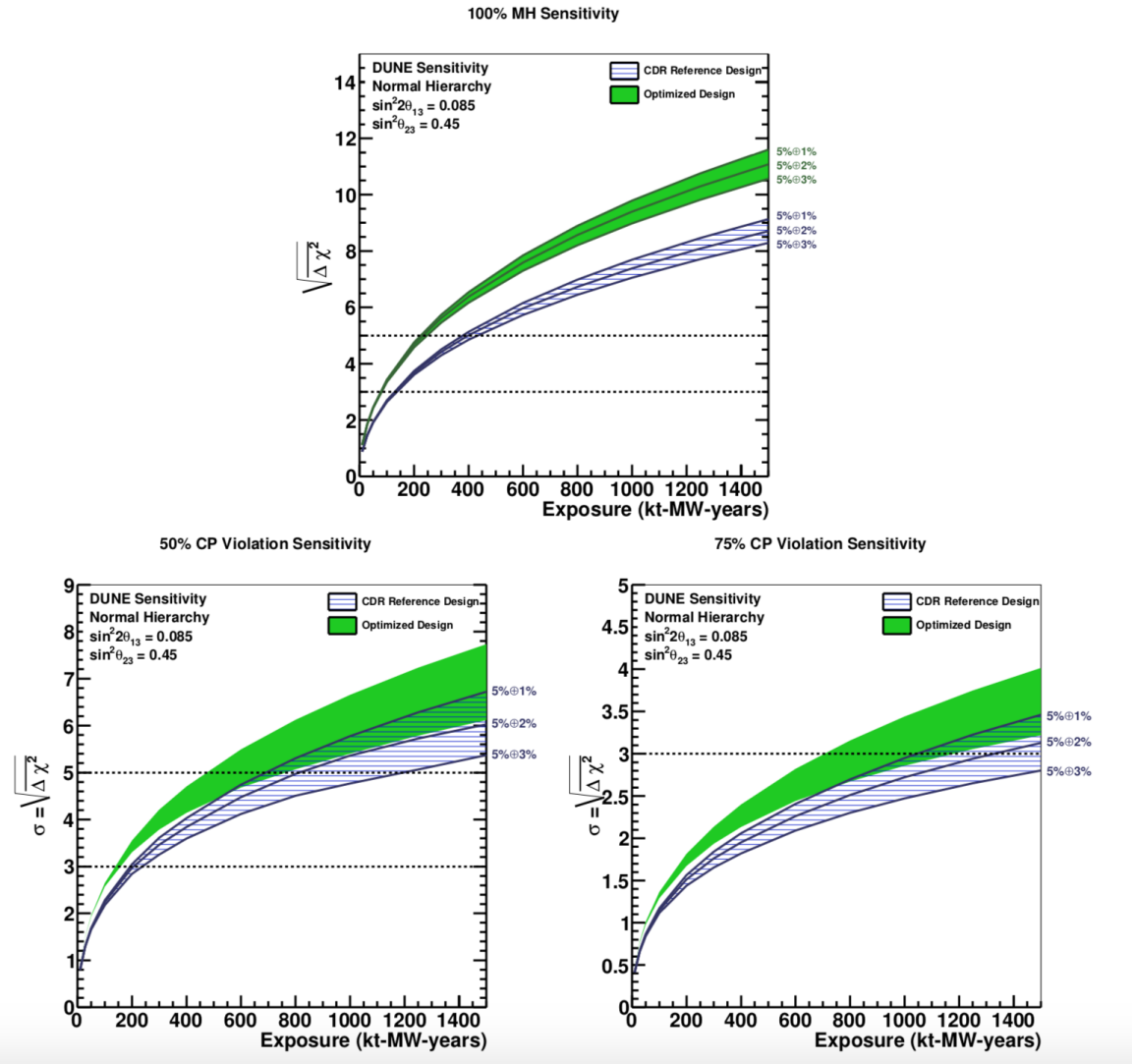

Figure 2.3: Predicted sensitivity of DUNE to determination of mass hierarchy (top panel) and CP violation as a function of exposure. Equal running in neutrino mode and antineutrino mode is assumed. The variations are for a range of values for ν_e and $\bar{\nu}_e$ signal normalization uncertainties from 5%⊕3% to 5%⊕1%. The sensitivities quoted are the minimum sensitivity for MH (top)under all δ_{CP} values, and 50% (bottom left) or 75%(bottom right) of δ_{CP} values for CP sensitivity. The blue hashed band is for the CDR Reference Design and the solid green band is for the Optimized Design.

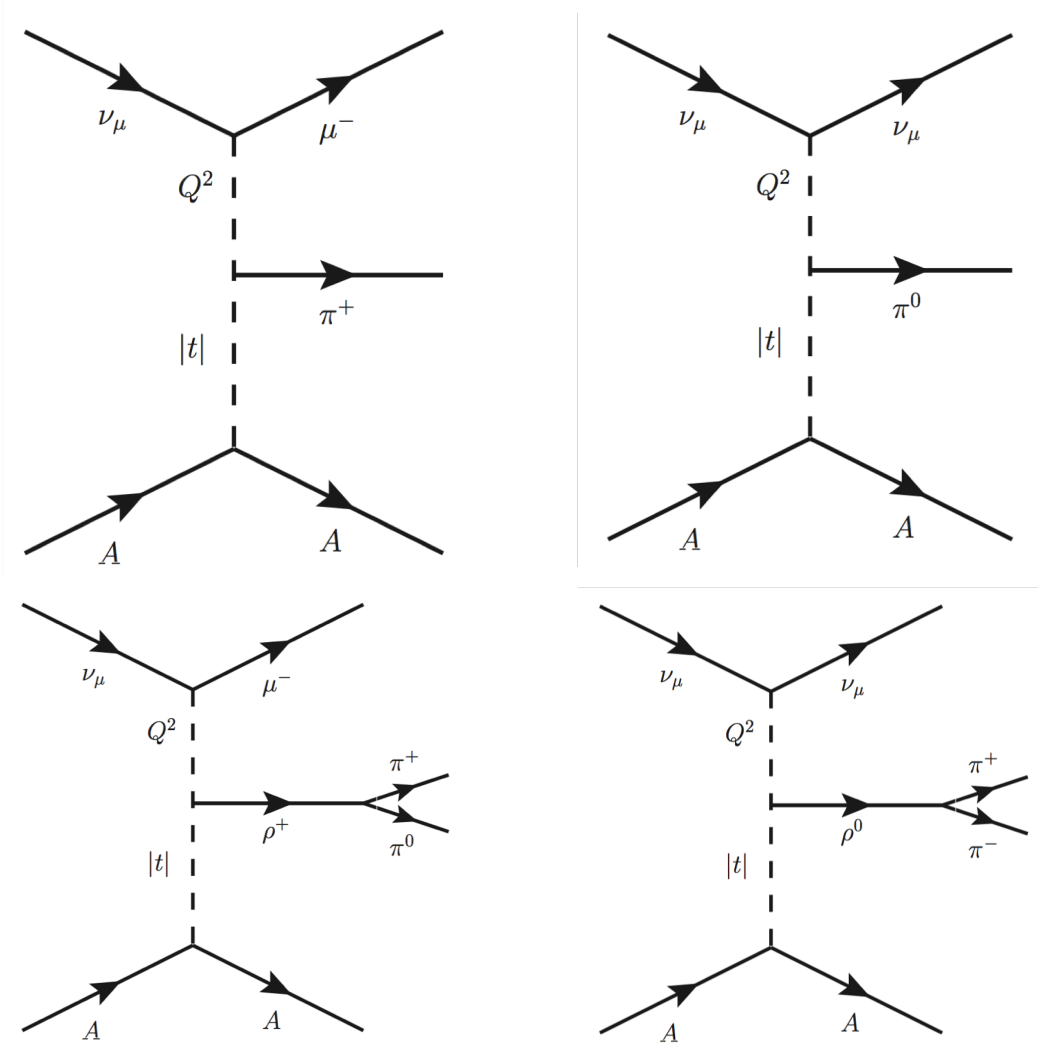

Figure 2.4: Feynman diagram for top left: charged current coherent π^+ interaction, top right: neutral current coherent π^0 interaction, bottom left: charged current coherent ρ^+ interaction, bottom right: neutral current coherent ρ^0 interaction.

collinear or one of the gamma inherit most of the energy from the π_0 in lab frame, which makes the other gamma unregistered in the detector, this large-energy gamma could be mis-identified as a electron, especially in a high-density detector. For neutral current coherent rho interaction, the meson ρ decays to $\pi^+\pi^-$, one of them could be mis-identified as an electron.

Secondly, Determination of $\nu/\bar{\nu}$ flux ratio. The measurement of $\nu/\bar{\nu}$ flux ratio is important for two reasons. First, to measure CP violation, DUNE is planned to

be operated half of time under neutrino mode and the other half under antineutrino mode, it eventually will combine data under both modes to do the oscillation parameters fitting. Secondly, under each neutrino beam mode, the correct-sign neutrinos are always coexist with wrong-sign neutrinos. However, for neutrino-nucleon interactions between neutrino and anti-neutrino, they differ in energy-scale, topologies, cross-section and nuclear effect[7], etc. This could seriously jeopardize the high precision goals required by DUNE. Coherent-meson interaction, according to its theoretical model, it has same cross section for neutrino and anti-neutrino interactions. The topologies are also the same for neutrino and anti-neutrino interactions. For example, coherent π^+ give off a μ^- and a π^+, coherent π^- give off a μ^+ and a π^-. And there's little nuclear effect for both neutrino and anti-neutrino interactions. With all these being considered, coherent-meson interaction offer a unique and powerful tool on measuring neutrino and anti-neutrino flux ratio.

Chapter 3

Coherent Pion Interaction Models

Before we talk about any theoretical models of coherent meson interaction, let's define some notations used in this chapter.

- E_ν and E_μ : The incoming neutrino and outgoing lepton's energy.
- p_ν and p_μ : The incoming neutrino and outgoing lepton's four-momentum.
- p and p' The four momentum of the initial and final state of hadronic system.
- q: The four-momentum transfer (out of leptonic system).
- ν: The energy transfer out of leptonic system.
- M: The target mass.
- Q^2: The negative of the square of the four-momentum transfer.

$$\begin{aligned} y &= \frac{\nu}{E_\nu} (\text{Bjorken y}) \\ x &= \frac{Q^2}{2p \cdot q} = \frac{Q^2}{2M\nu} (\text{Bjorken x}) \end{aligned} \tag{3.1}$$

3.1 Weak Interaction Scattering Amplitude

In most neutrino oscillation experiment, the mass of W boson is much larger than the mass of momentum transfer, the scattering amplitude of a neutrino CC interaction can be written as:

$$\mathcal{M} = \frac{G_f}{\sqrt{2}} j_w^\alpha w_\alpha \tag{3.2}$$

Where G_f is is the Fermi coupling constant, j_w^α is the weak leptonic current coupled with charged W boson, w_α is the corresponding hadronic current. The CC leptonic

current can be expressed as:

$$j_w^\alpha = \bar{\psi}_l \gamma^\alpha (1-\gamma^5)\psi_\nu \tag{3.3}$$

The form of the hadronic current is not the same as the leptonic one since the nucleon/nucleus is not a point particle but a composite system made of quarks and gluons/multiple nucleons. Generally it is expressed as:

$$w_\alpha = \bar{\psi}_p \gamma^\alpha (V_\alpha - A_\alpha)\psi_n \tag{3.4}$$

The V_α A_α here are the vector and axial-vector components of the current respectively. Combining the leptonic and hadronic currents we have:

$$\mathcal{M} = \frac{G_f}{\sqrt{2}} \bar{\psi}_l \gamma^\alpha (1-\gamma^5)\psi_\nu [V_\alpha - A_\alpha] \tag{3.5}$$

Where we have absorbed $\bar{\psi}_p$ and ψ_n into the definitions of V_α and A_α.

The square of the scattering amplitude gives:

$$\begin{aligned}
|\mathcal{M}|^2 =& \frac{G_f^2}{2} \bar{\psi}_l \gamma^\alpha (1-\gamma^5)\psi_\nu [V_\alpha - A_\alpha] \{\bar{\psi}_l \gamma^\beta (1-\gamma^5)\psi_\nu [V_\beta - A_\beta]\}^* \\
=& \frac{G_f^2}{2} \bar{\psi}_l \gamma^\alpha (1-\gamma^5)\psi_\nu [V_\alpha - A_\alpha][V_\beta^* - A_\beta^*] \bar{\psi}_\nu \gamma^\beta (1-\gamma^5)\psi_l \\
=& \frac{G_f^2}{2} \bar{\psi}_\nu \gamma^\beta (1-\gamma^5)\psi_l \bar{\psi}_l \gamma^\alpha (1-\gamma^5)\psi_\nu [V_\alpha - A_\alpha][V_\beta^* - A_\beta^*] \\
=& \frac{G_f^2}{2} Tr(\psi_\nu \bar{\psi}_\nu \gamma^\beta (1-\gamma^5)\psi_l \bar{\psi}_l \gamma^\alpha (1-\gamma^5))[V_\alpha - A_\alpha][V_\beta^* - A_\beta^*] \\
=& \frac{G_f^2}{2} Tr(\not{p}_\nu \gamma^\beta (1-\gamma^5)(\not{p}_\mu + m_\mu)\gamma^\alpha (1-\gamma^5))[V_\alpha - A_\alpha][V_\beta^* - A_\beta^*] \\
\equiv& \frac{G_f^2}{2} L^{\alpha\beta} W_{\alpha\beta}
\end{aligned} \tag{3.6}$$

In the middle, Casimir's trick is used. And spins are implicitly summed for incoming neutrino and outgoing lepton by equation:

$$\sum_{spins} u\bar{u} = \gamma^\mu p_\mu + mc \tag{3.7}$$

Normally the initial particles spins are averaged and the final particles spins are summed. But neutrinos are always left handed(anti-neutrinos are always right-

handed), so you won't see a 1/2 here. And we also defined:

$$\begin{aligned} L^{\alpha\beta} =& Tr(\not{p}_\nu \gamma^\beta (1-\gamma^5)(\not{p}_\mu + m_\mu)\gamma^\alpha (1-\gamma^5)) \\ W_{\alpha\beta} =& [V_\alpha - A_\alpha][V_\beta^* - A_\beta^*] \end{aligned} \tag{3.8}$$

Be aware the subscripts ν and μ represent the neutrino and the muon, not the four-vector indices. The leptonic tensor can be evaluated as:

$$L^{\alpha\beta} = 2\left[Tr(\not{p}_\nu \gamma^\beta \not{p}_\mu \gamma^\alpha + m_\mu Tr(\not{p}_\nu \gamma^\beta \gamma^\alpha) - Tr(\not{p}_\nu \gamma^\beta \gamma^5 \not{p}_\mu \gamma^\alpha) - m_\mu Tr(\not{p}_\nu \gamma^\beta \gamma^\alpha \gamma^5)\right] \tag{3.9}$$

The trace of any odd number of gamma matrices is zero so the second trace does not contribute. γ^5 contains an even number of gamma matrices, so if it is paired with an odd number of gamma matrices the trace is zero, so the last term does not contribute. And after using some "trace theorems" which you can find in most quantum field theory books, we are left with:

$$L^{\alpha\beta} = 8\left[p_\nu^\beta p_\mu^\alpha + p_\nu^\alpha p_\mu^\beta - (p_\nu \cdot p_\mu) g^{\alpha\beta} - i\epsilon^{\alpha\beta\lambda\sigma}(p_\nu)_\lambda (p_\mu)_\sigma\right] \tag{3.10}$$

If we can assume negligible lepton mass we'll have:

$$p_\nu \cdot p_\mu = \frac{Q^2}{2} (m_\mu \to 0) \tag{3.11}$$

If we take the low Q^2 limit, then, then the term $p_\nu \cdot p_\mu$ vanishes.

Since $Q^2 = 2E_\nu E_\mu(1-\cos\theta)$, in $Q^2 \to 0$ limit, $\theta \to 0$, muon is parallel with neutrino. So in this limit, $\vec{p_\nu}$ $\vec{p_\mu}$ and $\vec{q}$ all the three vectors are all parallel. And because we are neglecting muon mass for high energies, we can describe the lepton 4-vectors in terms of the 4-momentum transfer:

$$\begin{aligned} p_\nu =& (\frac{E_\nu}{\nu})q \\ p_\mu =& (\frac{E_\nu}{\mu})q \end{aligned} \tag{3.12}$$

So we can express the leptonic tensor in terms of q:

$$L^{\alpha\beta} = 8\frac{E_\nu E_\mu}{\nu^2}\left[q^\alpha q^\beta + q^\beta q^\alpha - i\epsilon^{\alpha\beta\lambda\sigma} q_\lambda q_\sigma\right] \tag{3.13}$$

The last term contains a anti-symmetric tensor, multiplied by a a term that is symmetric under the same exchange, so the term will vanish after summation.So we have our final form of the leptonic tensor as:

$$L^{\alpha\beta} = 16\frac{E_\nu E_\mu}{\nu^2} q^\alpha q^\beta \tag{3.14}$$

3.1.1 Hadronic tensor $W_{\alpha\beta}$

One of the fundamental postulates of quantum mechanics is the representation of momentum and energy as derivatives of space and time:

$$\begin{aligned} \vec{p} &\longrightarrow -i\vec{\Delta} \\ E &\longrightarrow i\partial_t \end{aligned} \tag{3.15}$$

Applying this to the classical equation of conservation of energy ($E = p^2/2m + V$), we immediately get the Schrödinger equation, and we can obtain the Klein-Gordon equation by applying it to the relativistic version. A simpler 4-vector way to describe the above relation is :

$$p^\mu = (E, \vec{p}) \longrightarrow i\partial^\mu = i(\partial_t, -\vec{\Delta}) \tag{3.16}$$

Considering the amplitude for a one particle pion state with momentum q,

$$\langle 0| J^\alpha(x) |\pi\rangle = \langle 0| e^{i\hat{P}x} J^\alpha(0) e^{-i\hat{P}x} |\pi\rangle = \langle 0| J^\alpha(0) |\pi\rangle e^{-iqx} \tag{3.17}$$

The derivative of this is:

$$\begin{aligned} \partial_\alpha \langle 0| J^\alpha |\pi\rangle &= \langle 0| \partial_\alpha (J^\alpha(0) e^{-iqx}) |\pi\rangle = \langle 0| - iq_\beta J^\alpha(0) e^{-iqx} \partial_\alpha x^\beta |\pi\rangle \\ &= \langle 0| - iq_\beta J^\alpha \partial_\alpha x^\beta |\pi\rangle = \langle 0| - iq_\beta J^\alpha \delta^\beta_\alpha |\pi\rangle \\ &= -iq_\alpha \langle 0| J^\alpha |\pi\rangle \end{aligned} \tag{3.18}$$

from this we can conclude:

$$\partial_\alpha J^\alpha = -iq_\alpha J^\alpha \tag{3.19}$$

which is in accordance with the fundamental postulate in (3.16). Furthermore, the square of the amplitude's derivative is :

$$|\partial_\alpha J^\alpha|^2 = (-iq_\alpha J^\alpha)(iq_\beta J^{\beta *}) = q_\alpha q_\beta J^\alpha J^{\beta *} = q_\alpha q_\beta W^{\alpha\beta} \tag{3.20}$$

Once we put the final form of leptonic tensor into the amplitude squared, we'll arrive at:

$$|\mathcal{M}|^2 = \frac{G_f^2}{2} 16 \frac{E_\nu E_\mu}{\nu^2} q^\alpha q^\beta W_{\alpha\beta} = 8 G_f^2 \frac{E_\nu E_\mu}{\nu^2} |\partial^\alpha (V_\alpha - A_\alpha)|^2 \tag{3.21}$$

By CVC we have $\partial^\alpha V_\alpha = 0$ at low Q^2, which leaves only the dependence on the axial-vector current in the amplitude squared.

$$|\mathcal{M}|^2 = 8 G_f^2 \frac{E_\nu E_\mu}{\nu^2} |\partial^\alpha A_\alpha|^2 (Q^2 \to 0 \& m_l = 0) \tag{3.22}$$

The PCAC hypothesis relates the divergence of the axial-vector current to the amplitude of the pion field, ϕ_π.

$$\partial_\lambda A^\lambda = f_\pi m_\pi^2 \phi_\pi \tag{3.23}$$

According to Adler using PCAC[40] and the Goldberger-Treiman relation we can equate the divergence of the axial-vector current with the corresponding scattering of a pion.

$$|\langle \beta | \, \partial_{lambda} A^\lambda \, | \alpha \rangle \, |^2 = f_\pi^2 |\mathcal{M}(\pi\alpha \to \beta)|^2 \tag{3.24}$$

putting this into our form of $|\mathcal{M}|^2$, we have:

$$|\mathcal{M}|^2 = 8 G_F^2 \frac{E_\nu E_\mu}{\nu^2} f_\pi^2 |\mathcal{M}(\pi\alpha \to \beta)|^2 \tag{3.25}$$

At this point we have related the weak neutrino interaction to pion nucleus scattering and we are in a good position to calculate the cross-section. According to Fermi's Golden rule on cross-section for one incoming particle hit on a static target:

$$\begin{aligned} d\sigma =& \frac{|\mathcal{M}|^2}{2E_\nu 2M} \left(\frac{d^3 p_\mu}{(2\pi)^3} \frac{1}{2E_\mu} \right) \left(\frac{d^3 p'}{(2\pi)^3} \frac{1}{2p'_0} \right) (2\pi)^4 \delta^4 (p_\nu + p - p_\mu - p') \\ =& \frac{G_F^2}{M\nu^2} f_\pi^2 |\mathcal{M}(\pi\alpha \to \beta)|^2 \left(\frac{d^3 p_\mu}{(2\pi)^3} \right) \left(\frac{d^3 p'}{(2\pi)^3} \frac{1}{2p'_0} \right) (2\pi)^4 \delta^4 (p_\nu + p - p_\mu - p') \end{aligned} \tag{3.26}$$

3.1.2 $d\sigma$ IN TERMS OF dQ^2 AND $d\nu$

We would now like to express $d\sigma$ in terms of dQ^2 and $d\nu$ rather than $d^3 p_\mu$. When ignoring the lepton mass, we have $Q^2 \approx 2EE'(1 - \cos\theta)$. take it's derivative:

$$dQ^2 = \left(\frac{\partial Q^2}{\partial \theta} \right) d\theta + \left(\frac{\partial Q^2}{\partial E'} \right) dE' \tag{3.27}$$

The initial energy is assumed to be fixed, so it's not included here. Now for $d\nu$ we have $d\nu = d(E - E') = dE - dE' \rightarrow d\nu = -dE'$, The minus sign seems troublesome, but it is a simple matter of changing the integration limits.

$$\int_0^E dE' = -\int_E^0 d\nu = \int_0^E d\nu \tag{3.28}$$

It is easier to understand in the way that when the outgoing lepton has zero energy then the full energy E has been transferred to the hadronic system. So it's totally safe to think $d\nu = dE'$, so we multiply the two sides with them respectively, we have:

$$dQ^2 d\nu = \left(\frac{\partial Q^2}{\partial \theta}\right) d\theta dE' + \left(\frac{\partial Q^2}{\partial E'}\right) (dE')^2 \tag{3.29}$$

The second term is too small to be integrated and we finally have:

$$dQ^2 d\nu = \left(\frac{\partial Q^2}{\partial \theta}\right) d\theta dE' = (2EE' \sin\theta) d\theta dE' \tag{3.30}$$

For d^3p we have:

$$\begin{aligned} d^3p =& |\vec{k}|^2 d|\vec{k}| d\Omega \approx E'^2 dE' d\Omega = 2\pi E'^2 dE' \sin\theta d\theta \\ =& \pi \frac{E'}{E} dQ^2 d\nu \end{aligned} \tag{3.31}$$

Use this equation to replace d^3p_μ in bla. We have:

$$d\sigma = \frac{G_F^2 E_\mu dQ^2 d\nu}{2\pi^2 \nu E_\nu} f_\pi^2 \left[\frac{|\mathcal{M}(\pi\alpha \rightarrow \beta)|^2}{2M2\nu} \left(\frac{d^3p'}{(2\pi)^3} \frac{1}{2p'_0}\right) (2\pi)^4 \delta^4(p_\nu + p - p_\mu - p') \right] \tag{3.32}$$

Now we want to replace the amplitude of the pion scattering process with the cross-section of it. We will have the same target α with 4-momentum p=(M,0,0,0), the same final hadron state β with 4-momentum p', and an initial pion with 4-momentum $(p_\nu - p_\mu$. We will assume the relative velocity can be approximated as unity when either the initial pion is off-shell by an amount on the order of its mass, or we are assuming a very high energy pion where its mass is negligible. To reiterate, we must take the 4-vector of the initial pion to be the difference of the lepton 4-vector.

$$p_\pi = p_\nu - p_\mu \longrightarrow E_\pi = yE_\nu \tag{3.33}$$

With this, we can find out the cross-section for the pion scattering process:

$$d\sigma(\pi\alpha \to \beta) = \left[\frac{|\mathcal{M}(\pi\alpha \to \beta)|^2}{2M2\nu}\left(\frac{d^3p'}{(2\pi)^3}\frac{1}{2p'_0}\right) \times (2\pi)^4\delta^4(p_\nu + p - p_\mu - p')\right] \tag{3.34}$$

Comparing this cross-section with neutrino cross-section we arrived a while ago, everything in the brackets are exactly the same, so we finally have:

$$\left.\frac{d^2\sigma(\nu\alpha \to \mu\beta)}{dQ^2d\nu}\right|_{Q^2\to 0} = \left(\frac{G_F^2 f_\pi^2(1-y)}{2\pi^2\nu}\right) d\sigma(\pi\alpha \to \beta)|_{E_\pi = yE_\nu} \tag{3.35}$$

This expression is known as Adler's theorem[40], it relates the weak neutrino-nucleus cross-section to that of the strong pion-nucleus cross-section.

3.1.3 Antineutrino cross-section

It should be very quick to find out that the antineutrino cross-section is identical to its neutrino counterpart, i.e.

$$\sigma(\bar{\nu}\alpha \to \mu\beta) = \sigma(\nu\alpha \to \mu\beta) \tag{3.36}$$

3.1.4 The Neutral Current Cross-Section

For the neutral current,, one simply need to replace the pion's decay constant due to isospin.

$$f_{\pi^0} = \frac{f_{\pi^\pm}}{\sqrt{2}} \tag{3.37}$$

So the cross section simply becomes:

$$\left.\frac{d^2\sigma(\nu\alpha \to \mu\beta)}{dQ^2d\nu}\right|_{Q^2\to 0} = \left(\frac{G_F^2 f_\pi^2(1-y)}{4\pi^2\nu}\right) d\sigma(\pi\alpha \to \beta)|_{E_\pi = yE_\nu} \tag{3.38}$$

So the NC cross-section is simply half of the CC cross-section. This quantity is often given in terms of Bjorken variables x and y. Let's work on it. From the definition of x and y, we have:

$$\begin{aligned} Q^2 &= 2M\nu x \\ \nu &= E_\nu y \end{aligned} \tag{3.39}$$

Take the derivatives of them we'll have($dE_\nu = 0$):

$$\begin{aligned} dQ^2 =& 2M\nu dx + 2Mxd\nu \\ \nu =& E_\nu dy \end{aligned} \tag{3.40}$$

so, we'll have:

$$\begin{aligned} dQ^2 d\nu =& (2M\nu dx + 2Mxd\nu)(E_\nu dy) \\ =& (2ME_\nu y dx + 2MxE_\nu dy)(E_\nu dy) \\ \overset{(dy)^2=0}{=}& 2ME_\nu^2 y dx dy \end{aligned} \tag{3.41}$$

Take this into the cross section equation and after some organization, we final have our cross-section:

$$\left.\frac{d^3\sigma(\nu\alpha \to \nu\pi^0\alpha)}{dxdydt}\right|_{Q^2=0} = \left(\frac{G_F^2 f_\pi^2 ME_\nu(1-y)}{2\pi^2}\right)\left[\frac{d\sigma(\pi\alpha \to \pi\alpha)}{dt}\right]_{E_\pi = yE_\nu} \tag{3.42}$$

3.1.5 Rein and Sehgal Model

The cross-section for coherent pion production derived from Adler's so far has assumed that $Q^2 = 0$. Rein and Sehgal model[39] extended it to non-zero Q^2, and used pion-nucleon scattering to model the pion-nucleus cross-section. Rein and Sehgal introduced a form factor to transit the cross-section from zero Q^2 to non-zero Q^2 :

$$\frac{d^3\sigma(\nu\mathcal{A} \to \nu\pi^0\mathcal{A})}{dxdydt} = \left(\frac{G_F^2 f_\pi^2 ME_\nu(1-y)}{2\pi^2}\right)\left(\frac{M_A^2}{M_A^2+Q^2}\right)^2\left[\frac{d\sigma(\pi\mathcal{A} \to \pi\mathcal{A})}{dt}\right] \tag{3.43}$$

To model the pion-nucleus cross-section, the authors used forward pion-nucleon scattering:

$$\frac{d\sigma(\pi\mathcal{A} \to \pi\mathcal{A})}{d|t|} = A^2|F_\mathcal{A}(t)|^2 \left.\frac{d\sigma(\pi^0 N \to \pi^0 N)}{d|t|}\right|_{t=0} \tag{3.44}$$

where $F_\mathcal{A}(t)$ is the nuclear form factor and A is the number of nucleons within the nucleus. With the optical theorem, we have:

$$\frac{d\sigma(\pi N \to \pi N)}{d|t|} = \frac{1}{16\pi}\left[\sigma_{tot}^{\pi^0 N}\right]^2(1+r^2); \qquad r = \frac{Re(f_{\pi N}(0))}{Im(f_{\pi N}(0))} \tag{3.45}$$

$f_{\pi N}(0)$ is t he $\pi - N$ forward amplitude and $\sigma_{tot}^{\pi^0 N}$ gives the total cross-section for $\pi - N$ scattering. The nuclear form factor is modeled with an exponential:

$$|F_{\mathcal{A}}(t)|^2 = e^{-b|t|} F_{abs}; \qquad b = \frac{1}{3}R^2; \qquad R = R_0 A^{1/3} \tag{3.46}$$

where F_{abs} representing the effects of pion absorption in the nucleus. R is the nuclear radius and R_0 is 1.12fm. By combining all the above we have our final R.S. formula:

$$\frac{d\sigma}{dxdyd|t|} = \frac{G_F^2 M}{2\pi^2} f_\pi^2 A^2 E_\nu (1-y) \frac{1}{16\pi} \left[\sigma_{tot}^{\pi^0 N}(E_\nu y)\right]^2 (1+r^2) \left(\frac{M_A^2}{M_A^2 + Q^2}\right)^2 e^{-b|t|} F_{abs} \tag{3.47}$$

The absorption factor can be estimated by

$$F_{abs} = e^{-<x>/\lambda} \tag{3.48}$$

where <x> is the average path length traversed by a π^0 produced in nucleus, and λ is the absorption length defined in terms of the pion-nucleon inelastic cross-section and the nuclear density ρ by $\lambda^{-1} = \sigma_{inel}\rho$ where $\rho = A(4/3\pi R^3)^{-1}$. Finally we get:

$$F_{abs} = e^{-\frac{9A^{1/3}}{16\pi R_0^2}\sigma_{inel}} \tag{3.49}$$

R.S. model agrees very well with data for neutrino energy above 2GeV. For NOMAD experiment, of which the average energy is 25GeV, this is adequate for the precision we needed on coherent pion cross-section measurement. However, in the era of precise oscillation measurement, the neutrino energy centers around only a few GeV, correction of R.S model or different methods are needed for this low energy challenge.

3.1.6 Berger Sehgal

Berger Sehgal model[25] is proposed to solve the low energy issue suffered by Rein and Sehgal model. In resonance region, the derivation 3.44 and 3.49 based on simple classical ansatz may not be a valid estimation of pion-nucleus scattering. To circumvent the uncertainties in modelling nuclear processes, Berger model directly appeal

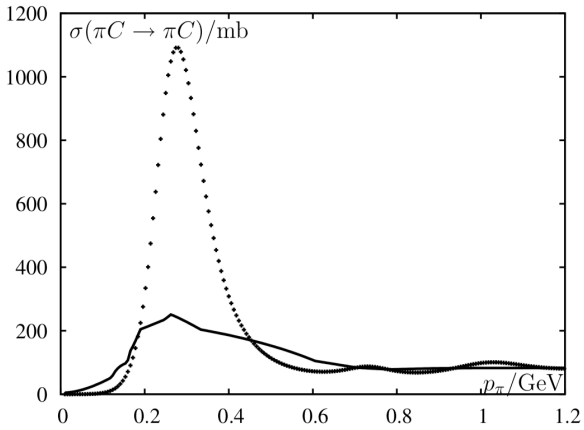

T_π GeV	A_1 mb/GeV^2	b_1 1/GeV^2
0.076	11600	116.0
0.080	14700	109.0
0.100	18300	89.8
0.148	21300	91.0
0.162	22400	89.2
0.226	16400	80.8
0.486	5730	54.6
0.584	4610	55.2
0.662	4570	58.4
0.776	4930	60.5
0.870	5140	62.2

Figure 3.1: Total elastic pion Carbon cross section versus pion laboratory momentum. Left: The dotted line represents the Rein-Sehgal model, solid line represented the BS model by fitting with pion Carbon data. Right: The fitting result of the coefficients A1,b1 from BS equation. [25]

to data on pion nucleus elastic scattering. They found out the elastic πp cross section can be simply parametrized by:

$$\frac{d\sigma(\pi\mathcal{A} \to \pi\mathcal{A})}{d|t|} = A_1 e^{-b_1 t} \tag{3.50}$$

where coefficients A1, b1 can be fitted by external data. The result based on the fitted equation is show in figure 3.1, in comparison with Rein-Sehgal model's prediction. It is obvious that the cross section from Berger Sehgal's fitting with pion Carbon data is much below the RS model. And when P_π approaches 1 GeV, the two curves become consistent which justify the ansatz. It also suggests that the RS model fails in the region of the Δ resonance, but may be a valid description at higher energies.

Chapter 4

The NOMAD Experiment

The NOMAD experiment [31] took data in CERN SPS wide-band neutrino beam from 1995 to 1998. It collected 2.2 $\times 10^{19}$ POT, more than one million charged current ν_μ events were detected and reconstructed with an accuracy which could only be achieved by bubble chambers previously.

The NOMAD detector was designed to search ν_μ to ν_τ oscillation. A few theoretical models suggested ν_τ may have a mass of 1eV/c^2 or higher, and therefore could be the main constituent of the dark matter. Even though no oscillation was observed due to too small mass difference which was not expected, it still restrained the oscillation probability of ν_μ to ν_τ down to more than one order of magnitude smaller than limits set by the previous generation of experiments. For the first time a purely kinematical approach was applied to the detection of ν_τ CC interactions. This demonstrated that the approach developed into a mature technique.

4.1 Beam and Flux Measurement

The NOMAD detector was exposed to the SPS wide-band neutrino beam consisting mainly of ν_μ. The neutrinos were produced from the in-flight decays of mesons such as $\pi^\pm$, $K^\pm$ which were secondary particles created from the 450GeV protons impinging on a beryllium target. The $\pi^\pm$ and $\kappa^\pm$ are focused by two magnetic lenses, the horn and the reflector, and later entering a 290m vacuum tunnel for decaying into neutrinos. The survived hadrons and muons are stopped by iron and earth shields. The NOMAD detector was located 835 m downstream. The average distance between

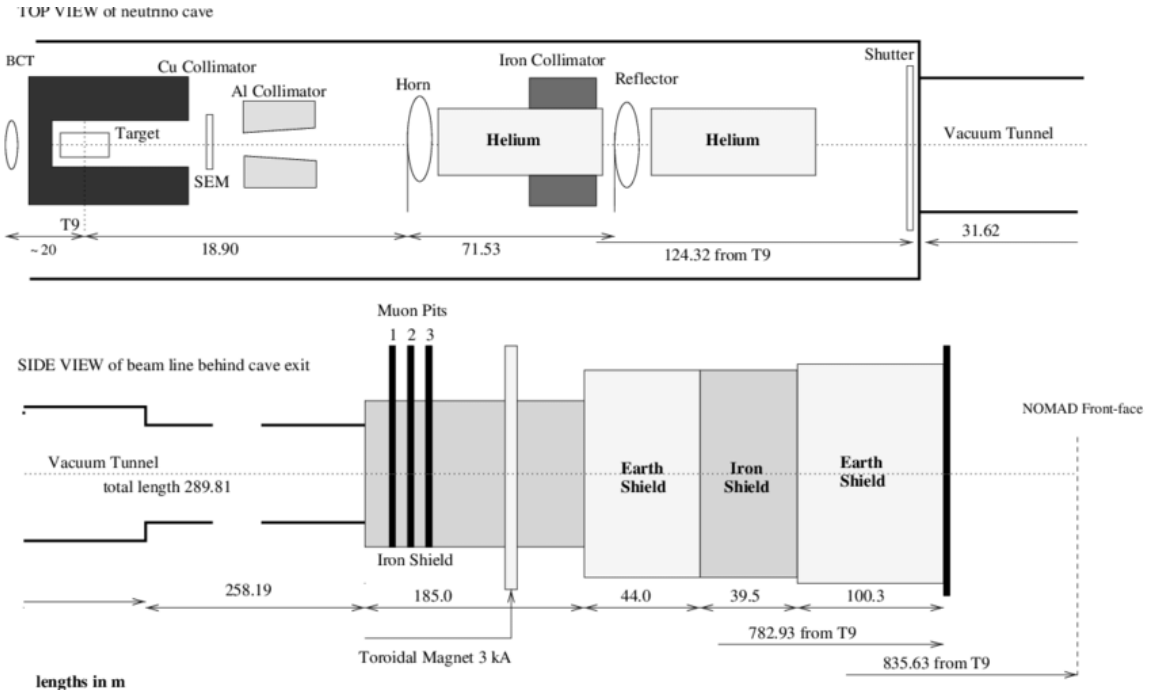

Figure 4.1: Schematic layout of the West Area Neutrino Facility (WANF) beam line.

the meson decay points and NOMAD was 620 m. A schematic layout for the beam line is shown in figure 4.1.

A neutrino beam monitoring system based on the detection of muon yields at several depths into the iron shield was also built . Silicon detectors provided an absolute flux measurement. Another independent measurement of the flux was given by the number of protons incident on the target, the POT is estimated from a pair of beam current transformers (BCT) upstream of the target.

The neutrino flux is predicted by a detailed GEANT4 simulation of beam line. The simulation predicted the relative abundance of neutrino species $\nu_\mu : \bar{\nu_\mu} : \nu_e : \bar{\nu_e}$ = 1.00 : 0.061 : 0.0094 : 0.0024 with average energies of 23.5, 19.2, 37.1, and 31.3 GeV, respectively. The detailed distribution is shown in figure 4.2. The prompt ν_τ contamination is also evaluated and found to be negligible comparing to the sensitivity of the experiment.

During the four years of data taking, 1995-1998, NOMAD collected a total of 2.2 $\times 10^{19}$ protons incident on the target (POT).

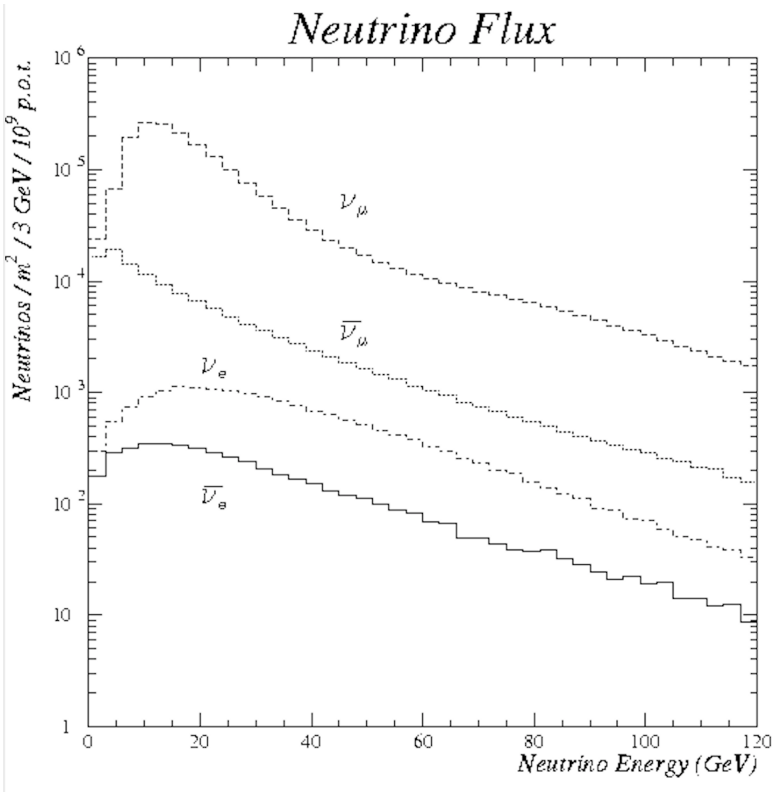

Figure 4.2: Predicted Neutrino Flux for NOMAD

4.2 DETECTOR

The detector is showed in Figure 4.3. The coordinate system used for NOMAD had the x-axis into the plane of the figure, the y axis directed upwards and z-axis horizontal to the right. The beam line is approximately along the z-axis but with a 2.4^o upwards. The main components of the detector are surrounded by a dipole magnet which created a magnetic field along x-axis with value 0.4T. The inner volume of the magnet is 7.5m along z and 3.5×3.5 along transverse plane.

The components along z-axis from upstream to downstream are a veto counter system, a front calorimeter, drift chambers, a transition radiation detector, a preshower, an electromagnetic calorimeter, a hadron calorimeter, and an iron filter consisting in the return-yoke of the magnet and a set of large drift chambers used for muon

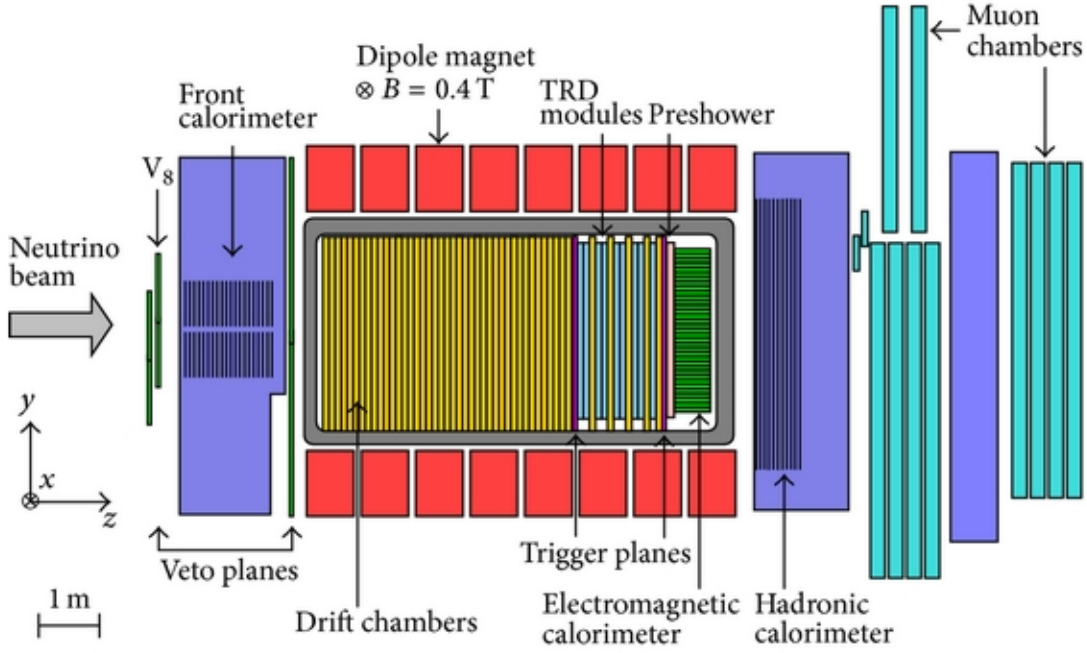

Figure 4.3: A side view of NOMAD detector and it's structure.

identification. Upstream and downstream of the transition radiation detector, two large hodoscopes of scintillators provided a fast trigger.

The veto counters

The 59 scintillation counters are at the upstream of the whole detector to reject the charged particles crossing through. These are either produced by neutrino interaction within the upstream material such as iron magnet support, rock, or cosmic rays traveling in every possible direction.The charged particle rejection efficiency of the veto system was constantly monitored and remained stable at a level of 96-97%.

The Front Calorimeter (FCAL)

FCAL provides additional massive active target for neutrino interactions. it had a depth of about 5 nuclear interaction lengths and a total mass of about 17.7 tons. A minimum ionizing particle(MIP) traversing the whole FCAL had an equivalent

hadronic energy of 430 MeV. The FCAL was particularly useful for the study of charm dimuon production.

The Drift Chambers (DC)

DC provides both tracking and target. They were designed with conflicting requirements that the material has to be as heavy as possible to maximize the number of neutrino interactions and as light as possible to minimize multiple scattering and secondary interactions. The complete target consisted of 145 drift chambers, with a 2.9 tons over a fiducial area of 2.6×2.6 m^2. Each chamber contributed 0.02 X_0. Overall, the target had a density of 0.1 g/cm3 and a total length of 1.0 X_0; The fiducial mass of the NOMAD drift chamber, composed mainly of carbon (64%), oxygen (22%), nitrogen (6%), and hydrogen (5%), was 2.7 tons. The measured composition of the target was 52.43% protons and 47.57% neutrons. The correction for non-isoscalarity was about 5%.

Each chamber is made of 4 3×3m^2 aramid-fiber panels sandwiched by Kevlar-epoxy resin skins. The three 8 mm gaps between the panels were filled with an argon-ethane (40%–60%) mixture at atmospheric pressure.

The central gap was equipped with sense wires at 5° and −5° with respect to the magnetic field direction. These sense wires were 20 μm in diameter and were made of gold-plated tungsten. They were interleaved with 100 μm potential wires made of Cu-Be. The momentum resolution provided by the drift chambers was a function of momentum and track length. For charged hadrons and muons traveling normal to the plane of the chambers, it was parameterized as

$$\frac{\sigma_p}{p} \sim \frac{0.05}{\sqrt{L}} + \frac{0.008p}{\sqrt{L^5}} \tag{4.1}$$

The Transition Radiation Detector (TRD)

The TRD was designed to separate electrons from pions with a pion rejection factor greater than 10^3 for a 90% electron efficiency in the momentum range from 1 to

50 GeV/c. In order to be able to extrapolate track from the drift chamber to the calorimeter, five drift chambers were embedded in the TRD, one after each TRD doublet and one after the last module.

Each TRD module is made by a radiator block followed by a detection plane. The radiator block was a set of 315 polypropylene foils, each 15 μm thick and 2.85 $\times$ 2.85 m^2 in area, separated by 250 μm air gaps. The foils were stretched on an aluminum frame and embossed to ensure a regular spacing in spite of their large size and electrostatic effects. The detection plane consisted of 176 vertical straw tubes, each 3 m long and 16 mm in diameter, separated by 0.2 mm. The straw tubes were fed in parallel with a xenon-methane (80%–20%) gas mixture. They were made of two shifted 12.5 μm thick ribbons of aluminized mylar rolled and glued along a 16 mm diameter helix. The sensitive anode was a 50 μm diameter gold-plated tungsten wire stretched with a tension of 100 g.

The Preshower Detector (PRS)

The Preshower detector was installed for the purpose of enhancing photon conversion and improve electron/pion separation.It was located just in front of ECAL, consists of a lead-antimony converter followed by two planes of proportional tubes. One plane has 286 horizontal tubes and the other has 288 vertical tubes. Each aluminum proportional tube is 9mm wide and fitted with a 30μm-diameter tungsten anode, and filled with an 80%-20% Ar-CO2 gas mixture.

The resolution was about 1 cm, much smaller than the dimensions of a single tower of the electromagnetic calorimeter, this allows a precise determination of the impact point of photon conversion if it happens in the lead radiator. It turns out approximately 70% of photons convert in PRS. By using PRS' spatial resolution to distinguish two photons and the energy resolution of the ECAL, π^0 can be reconstructed with a resolution found to be 11 MeV/c2. The 2γ invariant mass distribution is shown in Figure 4.4.

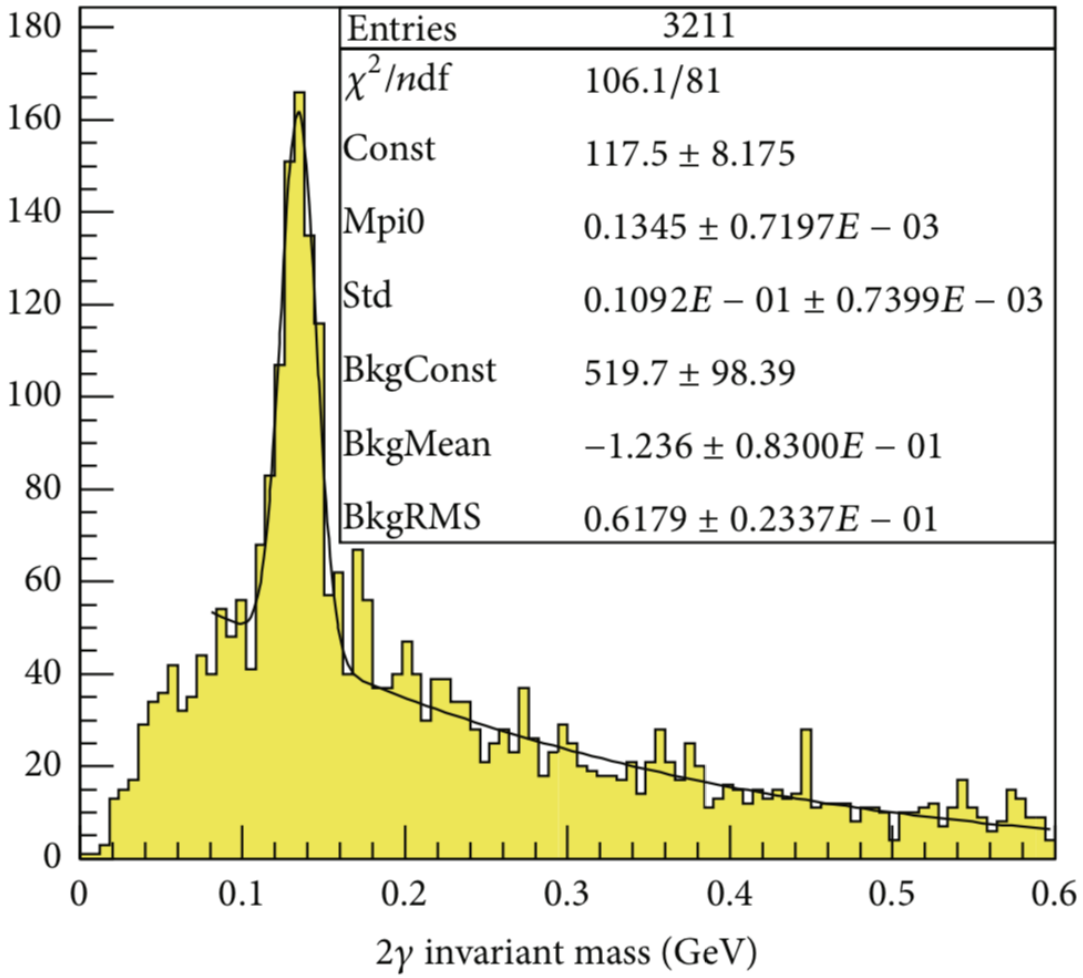

Figure 4.4: 2γ invariant mass distribution which signify the existence of π^0.

For particles energies greater than 4 GeV, by looking at the pulse-height spectrum, the PRS can be used to identify electrons from pions with a 90% efficiency and 10% contamination.

The Electromagnetic Calorimeter (ECAL)

ECAL plays a significant role in identification and measurement of final-state electrons. It is also crucial to measure the neutral component(due to photons) of the transverse momentum of final state particles. To accommodate a good energy resolution over a range from 100MeV to 100GeV, the homogeneous Cherenkov calorimeter is made of 875 lead-glass counters in a matrix of 35 rows×25 columns, each counter

has dimensions 79mm×112mm×494mm. They are calibrated in a test beam of 10 GeV electrons. The spatial resolution of electromagnetic showers is measured to be about 4mm. The energy resolution is measured to be $\Delta E/E = a + b/\sqrt{E}$ with E in GeV, gave a = (1.04 ± 0.01)% and b = (3.22 ±0.07)%.

The Hadronic Calorimeter (HCAL)

The HCAL was installed for the purpose of detecting neutral hadrons and to provide a measurement of the energy of charged hadrons complementary to that derived from momentum measurements in the DC's. It is also important to measure the transverse momentum which the neutral hadrons such as K_L and neutrons could carry a lot. Furthermore, calorimetric measurements of charged particles can be used as consistency check on their momentum measurements in DC, and it also can be used to distinguish between muons and charged hadrons. The HCAL had a energy resolution about $\Delta E/E = 100\%/\sqrt{E(GeV)}$.

The Muon Chambers

In order to provide for the identification of final-state muons,10 drift chambers previously used in the UA1 experiment was installed. Each chamber contains four planes of aluminum drift tubes, with two planes of drift tubes along horizontal and two planes along vertical. Between each two planes, they are staggered by half a tube width in order to resolve left-right ambiguities. The total active area per chamber is $3.75\times5.55\text{m}^2$, the maximum drift length is 7cm.

4.3 Simulation, Reconstruction and detector performance

The neutrino events are generated by the NEGLIB (NOMAD Event Generator LIBrary) which uses LEPTO 6.1 and JETSET 7.4. LEPTO simulate the deep inelastic scattering, JETSET simulate the fragmentation of produced partons into hadrons. NEGLIB also able to simulate quasielatic and resonance events. Later on, coherent

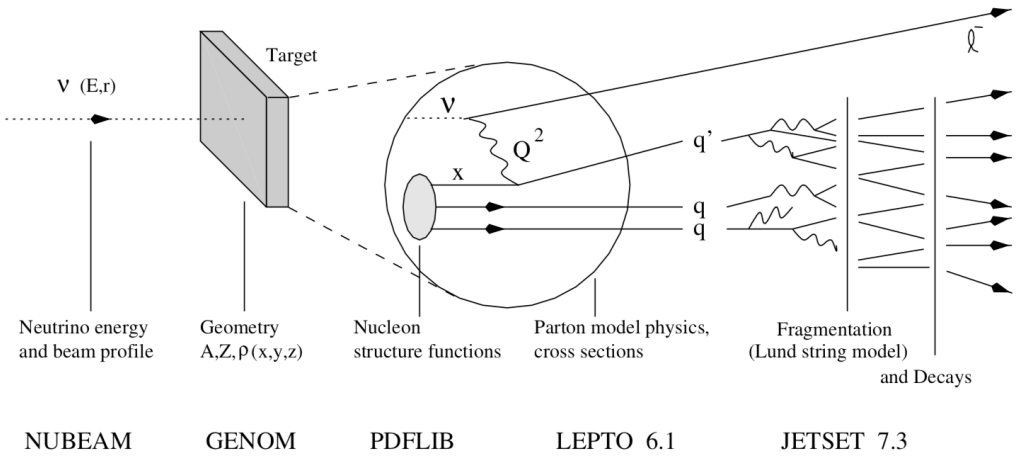

Figure 4.5: The workflow between the several packages within NEGLIB.

model based on Reign Sehgal and Berger Sehgal were added and the coherent events were generated too. As for the vertex of each neutrino interaction, the geometry of NOMAD is used according to the material density distribution along the beam axis. The workflow of the several packages within NEGLIB is shown in Figure 4.5.

After events generation, detector simulation is done by GENOM(GEant NOMad library), which is based on GEANT.

The reconstruction is performed in two stages. The first stage, Phase I, reconstructs raw data from each subdetector with RECON, a general reconstruction package, within phase I, the tracks and vertices in the drift and muon chambers and clusters of hits in the calorimeters are assembled. The second stage, Phase II, identifies each individual particles. The Phase II output is then stored in a DST(Data Summary Tape) format for use.

Not all the events or information is really needed for almost any analyses. The Calisto package is used to apply some initial loose selection upon the DST files and save most commonly used variables in ntuple format.The ntuple format based file can be easily processed by PAW or convert to ROOT from where, one can proceed his intereted study and make plots.

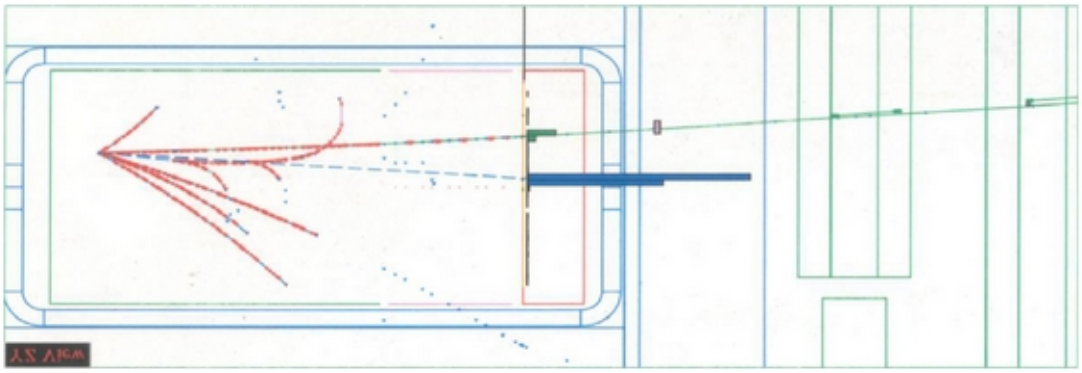

Figure 4.6: Candidate $\nu_\mu CC$ event reconstructed in the NOMAD detector.

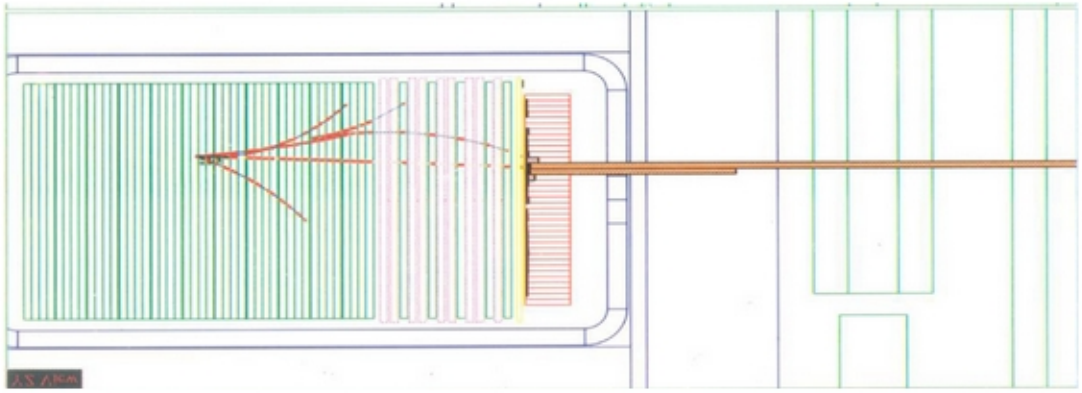

Figure 4.7: Candidate $\nu_e CC$ event reconstructed in the NOMAD detector

Electron Identification

Electron can be identified from other particles when they both pass through TRDs. When charged particle pass through inhomogeneous media, they lose their energy on different ways based on their Lorentz factors ($\gamma = E/mc^2$), particles with γ lose their energy predominantly by ionization, whereas charged particles with $\gamma > 500$ (mainly electrons) also produced transition radiation X-rays at the interfaces of the foils. As a result, a few low energy photons in keV range were produced, about 60% of them were absorbed by the detection plane due to the large cross section between xenon and keV photons. And because the emitted X-ray peaked around the initial particle direction, the x-ray energy deposition was added on top of the ionization losses from

same charged particle. The deposited energy distribution for electrons and pions in TRD straw tubes are shown in figure 4.8.

A likelihood ratio based algorithm using the responses of all the straw tubes was

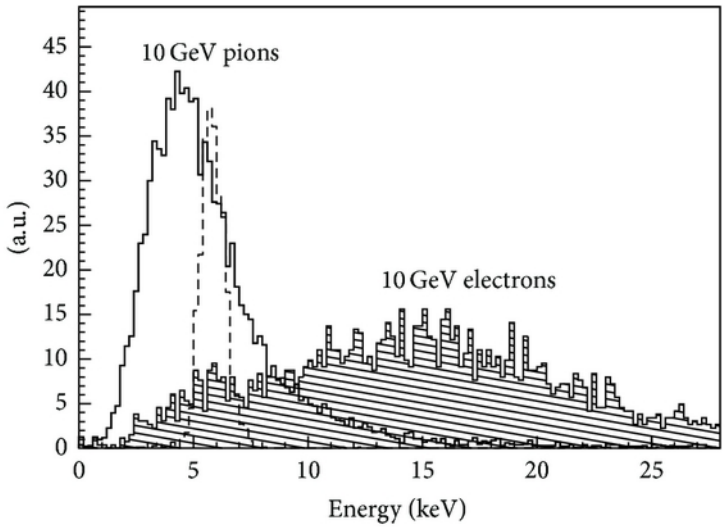

Figure 4.8: Energy deposited in the TRD straw tubes for pions and electrons

developed for electron identification. A pion rejection factor greater than 1000 was obtained with the 9 TRD modules in the momentum range from 1 to 50 GeV/c, while retaining an electron efficiency of 90%.

4.4 τ NEUTRINO SEARCH

The NOMAD experiment was designed to search for τ neutrino appearance from $\nu_\mu \to \nu_\tau$. Even though the oscillation was not observed through the whole operation of the experiment, a brief introduction is deserved here. The ν_τ search is performed by looking for its charged current interaction $\nu_\tau + N \to \tau^- + X$, τ can be identified by its decay products:

$$\tau \to \text{decay products} + \nu_\tau \tag{4.2}$$

Given the lifetime of τ and its energy, the τ travelled 1mm before decaying. However the spatial resolution of NOMAD is not good enough to recognize this

secondary vertex. The decay products would be seen as the primary particles coming from the neutrino vertex. The five primary decay channels are $e^-\bar{\nu}_e\nu_\tau$, $\mu^-\bar{\nu}_\mu\nu_\tau$, $\pi^-\nu_\tau$, $\rho^-\nu_\tau$ and $\pi^-\pi^-\pi^+n\pi^0\nu_\tau$, they sum up to 86% of the total branching ratio.

For the μ channel, ν_μ CC interaction is the main background. Two variables are used to do the selection. On the transverse plan, the angle between hadronic jet direction and muon direction $\phi_{\mu h}$, and the angle between hadronic jet direction and missing momentum ϕ_{mh}. In practice, a two-dimensional search in the combined space of $\phi_{\mu h}$ and ϕ_{mh} can be performed to improve the result.

For the electron channel, after a electron is identified (a DC track associated with primary vertex, satisfy TRD identification algorithm, ECAL cluster shape, consistency between DC momentum measurement and ECAL deposited energy), the main backgrounds are ν_e CC interactions with a genuine primary electron, NC events with an electron from photon conversion or π^0 Dalitz decay. In ν_e CC events the electron was well isolated and balanced the hadron jet momentum in the transverse plane. However, in NC events the electron was embedded in the hadron jet, so it's transverse momentum is almost aligned with the jet. The signal events had intermediate feature between the two extreme cases since neutrinos carried away transverse momentum and the large τ mass introduced a component of the electron momentum perpendicular to the τ direction, thus reducing its isolation. Based on the kinematics, two likelihood ratios λ_e^{NC}, λ_e^{CC} are separated trained to distinguish signal from two separate background source. Then, the plane (λ_e^{NC}, λ_e^{CC}) was considered to select events and optimize the sensitivity of oscillation search.

Unfortunately, the analysis of the full NOMAD data sample gave no evidence for τ appearance. However, it gave a upper limit on $\nu_\mu \to \nu_\tau$ oscillation probability with 90% C.L.[30]:

$$P(\nu_\mu \to \nu_\tau) < 2.2 \times 10^{-4} \tag{4.3}$$

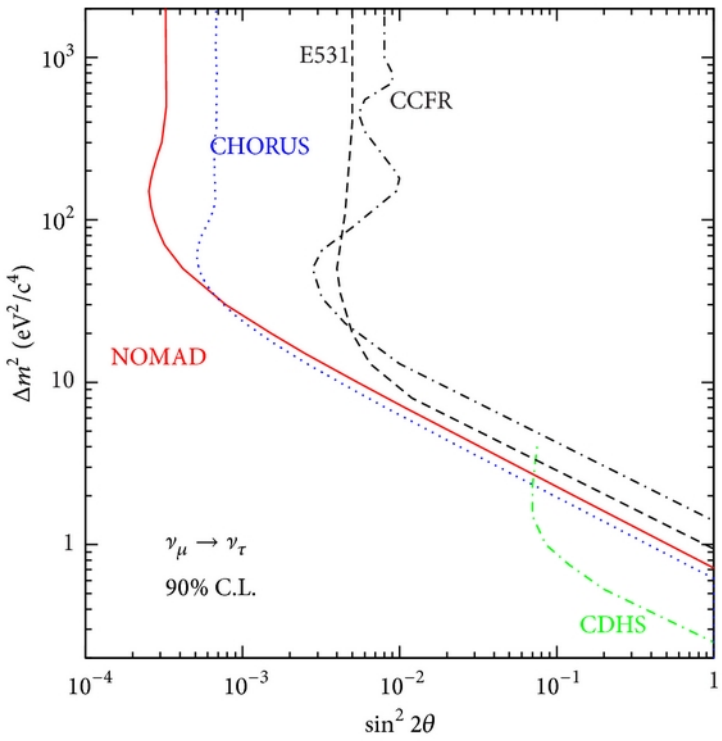

Figure 4.9: Final exclusion plot in the plane $sin^2\theta_{\mu\tau}\Delta$ for two flavor oscillation.[30]

In the two-family oscillation scenario, this sets a 90% CL allowed region in the $sin^2\theta_{\mu\tau}\Delta m^2$ plane which includes $sin^2\theta_{\mu\tau} < 3.3 \times 10^{-4}$ at large Δm^2 and $\Delta m^2 < 0.7eV^2/c^4$ at $sin^2 2\theta_{\mu\tau} = 1$.

4.5 Summary

The NOMAD experiment didn't discover neutrino oscillation. However, it puts limits on $\nu_\mu \rightarrow \nu_\tau$ oscillation probability two orders of magnitude better than previous published results and remains this record until 15 years later.

More importantly, the NOMAD experiment developed excellent detector technologies with high resolution and identification capabilities, which can be learned by future experiments. Indeed, inspired by NOMAD, a straw tube based fine grained

tracker is proposed as one component of DUNE ND complex. This will be talked in detail in Chapter 6.

Chapter 5

Coherent Pion Production in NOMAD

As we mentioned before, for a coherent interaction, there's no exchange of charge or isospin between the neutrino and the nucleus, which doesn't break and recoil very little, this basically tells us the four momentum transfer to the nucleus, especially the square of it, must be very small. Our derivation of coherent pion cross-section in chapter3 starts with low Q^2, this leads to collinearity between the outgoing charged lepton with the neutrino, and because of the low-recoil of nucleus, momentum conservation requires the collinearity of outgoing pion at same time. All these indicate the pion's and lepton's momentum on transverse plane must be small on their own and their combined momentum on transverse plane (missing Pt) is small too. Furthermore, their separate and combined angles with respect to the neutrino direction(beam direction) have to be small too. A event picture is shown in Figure 5.2. It can be tell that both muon and pion tracks are forward-going with little momentum on transverse plane, pion track going upward, muon track going downward which further cancel away the total momentum on transverse plane. It is worth noting that Q^2 is not necessarily zero, therefore the intrinsic transverse momentum for coherent interaction exists and is not negligible.

In reality, the Q^2 of coherent production is never necessarily to be zero, the outgoing lepton's mass is not zero too, and the detector smearing is not negligible when we reconstructing the kinematics, all these will make the above distinguishing variables less significant, but considering the high precision of NOMAD detector, these variables are still appreciable to make a selection.

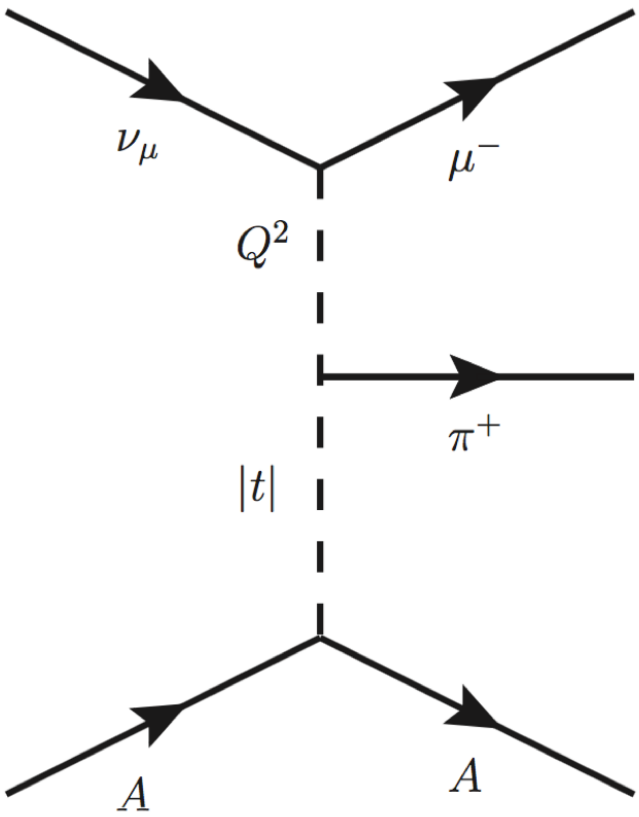

Figure 5.1: Feynman Diagram of coherent π^+ interaction

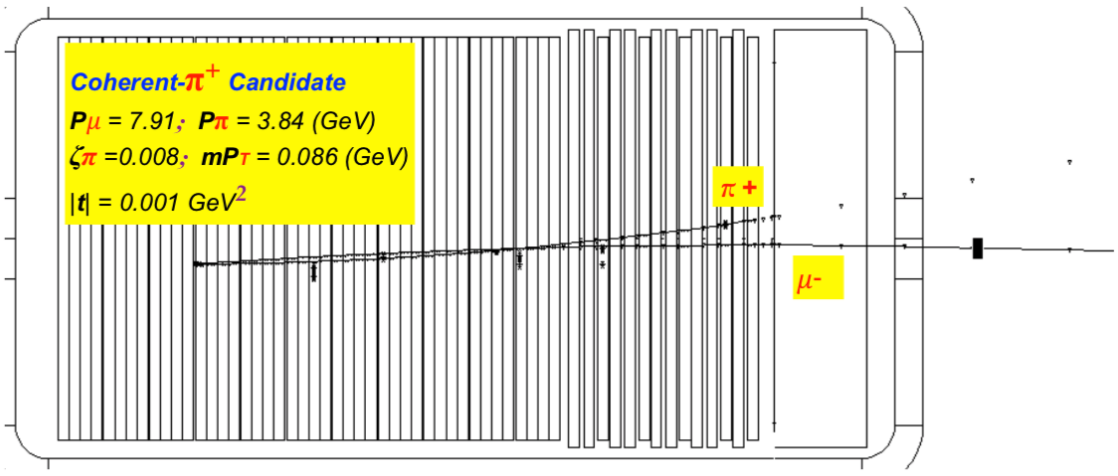

Figure 5.2: A event picture of coherent π^+ candidate

Table 5.1: Normalization factors for each channel

(ν_μ)Channel	Event Number with ratio
CC	$1,436,000$
DIS	$143600/(1+0.055)$
Res	$143600/(1+0.055) \times 0.055/(1+0.75)$
QE	$143600/(1+0.055) \times 0.055/(1+0.75) \times 0.75$
cohπ^+	$143600/(1+0.055) \times 0.055/(1+0.75) \times 0.75 \times 0.26$
cohρ^+	4350

5.1 Normalization

In the era when NOMAD experiment was taking data. High energy physics doesn't have much knowledge about the cross section for each neutrino channel or even the inclusive ensemble, experimentalist cannot completely rely on Monte Carlo softwares to do an absolute normalization or a normalization between different interaction channels. And for the Monte Carlo softwares used for neutrino event generation, it may or may not able to calculate the cross section, and may only take event number requested as input and then simply work on generating the kinematics for each interaction. To take the full advantage of Monte Carlo simulation and ensure it matches data well, applying a normalization upon all the event samples is needed before selection. One also can fine tune the normalization factors according to his/her own specific study and use variables which are particular important to the study. The normalization table is showed in table 5.6.

5.2 Selection

A list of selection cut is explained as following:

1. Fermi Momentum Cut(Pfermi $< 1.0GeV$): Fermi momentum cut is applied to all MC events to remove the non-physical events.

Table 5.2: Fiducial cut of Z minimum for NOMAD data

run No.	$\leqslant$ 8375	[8376,9344]	[9345,14164]	$\geqslant$14165
Zmin(cm)	265.0	115.0	5.0	35.0

2. W2s Cut(W2s $> 1.96GeV^2$): The invariance hadronic mass only applied to DIS and NC events.

3. Fiducial Volume Cut: It's always necessary to apply fiducial cut to cut out the events took place close to detector surface, so the rest of them are equivalently well reconstructed and will have same cut efficiencies for future cuts. The fiducial volume used in this analysis is $-5cm < Z < 405cm$, $|X| < 120cm$, $|Y-5| < 120cm$. For data, the minimum z used varies according to run number, the detail is showed in table 5.2.

4. Muon Identification: During Phase II of reconstruction, a DC track can be matched to a hit in the muon chambers within 40cm in the first station, or within 50cm in the second station. The cut will get passed if one of the three conditions satisfied:

   - Muon probability is greater than 0.999 and track momentum greater than 2.5GeV
   - The track can be matched to muon chamber first or second station with both x, y detected.
   - Is a muon stub

5. Tube/Veto Cut: this cut is applied to remove rock muon or cosmic muons.

6. ncand=2: Number of primary charged track must be exactly 2, This cut will move the QE with only one primary track and Resonance and DIS channel which have more than three tracks.

7. $\mu - \pi+$the selected muon track have negative charge and the other track (call it hadron track) have positive charge: A magnitized detector like NOMAD is able to apply such a cut, this will remove the wrong-sign events.

8. Angle cut: Cut on the angle between lepton track and hadron track. Coherent events are outstanding with the collinearity of both lepton and hadron.

9. Missing Transverse Momentum Cut ($P_m^t < 0.5GeV$), Coherent events have very small missing transverse momentum.

10. Neutral vertex and Cluster Cut: events have neutron hadrons can form secondary vertex which can be identified by decayed charged tracks. π^0 and ρ^0 are the most common ones, and their masses can be reconstructed. If the reconstructed mass is greater than 0.05 GeV, the event fails the cut.

The cut table for all the single cuts is shown in Figure 5.7.

5.3 Multi Dimensional Likelihood

After the last single variable cut, there are still many CCDIS events and $coh\rho^0$ events left. All the backgrounds are more than twice of coherent $\pi+$ events. It has been tested a few more single variable cuts doesn't do a good job, therefore we develop a multi-dimensional likelihood method to maximize the selection. The five variables we found out to be the best candidates are:

- P_{mis}^T Missing transverse momentum has very strong selection power as I mentioned above. The single cut we already applied on this variable is a very gentle cut, and we have not exhausted its power.

- ϕ_{had}^{mis}. Coherent pion events are more well balanced on transverse plane, the angle between the Missing transverse momentum and hadron momentum on the transverse plane is relatively greater for the signal events.

- ζ_π this is defined as : $E_\pi(1-\cos\theta_\pi)$, because of pion's collinearity with neutrino, ζ_π is a very commonly used variable to select coherent events.

- xbj. coherent events typically has a low Xbj since a meson is created when the nucleus stays unmodified.

- $P^t_{\mu\pi}$ this is the double transverse momentum of muon. A double transverse variables is a very powerful tool in selecting events having no nuclear effect such as neutrino hydrogen interaction. Since in coherent events neutrino interact with the whole nucleus coherently, so there's no nuclear effect.

Another variable can be considered is t, which is the squared of four momentum transfer to nucleus. Since both lepton and pion's momentum can be measured, the t can be estimated as following:

$$|t| = |(q - p_\pi)^2| = |(p_\nu - p_\mu - p_\pi)^2| \tag{5.1}$$

$$p_\nu = (E_\nu, 0, 0, E_\nu) = (E_\mu + E_\pi, 0, 0, E_\mu + E_\pi) \tag{5.2}$$

Before we start to do any multi-variate analysis, let's look at a the distribution of the key variables. The 5 variables are shown in Figure 5.3 to Figure 5.8.

Their correlations are shown in figure 5.9. Because of their correlation, simple single cut won't be a good option to do further selection. We'll try to use likelihood ratio to training and testing. Since there are quite a few variables available to be implemented in likelihood ratio, one can group three variables into one set, train them within their three-degree phase space, obtain the likelihood ratio result, then use it as an independent variable and group it with another two variables to train again, the final likelihood ratio will have the highest selection power. The arrangement of variables used in likelihood ratio training is:

$$[P^T_{mis}, \phi_{mis,had}, \zeta_\pi, \quad [xbj, P^T_{\mu,\pi}]] \tag{5.3}$$

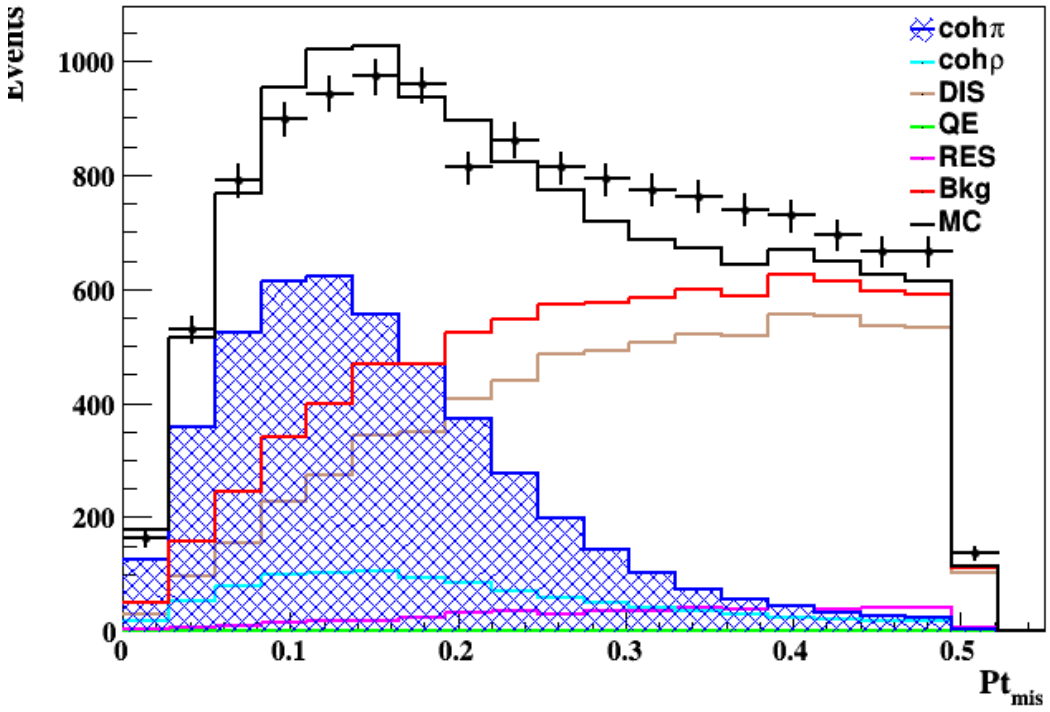

Figure 5.3: Missing transverse momentum distribution before multi-variate analysis.

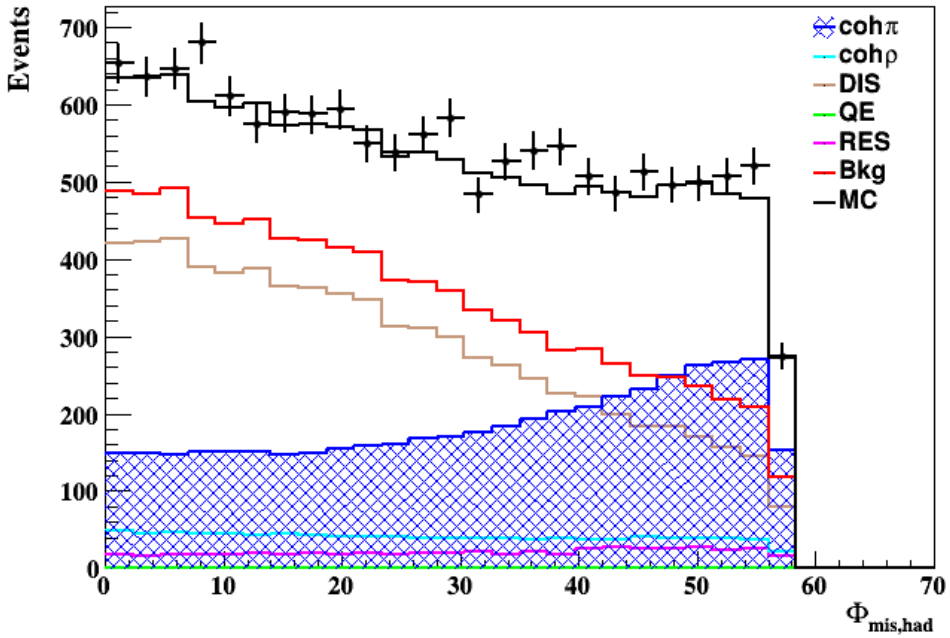

Figure 5.4: ϕ_{had}^{mis} distribution before multi-variate analysis.

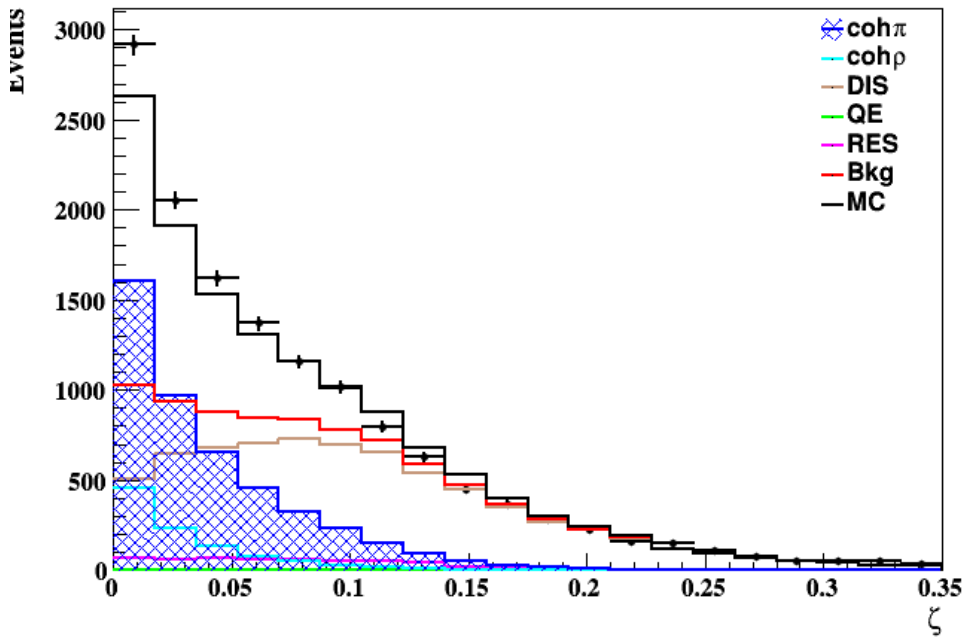

Figure 5.5: ζ_π distribution before multi-variate analysis.

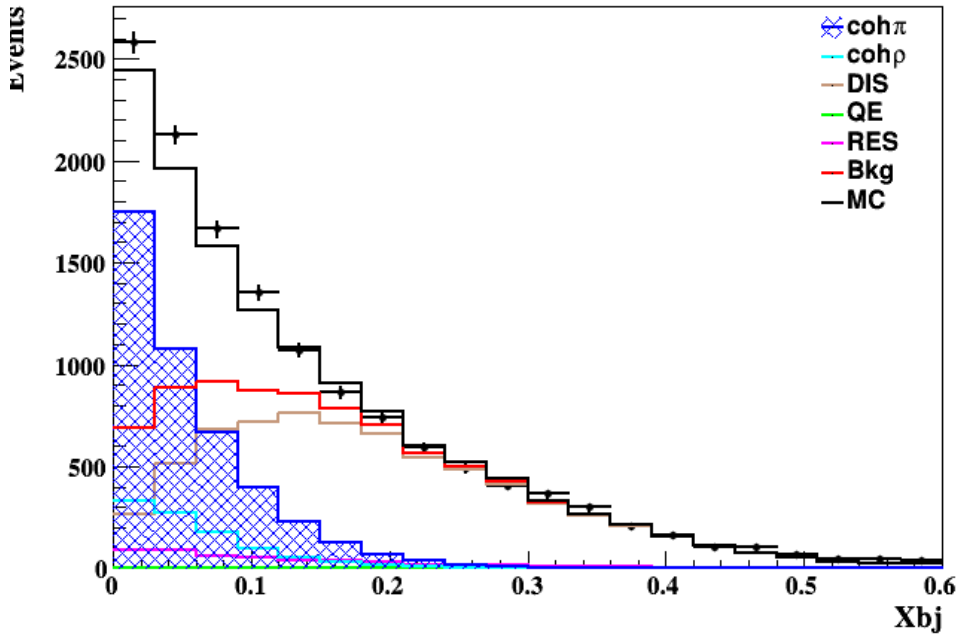

Figure 5.6: Xbj distribution before multi-variate analysis.

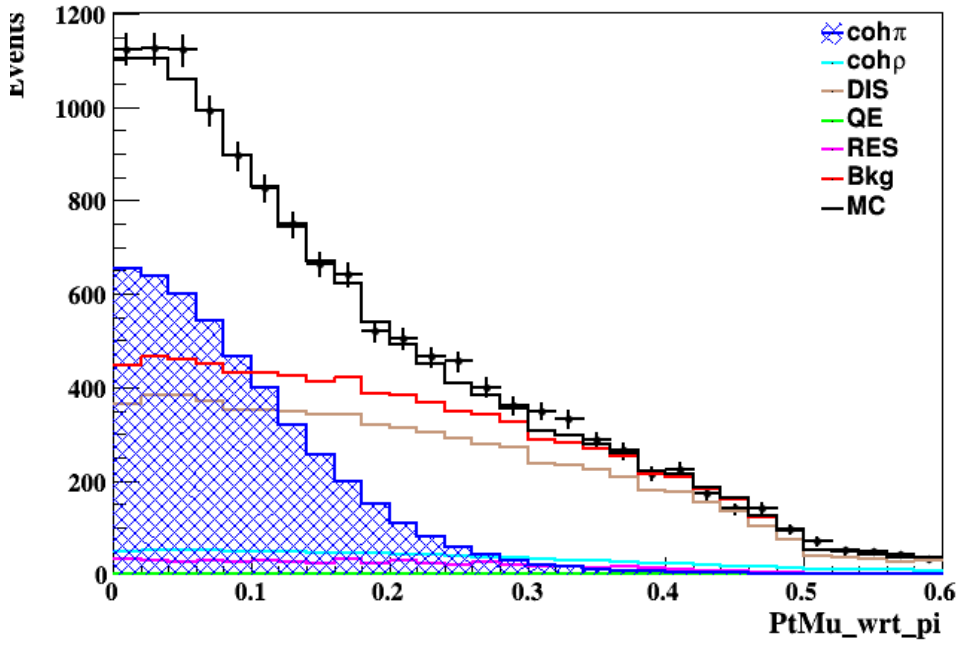

Figure 5.7: $P_{\mu\pi}^{T}$ distribution before multi-variate analysis.

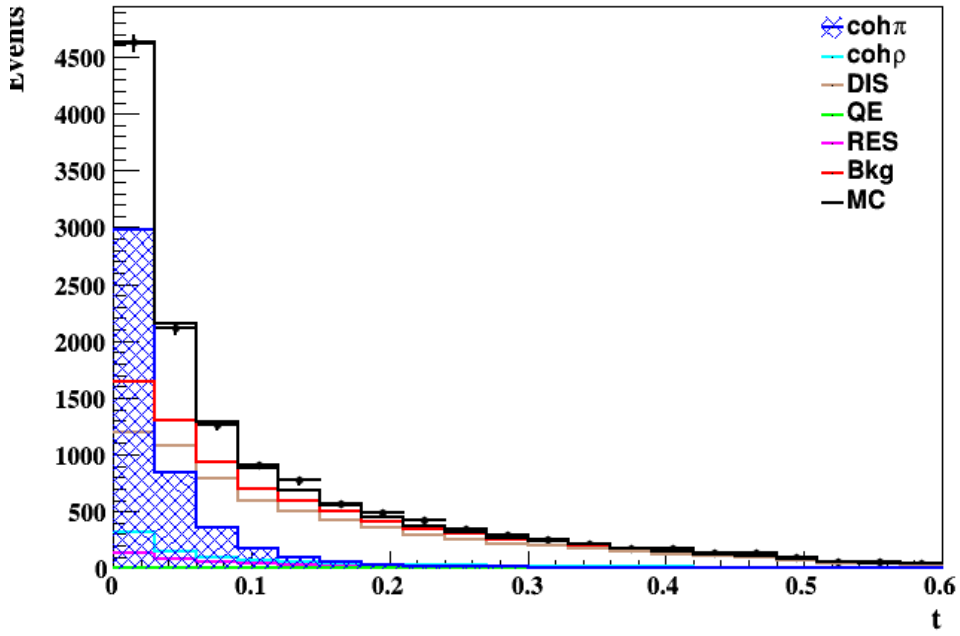

Figure 5.8: t distribution before multi-variate analysis.

After training, the likelihood ratio is applied to whole Monte Carlo sample and data, the result is shown in figure 5.10.

5.4 Neural Network

Artificial Neural Network is a machine learning technique which has already been used in HEP community for a long while, but comparing to the traditional likelihood, it's still a modern tool. Comparing to the bubble chamber era, HEP experiments nowadays require millions or trillions events to be reconstructed on a very sophisticated detector. More complicated algorithms are applied to do reconstruction, more complex variables are saved to the final ntuples, more Monte carlo events are created, at same time physicists pursue more precise result, the traditional one-dimensional cut or multi-dimensional likelihood may not handle the current issue or not give the best result. Machine learning relying on high speed computing provide a totally new perspective for us, it can handle more variables, generally gives better result.

Artificial neural network are layered networks of artificial neurons mimicking biological neurons. The neutrons in each layer don't communicate among themselves, instead, each of them receive signal from previous layer neutrons as input, add weights, and form an output signal and transmit to next layer. The very first layer receive inputs from the user, then it will process the information and transmit to next layer, this procedure continues until last layer, where the output will be the final result. Initially neural network have zero knowledge about how to process the inputs, so the result will simply be random. It has to be "trained" properly to eventually output good result. Now let's use N_{ij} to represent the jth neuron in layer i, the layer i has O_i neurons, the neuron's internal process is simply a non-linear function, for example, a sigmoid function $Out(in) = 1/(1 + e^{-in})$, and the input of neuron N_{ij} is:

$$In(N_{i,j}) = \sum_{r=1}^{O_{i-1}} w_{r,j;i} Out(N_{i-1,r}) \tag{5.4}$$

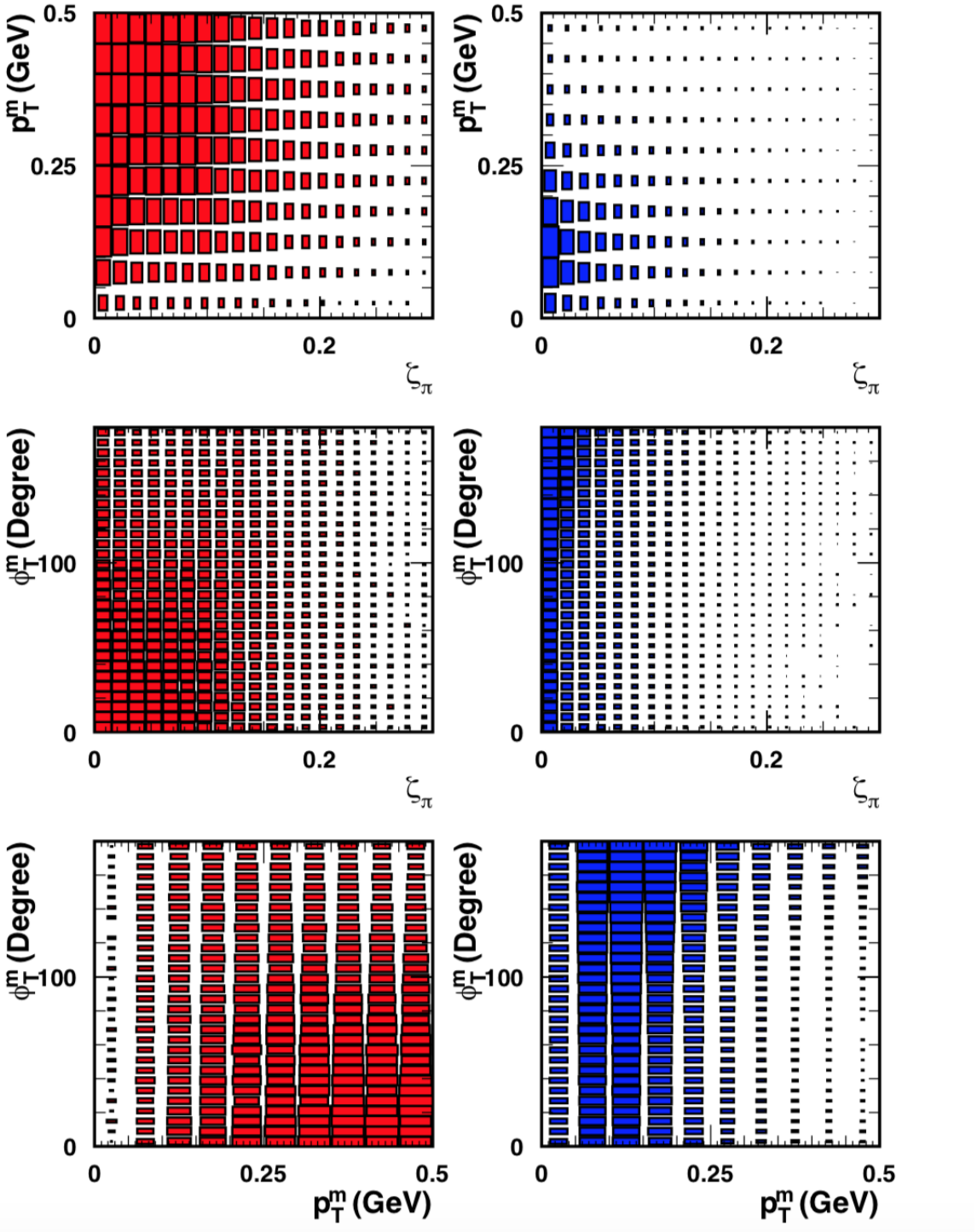

Figure 5.9: Correlations between kinematic variables used to construct likelihood functions for background(left) and signal(right)

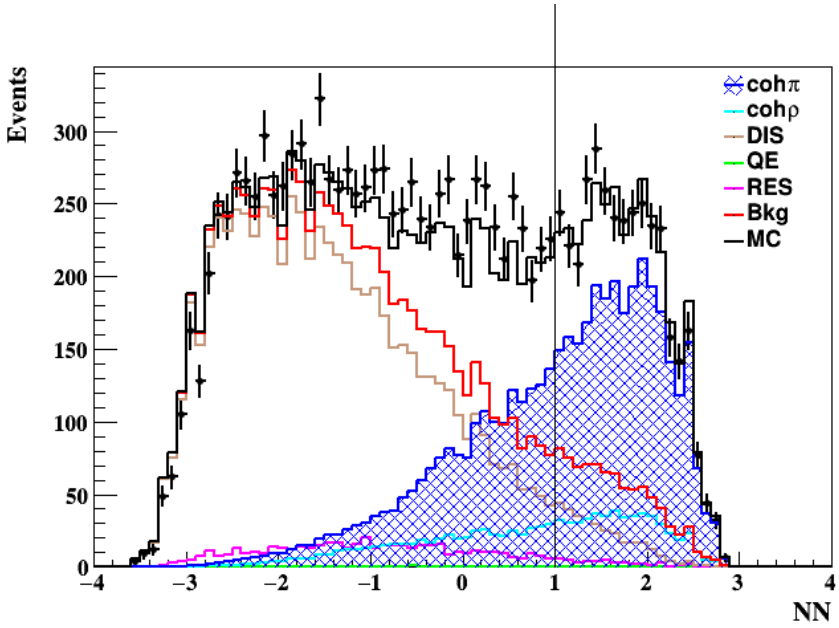

Figure 5.10: The likelihood result

All the neurons in the network can have same and known internal function, so the uniqueness of the network is completely represented by a set of weights $w_{r,j;i}$. The training procedure of the network is essentially to train the network until it achieves a good set of weights, which will enable the network output decent result after taking inputs.

In HEP experiment context, a simplest neural network is feed with a few variables, for examples, the kinematics of a detected neutrino event, the number of input variables is the dimension, it can be as large as user needs, then the output will be a 1 or 0, (signal or background). Before the training, the weights $w_{r,j;i}$ are randomly assigned, the user's input is feed one entry by one entry, directly to the first layer of the network, the first layer neurons process them and transmit the output to next layer, so it's a forward propagation process, after a while the last layer will output a final value and this will be compared with the "true" value, if it predicts well, it will reward the neighbor weighs, or it will punish them. This punish/reward mechanism goes backward, the opposite way how the input information get processed. Ideally,

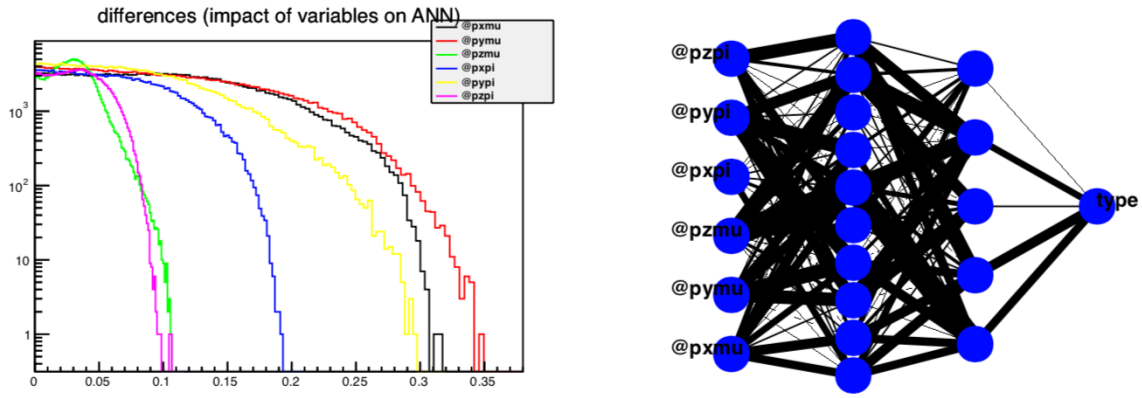

Figure 5.11: Neural Network structure for coherent π^+ selection

user can provide enough input data, so after many rounds of forward and backward work, the weights are trained to the extent that once a new input is given, it still can predict the result well.

When working with likelihood, one generally has to carefully select a few variables which already have strong power to select signal from background, but with neural network, this is not necessary. With enough number of inputs to cover the kinematic space of the neutrino interaction, it is still able to achieve decent result.

This neural network is trained with 6 variables: P^x_μ, P^y_μ, P^z_μ, P^x_{had}, P^y_{had}, P^z_{had}, besides the input layer and output layer, a configuration of 2 intermediate layers with 10 and 5 neurons respectively is used. The structure is shown in Figure 5.11. The training result is shown in Figure 5.12.

5.5 Background Normalization

After the multivariate analysis no matter using likelihood or neural network, a signal region is chosen by a cut on the output variable (LH or NN), this will be the region where we count the number of signal events and start to calculate the cross section by[2]:

$$\sigma = \frac{N_{data} - N_{bkg}}{\epsilon \times N_{target} \times \phi} \tag{5.5}$$

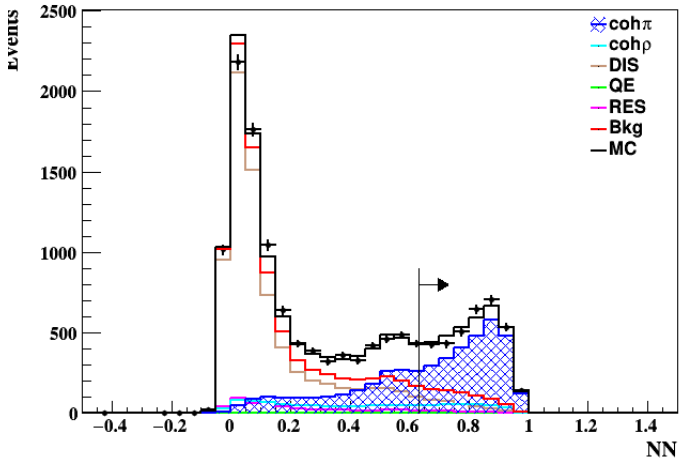

Figure 5.12: Neural Network structure for coherent π^+ selection

The N_{data} is the data in signal region, however, the way we choose the signal region is to maximize the purity of signal and also maximize the efficiency of it. A low-efficiency selection is more susceptible to variations in the signal or background model, a low-purity selection is more susceptible to how background processes are modeled. Therefore, there's a trade-off between maximizing efficiency and purity of a selection. Generally a figure of merit is used to optimize the combination. Back to the equation, since the background cannot be completed reduced to zero after the final cut, we have to deduct it from the data to get a raw-signal, that's why there's a N_{bkg} in the numerator. ϵ is the overall selection efficiency of signal calculated from simulation, N_{target} is the number of nuclei (for neutrino-nucleon interaction, this will be number of nucleon) in the detector fiducial volume, and ϕ is the integrated neutrino flux.

Before we deduct the background, we want to normalize it to make it more consistent with our data. A control region or another term sideband used in collider physics is chosen where background are dominant with little signal contamination, this region can be used to constrain the background and the normalization will be applied to the signal region. A very simple way to do the normalization is to check the number of

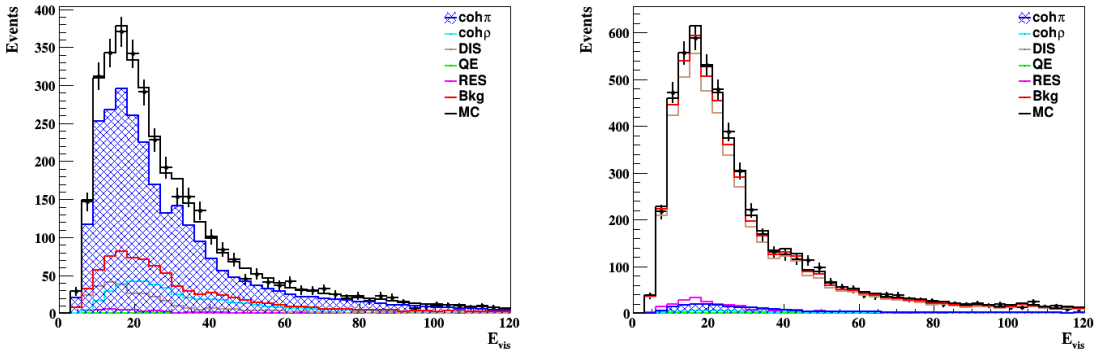

Figure 5.13: E_ν distribution in signal region (left) and control region(right).

signal and background in signal region and control region separately and tune them to be consistent with the number of data. A few iterations are generally needed to maximize the normalization. The detailed equations are shown below:

$$\begin{aligned} SN &= \frac{N^s_{data} - BN \times N^s_{bkg}}{N^s_{sig}} \\ BN &= \frac{N^b_{data} - SN \times N^b_{sig}}{N^b_{bkg}} \end{aligned} \tag{5.6}$$

Where the N^s_{data} and N^b_{data} are the number of data in signal region and control region(background region) separately. N^s_{sig} and N^b_{sig} are the number of MC signal events in signal region and control region separately. N^s_{bkg} and N^b_{bkg} are the number of MC background events in signal region and control region separately.

This can be done in whole phase space or in a few separate regions, in my analysis, both methods are conducted. For the latter, visible neutrino energy is used to split to 7/14/24 regions, within each region, the background normalization is independently conducted.

5.6 Unfolding

Unfolding (or deconvolution) is a general term for removing the effect of a measuring device from a measurement. So far we have been using reconstructed variables to do the selection, the reconstructed value is the truth value smeared by our detector

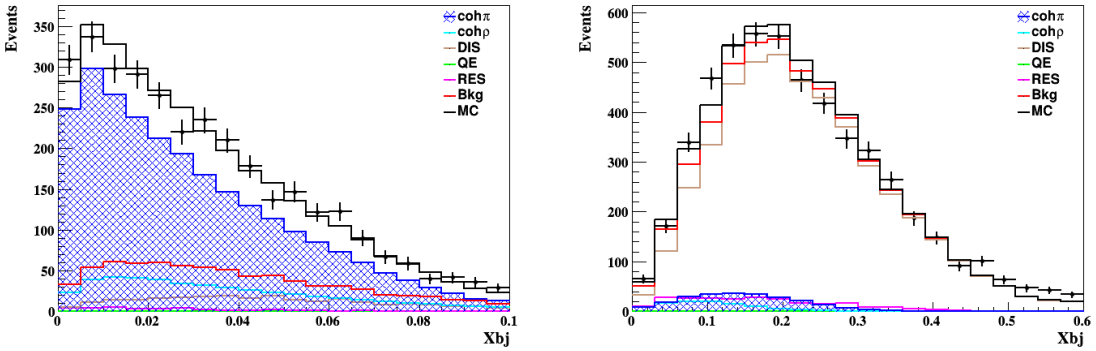

Figure 5.14: Xbj distribution in signal region (left) and control region(right).

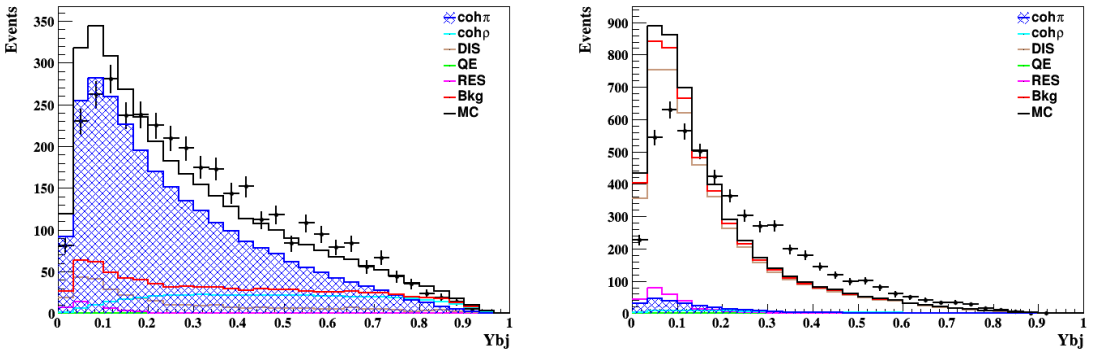

Figure 5.15: Ybj distribution in signal region (left) and control region(right).

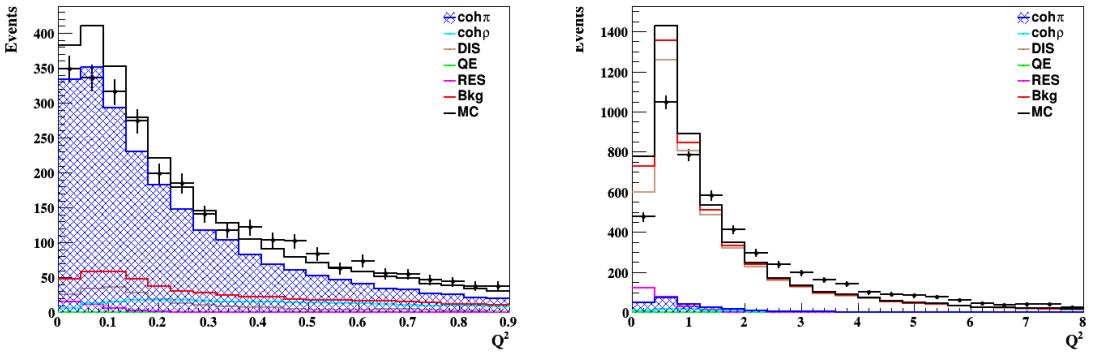

Figure 5.16: Q^2 distribution in signal region (left) and control region(right).

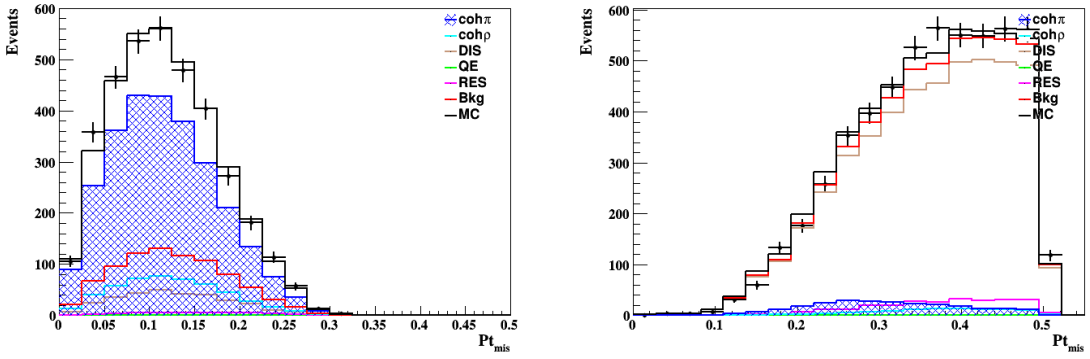

Figure 5.17: Missing transverse momentum distribution in signal region (left) and control region(right).

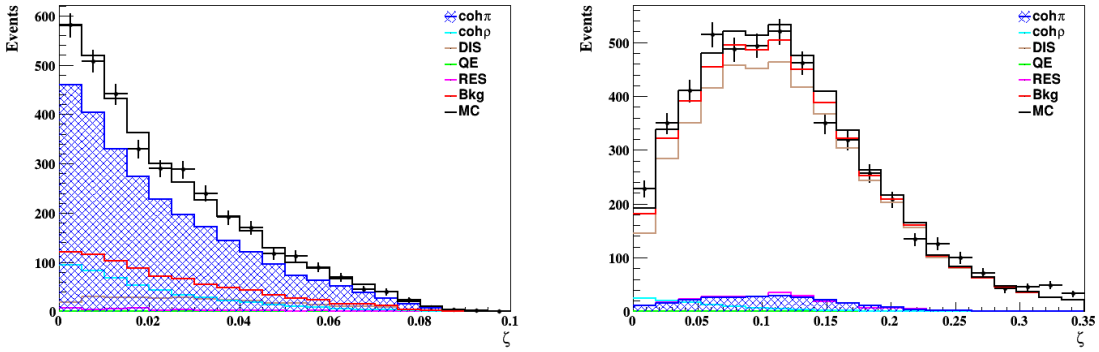

Figure 5.18: ζ distribution in signal region (left) and control region(right).

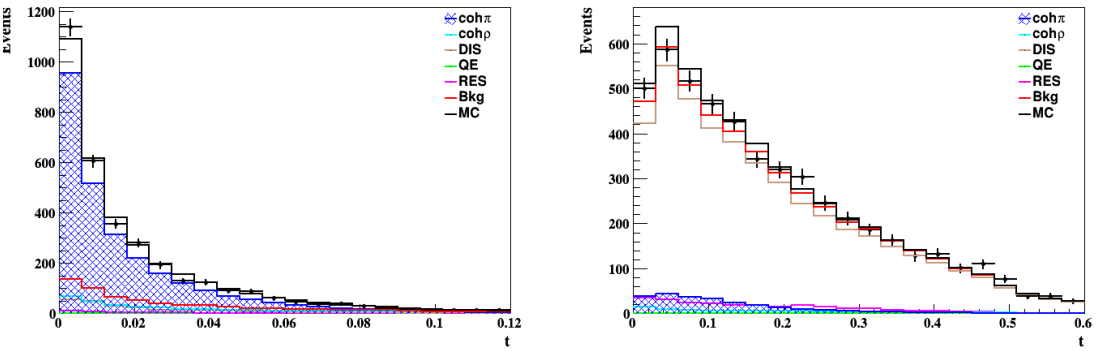

Figure 5.19: t distribution in signal region (left) and control region(right).

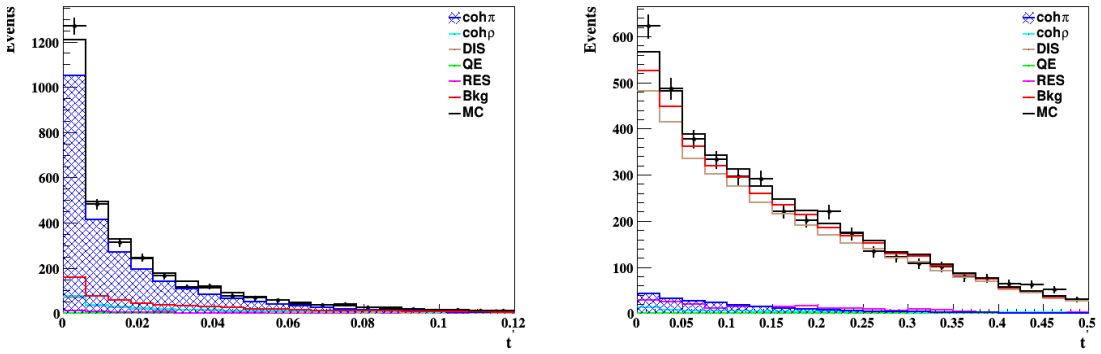

Figure 5.20: t' distribution in signal region (left) and control region(right).

NOMAD, what we really interested are the true value, only with this, we can compare it with results from other experiment. And unfolding is exactly what we are trying to do. The simplest way to do unfolding is to create an unfolding matrix, a matrix with row/column represent true value, column/row represent reconstructed value, by using reconstructed Monte Carlo, the matrix can be filled. If the detector is perfect and 100% reconstructs the truth out. Then the unfolding matrix is simply all ones along the diagonal, zeros off-diagonal and unfolding is not necessary. But in real experiment, reconstruction is hardly close to truth, and unfolding is generally necessary. After unfolding, the fully corrected number of Coh π^+ is:

$$\begin{aligned} &7762.2 \pm 171.4(Stat.) \pm 48.3(BN) \pm 326.7(Syst.) \\ &= 7762.2 \pm 372.1(Stat. \oplus Syst.)(\pm 4.8\%) \end{aligned} \tag{5.7}$$

5.7 Ratio to ν_μ inclusive CC events

ν_μ inclusive CC[27] has been studied and well-measured in NOMAD, the result can be directly used to calculate the cross section of other channels. Therefore, instead of using the cross-section equation above to calculate the coherent π^+, we find out the ratio of number of coherent π^+ events to number of ν_μ inclusive CC events, and multiply it with the average mass number of detector fiducial area 12.8, it will give

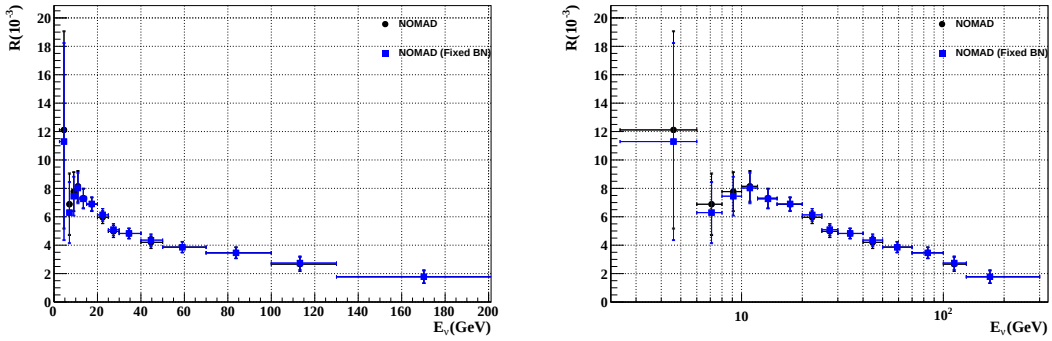

Figure 5.21: the ratio of coherent π^+ cross section to the cross section of inclusive CC

the ratio of coherent π^+ cross section to the cross section of inclusive CC . The ratio is shown in Figure 5.21 and Table 5.8.

5.8 Cross Section

After obtaining the ratio of coherent π^+ cross section to the cross section of inclusive CC, then it's straightforward to calculate coherent π^+ cross section by using inclusive CC result [27]. The cross-section result in 14 E_ν bins is shown in Figure 5.23 and in Table 5.8.

The final cross section we obtained by using non-fixed background normalization in 14 neutrino energy bins is: $\sigma = 117.827 \pm 2.7(\text{stat.}) \pm 4.96(\text{syst.}) \times 10^{-40} cm^2/\text{nucleus}$ at the average neutrino energy of 25GeV, at average atomic number A=12.8.

5.9 systematics

There are a couple of systematic uncertainties I will talk about.

- Selection efficiency. For each cut we applied, we cut it on reconstructed value since we don't know the true value, it will more or less affect the efficiency which is the denominator of the cross-section equation. Generally the better resolution we have for the cut variable, we suffer less uncertainty of efficiency from it, the

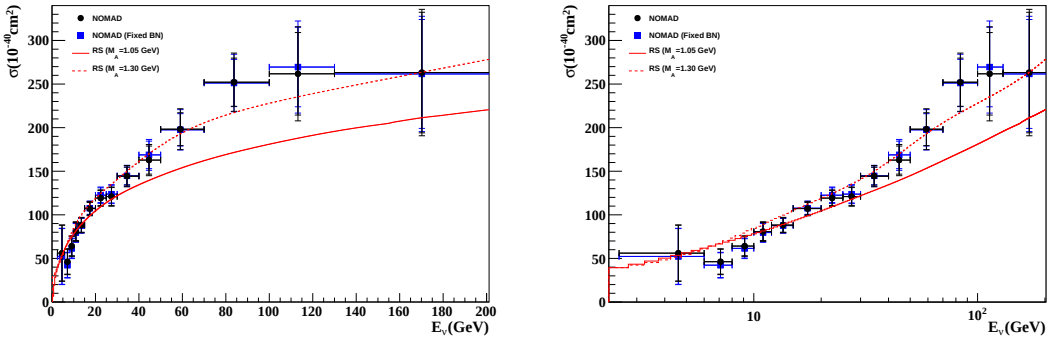

Figure 5.22: Cross section of coherent π^+ as a function of neutrino energy, in comparison with RS model. Left: neutrino energy in linear scale, Right: neutrino energy in logarithmic scale.

Table 5.3: Systematic Uncertainties for each selection cut in 14 E_ν bins.

E (GeV)	$E_\pi - \sigma$	$E_\pi + \sigma$	$\theta_{\mu\pi} - \sigma$	$\theta_{\mu\pi} + \sigma$	$P_t^M - \sigma$	$P_t^M + \sigma$
2.5 $\sim$ 6.0	11.68	14.92	0	1.22	-0.69	1.69
6.0 $\sim$ 8.0	-8.79	-13.24	0.19	-2.21	-3.2	-0.2
8.0 $\sim$ 10.0	2.98	-0.39	0.66	-0.29	1.35	0.04
10.0 $\sim$ 12.0	2.39	-3.4	-0.04	0.67	-1.55	-0.19
12.0 $\sim$ 15.0	0.17	-1.25	2.18	1.79	0.71	1.42
15.0 $\sim$ 20.0	1.02	0.74	0.47	-0.3	-0.12	0.04
20.0 $\sim$ 25.0	-0.59	1.84	1.15	0.13	0.99	0.45
25.0 $\sim$ 30.0	1.01	-0.38	0.38	0.94	0.98	-0.17
30.0 $\sim$ 40.0	0.86	-1.25	0.48	-1.25	0.15	-0.4
40.0 $\sim$ 50.0	-0.11	-1.19	0.9	-1.56	-0.52	0.82
50.0 $\sim$ 70.0	0.59	1.48	0.64	-0.47	-0.75	-0.12
70.0 $\sim$ 100.0	-0.01	-1.62	1.91	-0.37	3.04	-1.6
100.0 $\sim$ 130.0	3.11	-1.1	-0.43	-1.7	-0.27	-0.06
130.0 $\sim$ 300.0	-0.5	-3.86	-0.97	6.62	-0.87	-1.79
2.5 $\sim$ 300.0	0.64	-0.6	0.75	-0.02	0.21	0.09

uncertainty for each cut variable is showed in Figure 5.3. For each cut, we vary it by minus then plus one sigma (from resolution),find out the corrected signal , then compare it with the nominal one, the percentage difference will be assigned as the uncertainty.

- Backgrond normalization error. As I mentioned above, there are two ways have been used to do background normalization, one is to split "visible neutrino

Table 5.4: Systematic Uncertainties for background cross section modeling in 14 E_ν bins.

E (GeV)	Res$-\sigma$	Res$+\sigma$	Coh$\rho-\sigma$	Coh$\rho+\sigma$	LH$-\sigma$	LH$+\sigma$
2.5 $\sim$ 6.0	7.39	-1.57	1.42	-1.03	7.97	-2.08
6.0 $\sim$ 8.0	-4.78	-2.98	-5.82	1.27	-6.53	-3.02
8.0 $\sim$ 10.0	0.6	-1.4	1.35	1.67	-0.24	-1.72
10.0 $\sim$ 12.0	-2.5	0.83	-1.43	-0.18	-2.73	1.08
12.0 $\sim$ 15.0	0.96	1.11	-0.66	1.03	0.86	1.55
15.0 $\sim$ 20.0	-0.93	-0.52	-1.76	0.62	-0.88	-0.88
20.0 $\sim$ 25.0	0.43	2.49	-1.5	2.67	0.52	2.36
25.0 $\sim$ 30.0	2.28	1.25	-0.53	3.94	1.57	1.58
30.0 $\sim$ 40.0	-0.02	-1.9	-2.32	1.25	-0.27	-2.11
40.0 $\sim$ 50.0	1.76	2.74	-3.13	3.45	1.85	2.25
50.0 $\sim$ 70.0	-2.99	-0.01	-2.43	2.32	-2.78	-0.98
70.0 $\sim$ 100.0	-6.4	2.61	-2.75	0.71	-6.27	2.64
100.0 $\sim$ 130.0	-2.23	-5.36	-6.42	1.75	-2.08	-3.82
130.0 $\sim$ 300.0	2.49	9.43	-1.14	8.1	2.52	6.43
2.5 $\sim$ 300.0	-0.38	0.47	-1.7	1.68	-0.52	0.33

energy" to few bins and do background normalization separately, the other is to do it in whole range. The difference between the two is considered as a systematic uncertainty.

- Cross section error. A big systematic uncertainty comes from the cross section prediction for each background channel. We find out the error the same way we do for selection efficiency. The 1 sigma error used for CC Resonance is 7%, from NOMAD measurement [16], the 1 sigma error for CC coherent ρ^+ is 8%[22], from another NOMAD measurement. Comparing to these two channels, the uncertainty coming from quasi-elastic is negligible. for DIS, we already used control region to restrain it. Its error is contained in the background normalization error. The systematic uncertainties for each channel's cross section modeling is shown in Figure 5.4.

- Systematics from Final State Interaction(FSI). For coherent processes, it's not sensitive to final state interaction since neutrino interact with whole nucleus

Table 5.5: Systematic Uncertainties for Flux, FSI and the summary of total systematic errors, statistical errors and total errors in 14 E_ν bins.

E (GeV)	Flux Err	FSI	Stat	Tot Sys.	Tot Err (%)
2.5 ∼ 6.0	3.3	4.51	34.66	22.87	41.53
6.0 ∼ 8.0	3.5	4.51	15.86	20.48	25.90
8.0 ∼ 10.0	3.7	4.5	10.83	7.43	13.14
10.0 ∼ 12.0	2.6	4.68	8.92	8.15	12.09
12.0 ∼ 15.0	2.6	4	6.87	6.45	9.43
15.0 ∼ 20.0	2.3	4.53	5.16	5.82	7.78
20.0 ∼ 25.0	2.3	2.45	5.76	6.26	8.50
25.0 ∼ 30.0	2.3	2.4	6.93	6.46	9.48
30.0 ∼ 40.0	3.2	1.75	5.78	5.71	8.13
40.0 ∼ 50.0	3.2	1.64	8.26	7.70	11.30
50.0 ∼ 70.0	5.9	0.71	8.24	8.24	11.66
70.0 ∼ 100.0	5.9	-2.83	9.59	12.77	15.97
100.0 ∼ 130.0	7.5	-3.5	16.13	13.40	20.97
130.0 ∼ 300.0	7.5	8.5	21.45	20.05	29.37
2.5 ∼ 300.0	2.5	1.8	2.16	4.16	4.69

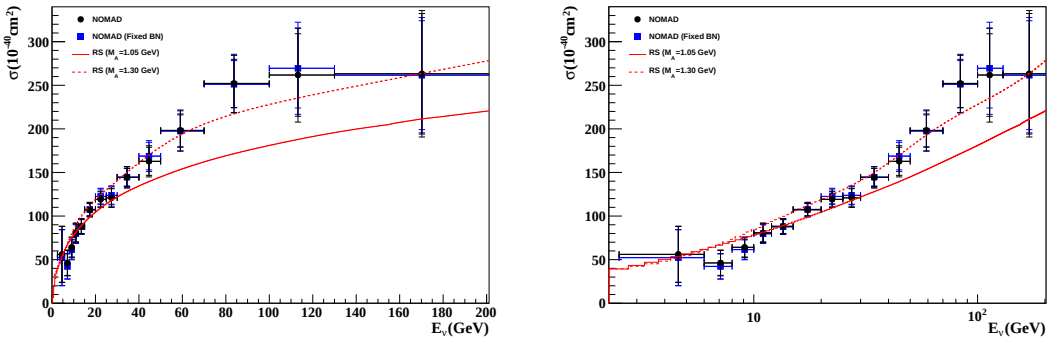

Figure 5.23: coherent π^+ cross section as a function of E_ν, comparing with RS model, Left: E_ν is in linear scale, Right: E_ν is in log scale.

and pion is generated out of this effect. However, FSI affect any neutrino-nucleon background processes. So by switching FSI on and off in Monte Carlo, we generate separate MC datasets and compare the result, we are able to find out the size of the uncertainty. The uncertainty is shown in Figure 5.4.

- Flux uncertainty. This is shown in the table 5.5.

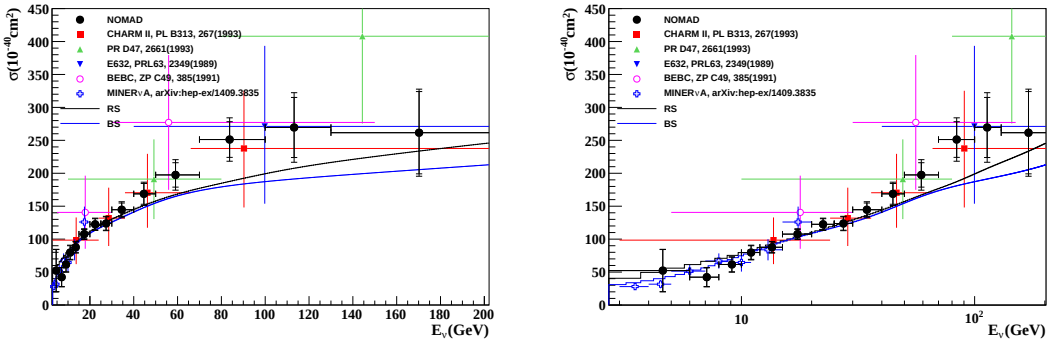

Figure 5.24: coherent π^+ cross section as a function of E_ν, comparing with RS model, Left: E_ν is in linear scale, Right: E_ν is in log scale

By combining all the systematic uncertainties from different sources, we can find out the total systematic uncertainty, it's shown in Figure 5.5 together with statistical uncertainty and total uncertainty.

5.10 Comparison with World Data

The comparison between this analysis with the historical measurement from other experiments is shown in Figure 5.24 together with Rein-Sehgal model and Berger-Sehgal model. The data are from experiments E632[35, 36], BEBC[37], Charm II[34], MINVERνA[9]. All the experiments measurements are scaled to have equivalent atomic number A=12.8 by $(A/12.8)^{1/3}$ for the purpose of comparison. The cross section measurement of this NOMAD analysis is consistent with the cross-section prediction of Rein-Sehgal Model. So far, even though NOMAD data was taken more than two decades ago, this analysis still provides the largest coherent pion interaction statistics and most precise measurement of cross section with average E_ν =25 GeV.

It is worth nothing that the counterpart of this analysis: coherent π^- analysis with NOMAD data, has already been conducted, interested reader can find it here[17].

Table 5.6: Cut table for normalization (neglibDIS).

Cut	QE	Res	CC-DIS	Cohrho+	Cohpi+	MC	data	data/MC
Total	35480.3	47316.8	1561739.4	4691.9	11416.5	1660644.9	4018980	2.42
Pfermi	35257.3	47031.2	1547988.8	4691.9	11416.5	1646385.7	4018980	2.44
W2	35257.3	47031.2	1472166.6	4691.9	11416.5	1570563.5	4018980	2.56
Fidu	32084.0	42778.6	1361137.4	4350.0	10330.1	1450680.2	3135328	2.16
Epi	32084.0	42778.6	1361137.4	4350.0	8341.8	1448691.8	1926258	1.33

Table 5.7: Cut Table for all single cuts(neglibDIS)

Cuts	QE	Res	CC-DIS	Cohrho+	Cohpi+	MC	Data	Data/MC
Total	21166.0	28377.3	956794.5	4214.1	10003.0	1020554.8	4018980	3.94
pfermi	21047.8	28213.4	948625.6	4214.1	10003.0	1012103.9	4018980	3.97
w2	21047.8	28213.4	902910.4	4214.1	10003.0	966388.7	4018980	4.16
fidu	19381.9	25925.4	835571.0	3908.7	9211.0	893997.9	3135328	3.51
ph2mu	19101.6	25564.2	735207.1	3577.8	9075.0	792525.6	1240972	1.57
tube/veto	18930.4	25176.9	730634.8	3519.8	9008.9	787270.7	1175872	1.49
ncand=2	7681.5	13293.9	71994.6	2692.9	8228.3	103891.2	141752	1.36
mu-	7680.9	13291.0	71819.5	2665.1	8204.9	103661.4	132297	1.28
had+	7466.4	12989.6	68296.8	2638.5	8149.0	99540.3	123453	1.24
theta<177.5	7462.4	12985.0	68285.4	2638.2	8147.2	99518.2	121038	1.22
Fit Matrix Error	7372.6	12892.9	67658.4	2601.6	8076.6	98602.1	119277	1.21
Epi>1.0 GeV	3186.4	3975.1	41141.1	2405.1	5376.9	56084.6	66282	1.18
Theta<0.5 Rad	10.7	1174.2	25484.3	2397.3	5180.7	34247.2	41118	1.20
mPt<0.5 GeV	7.4	554.2	9978.4	2146.5	5006.4	17692.8	18619	1.05
asym_phadpneu>0.	7.4	550.9	7793.9	1211.5	4994.8	14558.5	14421	0.99
mgg<0.05	7.4	550.7	7514.0	997.5	4971.2	14040.8	13709	0.98

Table 5.8: R and cross-section for coherent $\pi+$ selection, 14 E_{vis} bins are used, with non-fixed BN(background normalization), NN is used for multivariate analysis

Evis	$\overline{E}$	Norm-bkg	Data	Raw-sig	Eff	Corr-sig ± Stat	R	R-Err	Xsec ± Stat
2.5 ∼ 6.0	4.6	8.4	24	15.6	0.1628	90 ± 31.18	6.77	2.345	31.31 ± 10.853
6.0 ∼ 8.0	7.1	21.8	81	59.2	0.2675	218 ± 34.58	8.26	1.31	55.45 ± 8.797
8.0 ∼ 10.0	9.1	31.7	142	110.3	0.3029	370.9 ± 40.18	8.15	0.882	67.27 ± 7.286
10.0 ∼ 12.0	11	44.8	213	168.2	0.3262	513 ± 45.78	8.53	0.762	84.72 ± 7.561
12.0 ∼ 15.0	13.5	68.7	340	271.3	0.3464	792.4 ± 54.45	7.5	0.515	90.6 ± 6.226
15.0 ∼ 20.0	17.4	109.8	590	480.2	0.3727	1294.2 ± 66.82	7.19	0.371	112.06 ± 5.785
20.0 ∼ 25.0	22.4	92.7	495	402.3	0.3984	998.9 ± 57.51	6.35	0.365	126.8 ± 7.301
25.0 ∼ 30.0	27.4	76.1	340	263.9	0.4095	672.5 ± 46.62	5.32	0.369	129.46 ± 8.975
30.0 ∼ 40.0	34.5	82.9	487	404.1	0.432	916.7 ± 53.01	5.39	0.312	161.47 ± 9.338
40.0 ∼ 50.0	44.6	59.1	264	204.9	0.4272	481.7 ± 39.8	4.37	0.361	169.15 ± 13.977
50.0 ∼ 70.0	59.1	62.1	278	215.9	0.4145	513.9 ± 42.34	3.69	0.304	188.96 ± 15.57
70.0 ∼ 100.0	83.8	48.2	207	158.8	0.3843	412.1 ± 39.52	2.93	0.281	212.79 ± 20.406
100.0 ∼ 130.0	113.2	33	102	69	0.3775	182.9 ± 29.5	2.29	0.37	225.25 ± 36.335
130.0 ∼ 300.0	170.2	25.7	72	46.3	0.3362	135.6 ± 29.1	1.57	0.337	232.1 ± 49.791
2.5 ∼ 300.0	25	752.5	3635	2882.5	0.3736	7715.6 ± 166.48	5.35	0.116	119.91 ± 2.587

Chapter 6

Coherent π application in proposed Straw Tube Tracker Based SAND Detector in DUNE

6.1 The Near Detector of DUNE

Similar to any other near detectors of long baseline experiments, the near detector of DUNE serves two purposes[3, 1]. (1) Constraining the systematic uncertainties related to the oscillation measurements. (2) Advancing short-baseline neutrino physics such as precision measurements of neutrino interactions. The design of near detector is still being actively discussed and developed. The current reference configuration of Near detector complex include three components: a large mass Liquid Argon Time projection Chamber (LArTPC) without magnetic field, a magnetized Multi- Purpose Detector (MPD), both of them plan to be moveable according to DUNE PRISM program. A third detector, System for on-Axis Neutrino Detection (SAND) will be located on-axis to do beam monitoring and perform various physics measurements. The Near Detector complex structure is illustrated at figure 6.1 This chapter will focus on introducing the SAND and the coherent pion channel's application within it.

The ND complex will be placed 62m underground, at a distance of 574 m from target. A schematic view of the neutrino beam line and near detector location is shown in Figure 6.2.

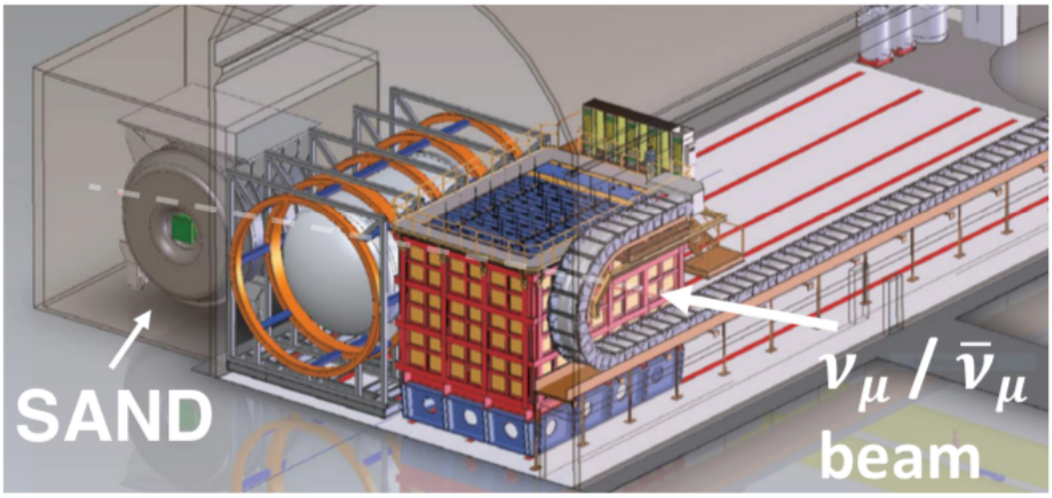

Figure 6.1: DUNE Near Detector Complex

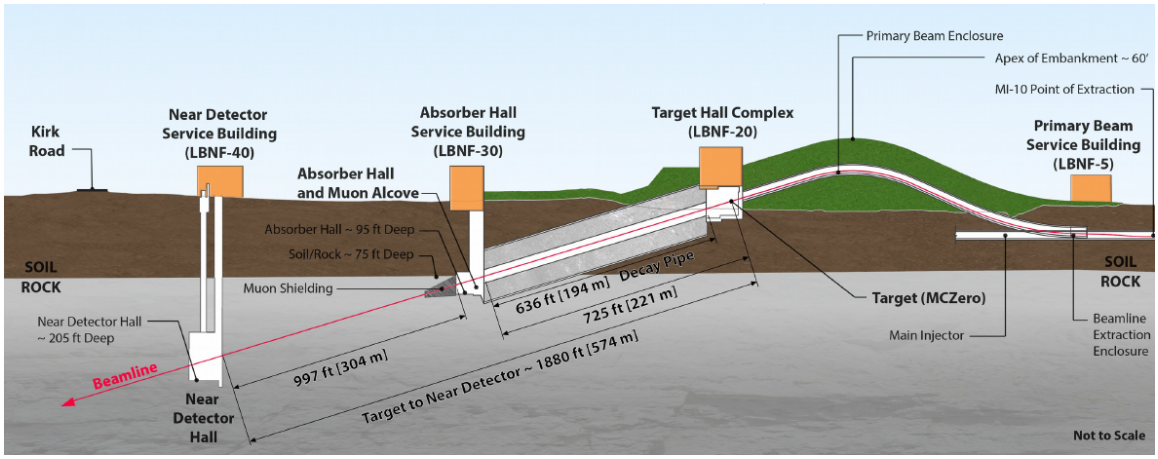

Figure 6.2: The DUNE neutrino beam line

6.2 SAND

The System for on-Axis Neutrino Detection (SAND) utilize the existing KLOE[29] magnet and electromagnetic calorimeter, a low-density tracking device will be placed in the center. The old KLOE detector is shown in figure reffig:kloe_pic The proposed design is a straw tube technology based tracker (STT), a liquid argon volume can be added to do cross-calibration between different ND components and unravel nuclear effects. The proposed geometry is show in figure 6.4.

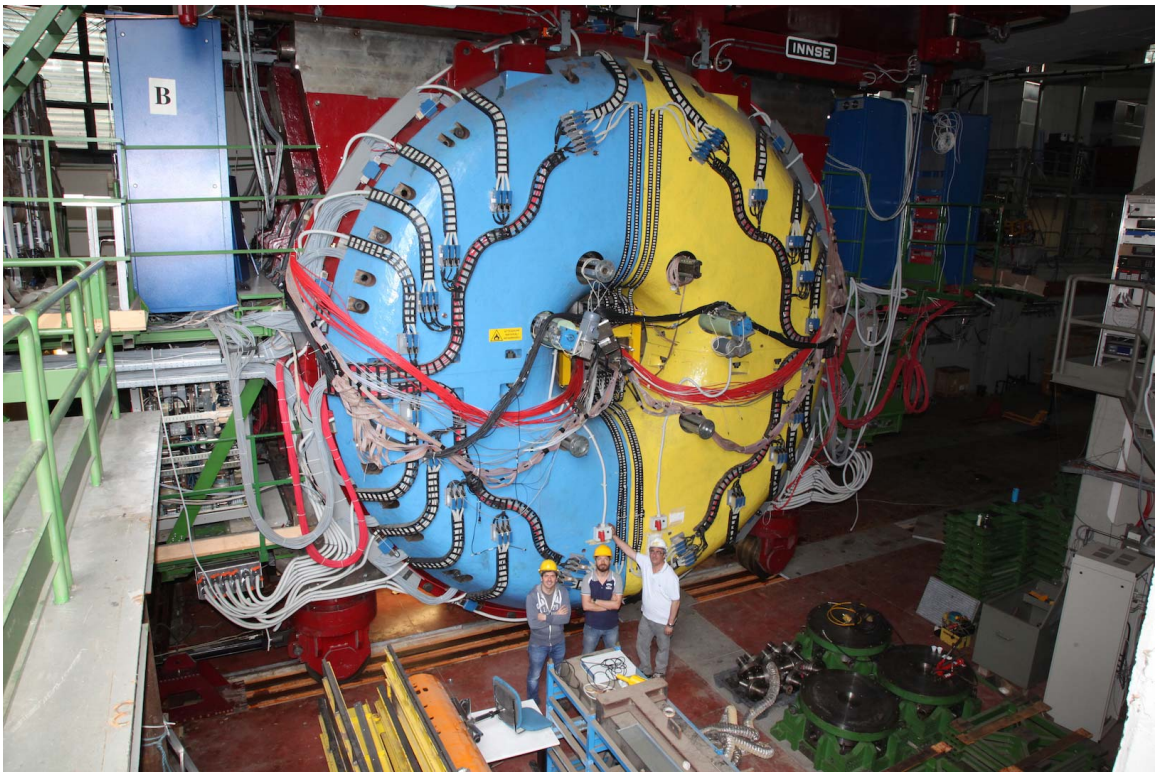

Figure 6.3: The KLOE experiment

The KLOE magnet is a superconducting magnet which successfully served for the KLOE experiment(K-LOng Experiment). It produces 0.6 T over a cylinder volume with 4.3 m length and 4.8 m diameter. The magnetic field is along the axial direction. The coil and cryostat weigh 8.5 tons, the return yoke weighs 475 tons.

The KLOE electromagnetic calorimeter[29] is a lead-scintillating fiber sampling calorimeter. Scintillating fibers offer high light transmission over several meters, sub-ns timing accuracy and very good hermetivity. It's composed of a barrel which is cylindrical and two endcaps ensure hermeticity. The barrel calorimeter consists of 24 modules, each one is 4.3 long, 23 thick with trapezoidal cross-section. Each module is made by 209 scintillating layer interleaved with 209 Lead layers. The scintillating fiber is along the axial direction and connect to photomultiplier tubes at two ends. For each module, there are 12×5 photomultiplier tubes connected. The two endcaps have similar structure. The total weight of calorimeter is about 100 tons, the

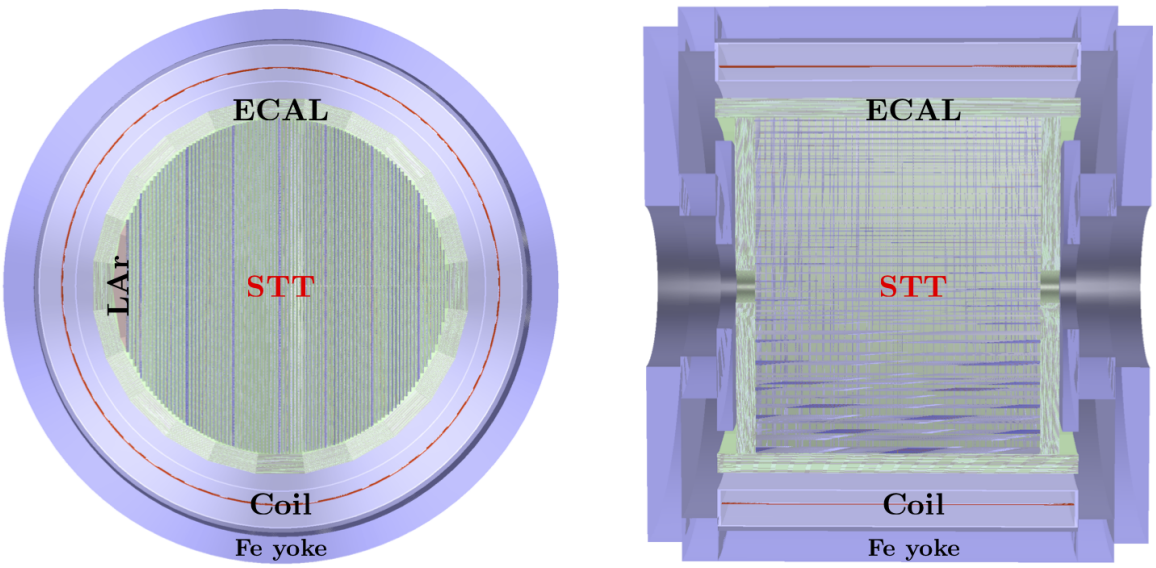

YZ view (beam -0.101 rad along Z) *XY view (B along X)*

Figure 6.4: Geometry of the complete detector with the inner magnetic volume filled by the STT supplemented by the LAr meniscus, as implemented in the GEANT4 simulations.

readout system includes 4880 photo-tubes. The energy resolution for the calorimeter is $\sigma/E = 5\%/\sqrt{E(GeV)}$, the timing resolution is $54/\sqrt{E(GeV)}$ ps.

6.3 Straw Tube Tracker

Typical neutrino detectors suffer from a conflict between two opposing requirements: large target mass to produce large quantity of neutrino interaction, low-dense enough to minimize multiple-scattering and provide high resolution tracking. Furthermore, in most fine-grained neutrino detectors, the active detector consisting of several different material and also provides target mass, a drawback of this configuration is the difficulty to precisely control the target chemical composition and size, limiting the ultimate precision achievable in the measurements. Additionally, it rarely provide an option to modify the target configuration during data taking. A straw tube technology based detector, is designed to offer a strategy to solve these outstanding

issues. It's named as Straw Tube Tracker (STT), it is configured in a way where the neutrino targets are physically separated from the actual tracking system (the straws) of negligible mass. The target mass materials are alternated with tracking straw tubes, therefore the mass is uniformly distributed throughout the tracker with an overall average low density. And the target modules can use different material at different location to serve different physics interests. It's also practical to replace target module during data taking.

STT is very flexible due to its modular design. By changing the modules' constituent and rearrange all the modules in a specific way, it can satisfy many demands such as total fiducial mass, specific target mass, average density. After a meticulous tuning of the module components and placement of different types modules, the following features can be achieved for STT: average density rho 0.18g/cm^3, radiation length X_0 2.8m, tracking sampling 0.15(0.36)%X_0 $\perp(\parallel)$.

A typical module, or standard module is designed with a total width of 44.09mm as following and shown in figure 6.5.

- The straws can be fabricated with either the ultrasonic welding or the traditional winding technologies. Each module consists of four straw layers XXYY glued together where the XX denotes two horizontal layers providing y coordinates measurement, YY denotes two vertical layers provide x coordinates measurements.

- The ultrasonic welding technology has been demonstrated in the COMET experiment that it's feasible to build straws with wall thickness of 12μm and 5mm diameter. A conservative design would be 20 μm. The wall will be coated with 70nm Al, the central wire is made of tungsten with 20μm diameter with a 20 nm gold coating.

- The four straw layers are preceded by a radiator composed of 150 polypropylene CH_2 foils 15 μm thick, interspaced by 120 μm air gaps. it's designed in this way to enhance transition radiation from which electron can be identified from pion. NOMAD have similar design and proved to have excellent e/π separation. The total thickness of the CH_2 in a single radiator is 2.25mm. The total thickness of one radiator is 20.13mm.

- The radiator is preceded by a solid polypropylene CH_2 target slab. The thickness of this slab, 5.3mm, can be tuned in order to achieve the desired target mass and detector density.

- Both the radiator and the CH_2 slab are removable without affecting the functionality and mechanical stability of the STT module.

- The default gas mixture for modules equipped with radiators is Xe/CO_2 70/30 operated with a internal pressure of about 1.9 atm.

- Each STT standard module contains a total of 7.55 mm thickness of CH_2 corresponding to 1.5% of the radiation length X_0.

6.3.1 Nuclear Targets and "solid" hydrogen concept

The STT is designed to offer a control of the configuration, chemical composition and mass of the neutrino targets similar to the one achieved in electron scattering experiments[5]. Various thin nuclear targets can be integrated into a STT module after removing the radiator and the polypropylene target slab.

The most important nuclear target material is graphite. CH_2 target slab and polypropylene provide interactions on CH_2, graphite slab provide interactions on C, by measuring them in same detector, a high precision of Hydrogen events can be extracted, these Hydrogen events are extremely valuable for flux measurement determination[8] and nuclear effect constraining. The graphite target can be implemented

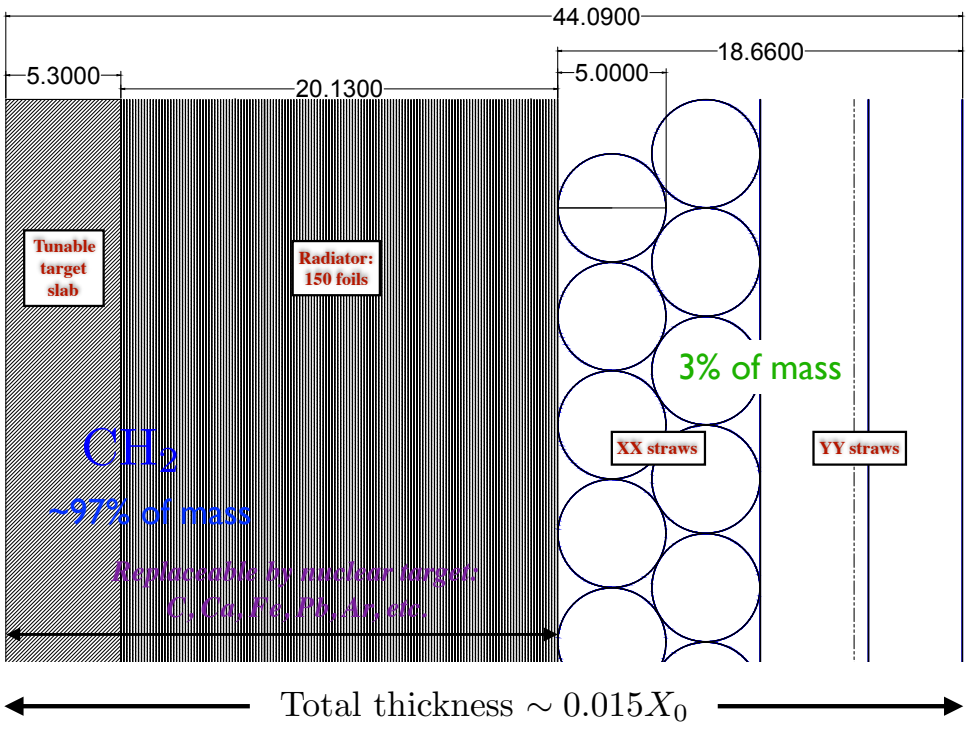

Figure 6.5: Drawing of a default compact STT module including three main elements (left to right): (a) a tunable polypropylene CH_2 target; (b) a radiator with 150 polypropylene foils for $e^{\pm}$ ID; (c) four straw layers XXYY. The radiator and plastic target are removed for modules to be equipped with nuclear targets.

by a "graphite module" in which the CH_2 slab and radiator are replaced by a graphite slab. The module structure is shown in Figure 6.6. The total length is 22.66mm and corresponds to about 2% of radiation length X_0. Ca is another important nuclear target, it has same atomic weight as Ar but is isoscalar, allowing a complete characterization of A= 40 nucleus, as well as various measurements related to isospin physics. A thin cryogenic liquid argon target is also planed to be added in front of the STT assembly. Above all, additional nuclear targets can be installed (Fe, Pb etc) depending upon nuclear measurements requested by the community. The default gas mixture used for STT modules equipped with nuclear targets (without radiator) is Ar/CO_2 70/30 with an 1.9 atm internal pressure.

The STT and related nuclear targets will fill the entire inner volume of KLOE magnet and ECAL, which is about 42.5m^3. As you can see, the targets' type and

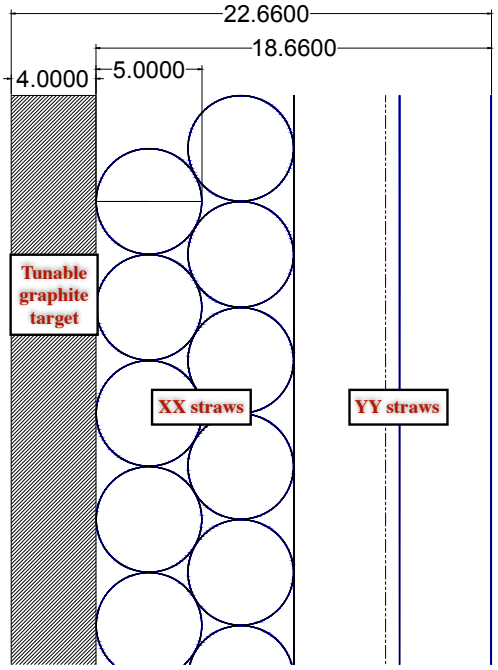

Figure 6.6: Drawing of one compact STT module equipped with graphite (pure C) target. The thickness of the C graphite plate is tuned to provide the same fraction of X_0 as the CH_2 modules.

width/mass can be tuned to achieve a desired fiducial mass and resolution and satisfy different physics goals at same time. The baseline STT configuration is described below and show in Figure 6.7.

- 91 modules installed horizontally along beam direction. They are introduced following the beamline
- LAr module: A liquid argon target located in the very front, followed with 8 straw layers XXYY + XXYY.
- 3 standard modules with CH_2 target slab and radiator.
- A sequence of 6 blocks, each composed of a "graphite module" followed by 12 standard module.
- One graphite module

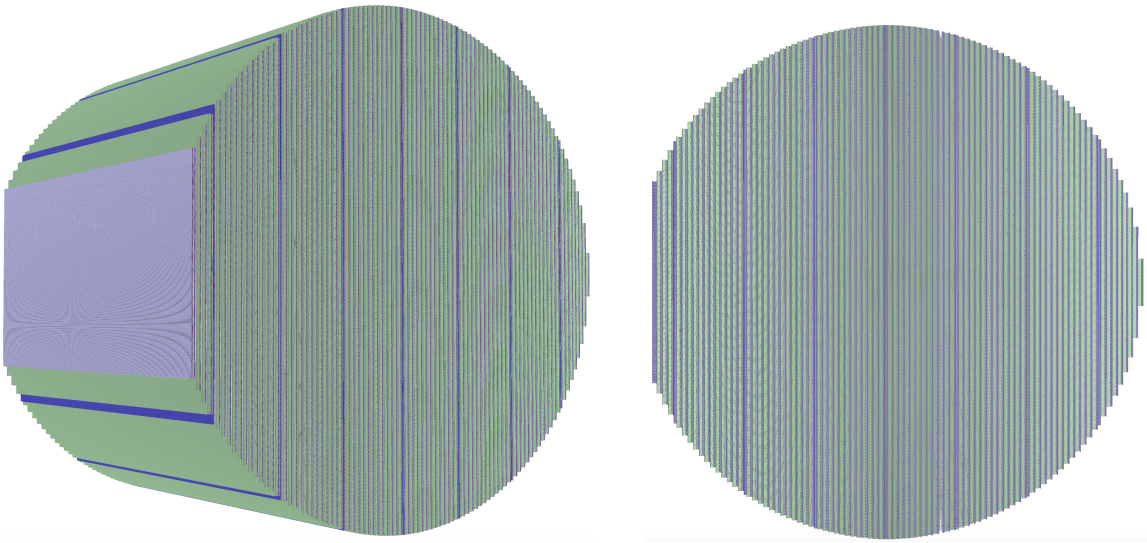

Figure 6.7: Views of the detailed STT geometry. The upstream empty space corresponds to the location of the internal LAr target, the first upstream STT module following the LAr target includes 8 straw layers XXYY+XXYY, the blue modules correspond to the ones equipped with graphite targets and are interleaved with standard CH_2 modules shown in green.

- 3 standard modules
- 5 tracking modules with CH_2 radiators but without target slab.
- The total thickness of the STT with the default configuration corresponds to about 1.42 X_0 including the straws and all target materials.

6.3.2 Performance and Advantages

Conservatively speaking, straw tubes have single hit resolution <200μm. But it's worth noting that the tracker of the COMET experiment implementing same technology as STT achieved a single hit resolution of about 140 μm. The STT provides superb momentum(3.5%), angular (2mrad), and timing (1ns) resolutions, as well as particle identification using both ionization signals dE/dx and the transition radiation. In NOMAD, transition radiation planes were able to have π rejections 10^3 for 90% electron efficiency.

The STT offers several unique advantages with respect to the other inner tracker candidates:

- By using polypropylene target radiators CH2 with 100% chemical purity and graphite target, a solid hydrogen target and its neutrino interactions can be well extracted and selected.
- Offering multiple nuclear targets candiates (e.g. C, Ca, Ar, etc.) to measure nuclear effects and compare with Hydrogen within the same detector with same acceptance.
- Timing resolution allowing to resolve the beam structure & withstanding high rates.
- Transition Radiation (TR) capability for electron/positron identification.
- 4π detection of π^0 from γ conversions within the STT volume.
- Flexible design allowing a variation of the target configuration with density $0.005 \leqslant \rho \leqslant 0.18$ g/cm^3.

6.3.3 Event simulation and reconstruction

Neutrino events are simulated by GENIE[15] and NUNDIS in FLUKA separately by different group. I specifically work on using GENIE to generate neutrino events. GENIE is very good at handling flux and geometry, it's able to accept flux as simple as a flat energy range , or as complicated as the output of upstream hadron production simulation done by another Monte Carlo program(dk2nu), or intermediately a three dimensional structure with both initial position and momentum of each neutrino ray (GSIMPLE, as the name says, it's still a simple format). As for the geometry, it can accept as simple as a list of target and their mass ratios, or more realistic like a gdml file. Geometry Description Markup Language (GDML) is a specialized XML-based

language designed as an application-independent persistent format for describing the geometries of detectors associated with physics measurements.It's not specific to a particular software, but supported by many HEP softwares such as GEANT and ROOT. GENIE is able to take GDML and realistic flux file like GSIMPLE/dk2nu as input, generate vertex by analyzing each neutrino ray traversing the detector geometry one by one. With official DUNE flux provided by fermilab beam group, and the STT based SAND detector geometry implemented in GDML, one is able to generate very realistic neutrino events with all the flavors of neutrino and all the target and their spatial relation considered.

Detector simulation is done by using GEANT4[24] and FLUKA separately. I focus on using GEANT4 based software EDep-sim. Edep-sim is basically a wrapper around GEANT4 with good input and output interface. Where it's available (in particular for argon), the simulation implements fairly detailed model of the energy deposited as ionization and scintillation. This is implemented using the NEST model. Edep-sim output is then converted into detector digits in order to be used for the subsequent event reconstruction.

Event reconstruction is also done separately in a detailed way (by a few Italian institutes) and fast way. I work on fast reconstruction particularly. Fast reconstruction is appreciable when detector is not built and there's no way to implement and validate a complete reconstruction which generally take years to do. But still, fast reconstruction can be realistic by using all the available detector/empirical/theoretical knowledge , and can be flexible enough to quickly serve downstream physics analyses. The fast reconstruction treat activity in electromagnetic calorimeter and STT differently. it also use different strategy for events originating in different detector area. Here I focus on events whose vertex is in fiducial volume of STT which is defined as 20cm inward from its boundary. For any charged particles such as $\mu^{+/-}$, $\pi^{+/-}$, their activities in STT are considered firstly, the number of straw tube hits can be

extracted from edep-sim, if it's number of y hit(track hitting horizontal straw tube will give y coordinate) is less than 4, it will be considered as un-reconstructable by STT, then calorimeter will be left to reconstruct it which may succeed or fail. If number of y hit is $\geqslant$4, Gluckstern formula is used to find out the track's measurement uncertainty of momentum and angle:

$$\begin{aligned}\left(\frac{\sigma_{P_\perp}}{P_\perp}\right)^2 &= \left(\frac{\sigma_{point} p_\perp}{0.3BL^2}\sqrt{\frac{720}{N+4}}\right)^2 + \left(\frac{0.05}{BL}\sqrt{\frac{1.43L}{X_0}}\right)^2 \\ \sigma_\theta^2 &= \left(\frac{\sigma_L}{L}\sqrt{\frac{12(N-1)}{N(N+1)}}\right)^2 + \left(\frac{0.015}{\sqrt{3}p}\sqrt{\frac{L}{X_0}}\right)^2\end{aligned} \tag{6.1}$$

with the track length, number of y hits as input. Later on a circular fit is developed too.

6.4 Coherent pion potential on flux ratio determination

As I mentioned in previous chapters, Coherent pion has a clean experimental signature. It has very little momentum transfer to the nucleus which remains in its ground state, small missing P_t and only a muon and a pion coming out without any other activities in the detector. Nuclear effects are much smaller than neutrino-nucleon interactions.

6.4.1 wrong sign contamination measurement

In any accelerator based oscillation experiment, the neutrino beam is always contaminated with wrong-sign neutrinos, i.e neutrino-mode contaminated by antineutrinos, anti-neutrino mode contaminated by neutrinos. It becomes critical to measure the ratio of $\nu/\bar{\nu}$ to achieve a high precision oscillation measurement. The ratio of CC coherent $\pi-/\pi+$ provides an excellent way to precisely measure the $\nu_\mu/\bar{\nu_\mu}$ flux ratio as a function of energy. Both interactions have the same experimental signatures with opposite charge ($\mu^-\pi+$ and $\mu^+\pi-$, respectively), the systematic uncertainties

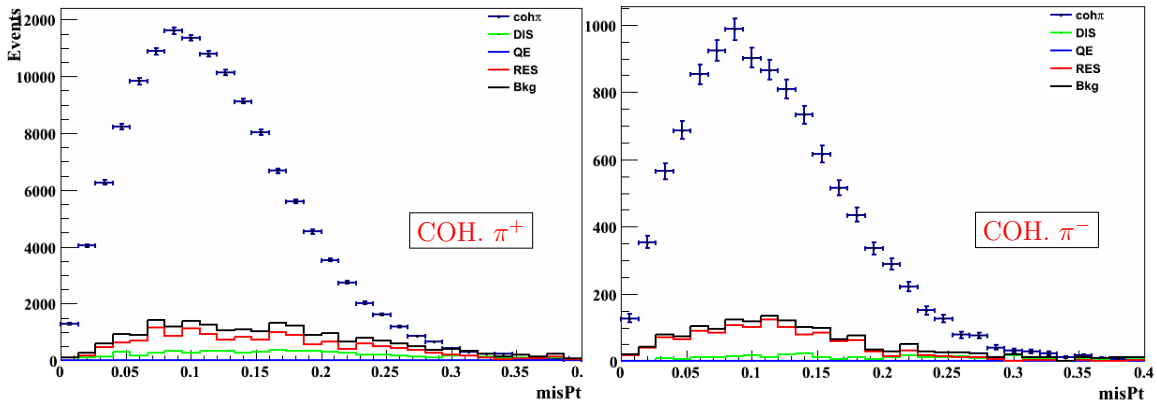

Figure 6.8: Reconstructed missing transverse momentum for coherent π^+ (left panel) and π^-(right panel) selected in STT in neutrino beam mode. The histograms show the actual statistics expected.

related to the event selection largely cancel out by the ratio. Model uncertainties also significantly cancel out. In particular, Adler's theorem which is based on the partially conserved axial current (PCAC) theorem, relating the neutrino-nucleus cross section to the pion-nucleus elastic cross section, predict that the neutrino and antineutrino cross-sections are the same for an isoscalar target. Small corrections from interference effects with the vector current are expected in some microscopic models. Coherent $\pi_{\pm}$ interactions in the STT radiators occur on isoscalar carbon nucleus, thus offering a potential reduction of systematics.

The most important experimental parameter is the resolution of |t|(the momentum transfer to the nucleus), requiring high momentum and angular resolutions. The fiducial mass of STT provides enough statistics for a precise measurement of the wrong sign component of the beam through coherent πproduction. the STT selection result of coherent $\pi_{\pm}$ in the FHC beam mode is shown in Figure 6.8. Overall, we can achieve an efficiency of 43% (42%) with a purity of 87% (86%) for coherent $\pi+(\pi-)$ in STT. In Figure 6.9 we summarize the corresponding precision on the $\nu_\mu/\bar{\nu_\mu}$ flux ratio achievable in STT for both the FHC and RHC beam modes, the uncertainty predicted by PPFX[11] is in comparison. PPFX is package developed in Fermilab to predict the flux with hadron production corrections using all relevant data. It

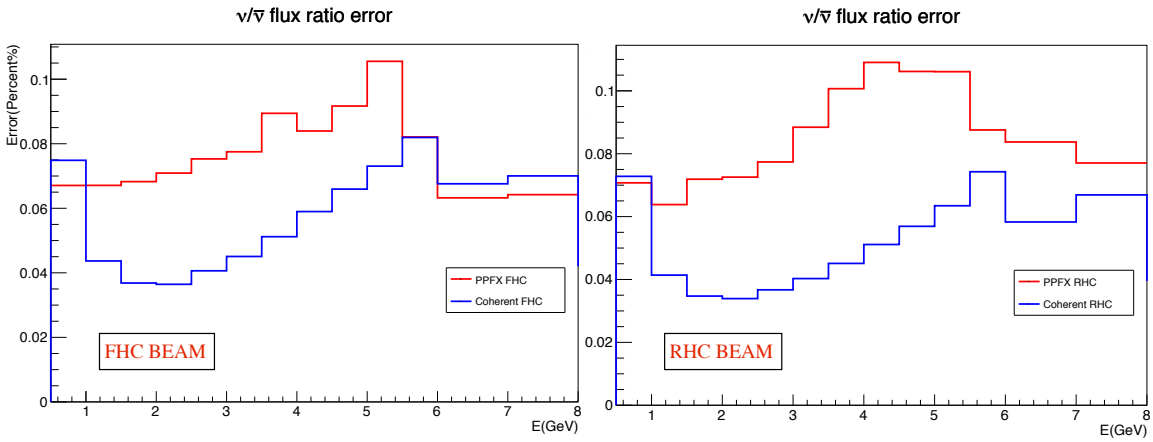

Figure 6.9: Uncertainty on the $\nu_\mu/\bar{\nu}_\mu$ flux ratio determined in STT from the ratio of coherent pion production in FHC neutrino mode (left panel) and RHC antineutrino mode(right panel). The uncertainties obtained by PPFX from the beam group are in comparison

can be seen the STT measurements with coherent pion channel offer a powerful in-situ constraint on such flux ratios, with uncertainties greatly reduced comparing to PPFX's.

Bibliography

[1] P. Bernardini et al. "Enhancing the LBNF/DUNE Physics Program". In: *European Particle Physics Strategy Update 2018-2020*. URL: https://indico.cern.ch/event/765096/contributions/3295805/.

[2] M A Acero et al. "Measurement of neutrino-induced neutral-current coherent $\pi 0$ production in the NOvA near detector". In: *Physical Review D* 102.1 (July 2020). ISSN: 2470-0029. DOI: 10.1103/physrevd.102.012004. URL: http://dx.doi.org/10.1103/PhysRevD.102.012004.

[3] G.Adamovetal. *A Proposal to enhance the DUNE Near-Detector Complex*. Tech. rep. 2020, DUNEDocDb#13262.

[4] H. Duyang, B. Guo, S. R. Mishra, and R. Petti. "A precise determination of (anti)neutrino fluxes with (anti)neutrino-hydrogen interactions". In: *Physics Letters, Section B: Nuclear, Elementary Particle and High-Energy Physics* (2019). ISSN: 03702693. DOI: 10.1016/j.physletb.2019.06.003. arXiv: 1902.09480.

[5] Petti Roberto. "Precision Measurements of Fundamental Interactions with (Anti-)Neutrinos". In: *27th International Workshop on Deep Inelastic Scattering and Related Subjects (DIS 2019)*. 2019.

[6] D. Adey et al. "Measurement of the Electron Antineutrino Oscillation with 1958 Days of Operation at Daya Bay". In: *Physical Review Letters* (2018). ISSN: 10797114. DOI: 10.1103/PhysRevLett.121.241805. arXiv: 1809.02261.

[7] L. Alvarez-Ruso et al. *NuSTEC White Paper: Status and challenges of neutrino–nucleus scattering*. 2018. DOI: 10.1016/j.ppnp.2018.01.006. arXiv: 1706.03621.

[8] H Duyang, B Guo, S R Mishra, and R Petti. "A Novel Approach to Neutrino-Hydrogen Measurements". In: (2018). arXiv: 1809.08752 [hep-ph].

[9] A. Mislivec et al. "Measurement of total and differential cross sections of neutrino and antineutrino coherent $\pi^{\pm}$ production on carbon". In: *Phys. Rev. D* 97.3 (2018), p. 032014. DOI: 10.1103/PhysRevD.97.032014. arXiv: 1711.01178 [hep-ex].

[10] M. Tanabashi et al. *Review of Particle Physics*. 2018. DOI: 10.1103/PhysRevD.98.030001.

[11] Leonidas Aliaga Soplin. "Neutrino Flux Prediction for the NuMI Beamline". PhD thesis. William-Mary Coll., 2016. DOI: 10.2172/1250884.

[12] L. Aliaga et al. "Neutrino flux predictions for the NuMI beam". In: *Physical Review D* (2016). ISSN: 24700029. DOI: 10.1103/PhysRevD.94.092005. arXiv: 1607.00704.

[13] Jun Cao and Kam Biu Luk. "An overview of the Daya Bay reactor neutrino experiment". In: *Nuclear Physics B* (2016). ISSN: 05503213. DOI: 10.1016/j.nuclphysb.2016.04.034. arXiv: 1605.01502.

[14] T. Kajita, E. Kearns, and M. Shiozawa. "Establishing atmospheric neutrino oscillations with Super-Kamiokande". In: *Nuclear Physics B* (2016). ISSN: 05503213. DOI: 10.1016/j.nuclphysb.2016.04.017.

[15] Costas Andreopoulos et al. "The GENIE Neutrino Monte Carlo Generator: Physics and User Manual". In: (2015). arXiv: 1510.05494 [hep-ph].

[16] Hongyue Duyang, Xinchun Tian, and Sanjib R Mishra. "Measurement of Resonance Interaction in The NOMAD Detector". In: *PoS* NUFACT2014 (2015), p. 60. DOI: 10.22323/1.226.0060.

[17] Jiang Libo. "Neutrino and Antineutrino Induced Meson Production". Doctoral disseration. University of South Carolina, 2015. URL: https://scholarcommons.sc.edu/etd/3590.

[18] "Long-Baseline Neutrino Facility (LBNF) and Deep Underground Neutrino Experiment (DUNE) Conceptual Design Report, Volume 2: The Physics Program for DUNE at LBNF". In: (Nov. 2015). DOI: 10.2172/1264020. URL: http://dx.doi.org/10.2172/1264020.

[19] G. Bellini, L. Ludhova, G. Ranucci, and F. L. Villante. "Neutrino oscillations". In: *Advances in High Energy Physics* 2014.October 2013 (2014). ISSN: 16877357. DOI: 10.1155/2014/191960. arXiv: 1310.7858.

[20] LBNE Collaboration et al. *The Long-Baseline Neutrino Experiment: Exploring Fundamental Symmetries of the Universe*. 2013. arXiv: 1307.7335 [hep-ex].

[21] Joseph A Formaggio. "From eV to EeV : Neutrino Cross-Sections Across Energy Scales". In: *Reviews of Modern Physics* (2013). arXiv: 1305.7513v1.

[22] X. C. Tian. "Neutrino induced charged-current coherent ρ production". In: *15th International Workshop on Neutrino Factories, Super Beams and Beta Beams, NuFact 2013*. 2013.

[23] C. T. Kullenberg et al. "A search for single photon events in neutrino interactions". In: *Physics Letters, Section B: Nuclear, Elementary Particle and High-Energy Physics* (2012). ISSN: 03702693. DOI: 10.1016/j.physletb.2011.11.049.

[24] S. Guatelli, D. Cutajar, B. Oborn, and A. B. Rosenfeld. "Introduction to the geant4 simulation toolkit". In: *AIP Conference Proceedings*. 2011. ISBN: 9780735409019. DOI: 10.1063/1.3576174.

[25] Christoph Berger. "PCAC and coherent pion production by neutrinos". In: *AIP Conference Proceedings*. 2009. ISBN: 9780735407251. DOI: 10.1063/1.3274159. arXiv: 0908.2758.

[26] C. T. Kullenberg et al. "A measurement of coherent neutral pion production in neutrino neutral current interactions in the NOMAD experiment". In: *Physics Letters, Section B: Nuclear, Elementary Particle and High-Energy Physics* (2009). ISSN: 03702693. DOI: 10.1016/j.physletb.2009.10.083.

[27] Q. Wu et al. "A precise measurement of the muon neutrino–nucleon inclusive charged current cross section off an isoscalar target in the energy range 2.5-40 GeV by NOMAD". In: *Physics Letters B* (2008). ISSN: 03702693. DOI: 10.1016/j.physletb.2007.12.027.

[28] T. Araki et al. "Measurement of neutrino oscillation with KamLAND: Evidence of spectral distortion". In: *Physical Review Letters* (2005). ISSN: 00319007. DOI: 10.1103/PhysRevLett.94.081801. arXiv: 0406035 [hep-ex].

[29] M. Adinolfi et al. "The KLOE electromagnetic calorimeter". In: *Nuclear Instruments and Methods in Physics Research, Section A: Accelerators, Spectrometers, Detectors and Associated Equipment* (2002). ISSN: 01689002. DOI: 10.1016/s0168-9002(01)01502-9.

[30] P Astier et al. "Final NOMAD results on muon-neutrino —> tau-neutrino and electron-neutrino —> tau-neutrino oscillations including a new search for tau-neutrino appearance using hadronic tau decays". In: *Nucl. Phys. B* 611 (2001), pp. 3–39. DOI: 10.1016/S0550-3213(01)00339-X. arXiv: 0106102 [hep-ex].

[31] J Altegoer et al. "The NOMAD experiment at the CERN SPS". In: *Nucl. Instrum. Meth. A* 404 (1998), pp. 96–128. DOI: 10.1016/S0168-9002(97)01079-6.

[32] Bruce T. Cleveland et al. “Measurement of the Solar Electron Neutrino Flux with the Homestake Chlorine Detector”. In: *The Astrophysical Journal* 496.1 (Mar. 1998), pp. 505–526. ISSN: 0004-637X. DOI: 10.1086/305343. URL: https://iopscience.iop.org/article/10.1086/305343.

[33] Raymond Davis. “A review of the homestake solar neutrino experiment”. In: *Progress in Particle and Nuclear Physics* (1994). ISSN: 01466410. DOI: 10.1016/0146-6410(94)90004-3.

[34] P. Vilain et al. “Coherent single charged pion production by neutrinos”. In: *Physics Letters B* (1993). ISSN: 03702693. DOI: 10.1016/0370-2693(93)91223-A.

[35] S. Willocq et al. “Coherent production of single pions and ρ mesons in charged-current interactions of neutrinos and antineutrinos on neon nuclei at the Fermilab Tevatron”. In: *Phys. Rev. D* 47 (7 Apr. 1993), pp. 2661–2674. DOI: 10.1103/PhysRevD.47.2661. URL: https://link.aps.org/doi/10.1103/PhysRevD.47.2661.

[36] M. Aderholz et al. “Coherent production of π^+ and π^- mesons by charged-current interactions of neutrinos and antineutrinos on neon nuclei at the Fermilab Tevatron”. In: *Phys. Rev. Lett.* 63 (21 Nov. 1989), pp. 2349–2352. DOI: 10.1103/PhysRevLett.63.2349. URL: https://link.aps.org/doi/10.1103/PhysRevLett.63.2349.

[37] Pierre Marage et al. “Coherent production of $\pi+$ mesons in ν neon interactions”. In: *Zeitschrift für Physik C Particles and Fields* 43 (1988), pp. 523–526.

[38] David Griffiths. *Introduction to Elementary Particles*. 1987. DOI: 10.1002/9783527618460.

[39] Dieter Rein and Lalit M. Sehgal. “Coherent $\pi 0$ production in neutrino reactions”. In: *Nuclear Physics, Section B* (1983). ISSN: 05503213. DOI: 10.1016/0550-3213(83)90090-1.

[40] Stephen L. Adler. “Tests of the conserved vector current and partially conserved axial-vector current hypotheses in high-energy neutrino reactions”. In: *Physical Review* (1964). ISSN: 0031899X. DOI: 10.1103/PhysRev.135.B963.